Theoretical Investigation of stimulated Brillouin scattering in Optical Fibers and their Applications

by

Daisy Williams

Thesis submitted to the
Faculty of Graduate and Postdoctoral Studies
in partial fulfillment of the requirements
for the Doctorate in Philosophy degree in Physics

Department of Physics
Faculty of Science
University of Ottawa

To my parents

Abstract

In 1920, Leon Brillouin discovered a new kind of light scattering – Brillouin scattering – which occurs as a result of the interaction of light with a transparent material's temporal periodic variations in density and refractive index. Many advances have since been made in the study of Brillouin scattering, in particular in the field of fiber optics. An in-depth investigation of Brillouin scattering in optical fibers has been carried out in this thesis, and the theory of stimulated Brillouin scattering (SBS) and combined Brillouin gain and loss has been extended. Additionally, several important applications of SBS have been found and applied to current technologies.

Several mathematical models of the pump-probe interaction undergoing SBS in the steady-state regime have emerged in recent years. Attempts have been made to find analytical solutions of this system of equations, however, previously obtained solutions are numerical with analytical portions and, therefore, qualify as hybrid solutions. Though the analytical portions provide useful information about intensity distributions along the fiber, they fall short of describing the spectral characteristics of the Brillouin amplification and the lack of analytical expressions for Brillouin spectra substantially limits the utility of the hybrid solutions for applications in spectral measurement techniques. In this thesis, a highly accurate, fully analytic solution for the pump wave and the Stokes wave in Brillouin amplification in optical fibers is given. It is experimentally confirmed that the reported analytic solution can account for spectral distortion and pump depletion in the parameter space that is relevant to Brillouin fiber sensor applications. The analytic solution provides a valid characterization of Brillouin amplification in both the low and high nonlinearity regime, for short fiber lengths. Additionally, a *3D parametric model* of Brillouin amplification is proposed, which reflects the effects of input pump and Stokes powers on the level of pump wave depletion in the fiber, and acts as a classification tool to describe the level of similarity between various Brillouin amplification processes in optical fibers.

At present, there exists a multitude of electro-optic modulators (EOM), which are used to modulate the amplitude, frequency, phase and polarization of a beam of light. Among these modulators, phase modulation provides the highest quality of transmitted signal. As such, an improved method of phase-modulation, based on the principles of stimulated Brillouin scattering, as well as an optical phase-modulator and optical phase network employing the same, has been developed.

Due to its robustness, low threshold power, narrow spectrum and simplicity of operation, stimulated Brillouin scattering (SBS) has become a favourable underlying mechanism in fiber-based devices used for both sensing and telecommunication applications. Since birefringence is a detrimental effect for both, it is important to devise a comprehensive characterization of the SBS process in the presence of birefringence in an optical fiber. In this thesis, the most general model of elliptical birefringence in an optical fiber has been developed for a steady-state and transient stimulated Brillouin scattering (SBS) interaction, as well as the combined Brillouin gain and loss regime. The impact of the elliptical birefringence is to induce a Brillouin frequency shift and distort the Brillouin spectrum – which varies with different light polarizations and pulse widths. The model investigates the effects of birefringence and the corresponding evolution of spectral distortion effects along the fiber, and proposes regimes that are more favourable for sensing applications related to SBS – providing a valuable prediction tool for distributed sensing applications.

In recent years, photonic computing has received considerable attention due to its numerous applications, such as high-speed optical signal processing, which would yield much faster computing times and higher bandwidths. For this reason, optical logic has been the focus of many research efforts and several schemes to improve conventional logic gates have been proposed. In view of this, a combined Brillouin gain and loss process has been proposed in a polarization maintaining optical fiber to realize all-Optical NAND/NOT/AND/OR logic gates in the frequency domain. A model describing the interaction of a Stokes, anti-Stokes and a pump wave, and two acoustic waves inside a fiber, ranging in length from 350m-2300m, was used to theoretically model the gates. Through the optimization of the pump depletion and gain saturation in the combined gain and loss process, switching contrasts of 20-83% have been simulated for different configurations.

Statement of Originality

This work contains no material which has been accepted for the award of any other degree or diploma in an University or other tertiary institution and, to the best of my knowledge and belief, contains no material previously published or written by another person, except where due reference has been made in the text.

I give consent to this copy of my thesis, when deposited in the University Library, being available for loan and photocopying.

SIGNED: ____________________________

DATED: _____________________________

Supervisors: Dr. Xiaoyi Bao and Dr. Liang Chen

Acknowledgments

It is my pleasure to take this opportunity to thank all the people who have helped me over the past few years.

First of all, I would like to thank my supervisors Dr. Xiaoyi Bao and Dr. Liang Chen, who invited me to join their group as a graduate student and gave me the chance to do research on stimulated Brillouin scattering (SBS) in optical fibers. I am grateful for the opportunity to have worked in their Fiber Optics Group at the University of Ottawa, in an environment which supported and motivated me to achieve my goals. I would like to thank Dr. Xiaoyi Bao and Dr. Liang Chen for the interest they showed in my progress and for the guidance they gave me. Their diligence and persistence in both research and mentorship is deeply appreciated. Their critical and thoughtful approach to problems was always instructive.

I must give many thanks to my colleagues in Fiber Optics Group at University of Ottawa. Their comments and suggestions have greatly benefited me. Special thanks to Bhavaye Saxena for interesting discussions and Dr. Dapeng Zhou for helping with my experimental setup. Their kind help and valuable suggestions went a long way in furthering my research goals.

I am deeply indebted to my parents. Their enduring love and support gave me the strength to overcome the challenges of being a Ph.D. student. To them, I dedicate this thesis.

– Daisy Williams

Table of Contents

Abstract........ iii
Acknowledgments........ vi
List of Figures........ x
List of Tables........ xiv
List of Acronyms........ xv

Chapter 1. Introduction........ 1
- 1.1 Overview........ 1
- 1.2 *3D parametric model*........ 2
- 1.3 SBS optical phase modulator........ 3
- 1.4 Polarization effects in SBS........ 4
- 1.5 Photonic Logic........ 6
- 1.6 Thesis contributions........ 8
- 1.7 Thesis outline........ 10

Chapter 2. Physics of Brillouin Scattering........ 12
- 2.1 Introduction........ 12
- 2.2 Light Scattering 12
- 2.3 Spontaneous Brillouin Scattering........ 14
- 2.4 Stimulated Brillouin Scattering........ 18
  - 2.4.1 SBS Generator........ 18
  - 2.4.2 SBS Amplifier........ 19
  - 2.4.3 Electrostriction........ 19
  - 2.4.4 SBS Coupled wave equations and configuration........ 20
  - 2.4.5 Combined Brillouin gain and loss coupled wave equations and configuration........ 23
- 2.5 Polarization and birefringence........ 25
  - 2.5.1 Polarization states........ 25
  - 2.5.2 Polarization Ellipse........ 26
  - 2.5.3 Poincaré Sphere........ 28
  - 2.5.4 Birefringence........ 30
- 2.6 Summary........ 31

Chapter 3. *3D parametric model*........ 32
- 3.1. Introduction........ 32
- 3.2 Model........ 33
- 3.3 Solution........ 36
- 3.4 Analytic Solutions........ 39
  - 3.4.1 Linear approximation........ 40
  - 3.4.2 Quadratic approximation........ 41
- 3.5 Relative error........ 41
  - 3.5.1 Linear Approximation........ 42
  - 3.5.2 Quadratic Approximation........ 43

3.6 *3D parametric model*.. 44
3.7 *3D parametric model*: Similar and Dis-similar Processes................. 45
3.8 Applications in Fiber Sensing.. 48
3.9 Spectral Characteristics.. 49
  3.9.1 Analytical expressions.. 49
  3.9.2 Transition to a Lorentzian Spectra (Curvature).................. 52
3.10 Experiment.. 55
  3.10.1 Experimental Setup.. 55
  3.10.2 Experimental Results... 56
3.11 Summary.. 57

Chapter 4. SBS Optical Phase Modulator and Network.. 58
4.1 Introduction.. 58
4.2 Theory... 58
4.3 Proposed Experimental Setup... 63
4.4 Optical phase modulator construction.. 67
4.4 Optical network transmission lines with phase-modulated carriers 68
4.5 Summary.. 72

Chapter 5. Polarization Effects in SBS.. 73
5.1 Introduction.. 73
5.2 Model.. 74
5.3. Results and Discussion... 79
  5.3.1 Spectral Shift... 79
  5.3.2 Spectral Distortion.. 82
    A. Linear Polarization (LP).. 82
    B. Elliptical Polarization for steady-state interaction.... 86
5.4 Summary.. 90

Chapter 6. Polarization Effects in combined Brillouin gain and loss..................... 91
6.1 Introduction.. 91
6.2 Model.. 91
6.3 Results and Discussion... 98
  6.3.1. Gain dominant regime... 98
  6.3.2 Competing Gain and Loss regime.. 102
6.4 Summary.. 105

Chapter 7. Applications of SBS: Photonic Logic.. 106
7.1 Introduction.. 106
7.2 Model.. 106
7.3 Results and Discussion... 110
7.4 NAND gate... 110
  7.4.1 Configuration I... 110
  7.4.2 Configuration II... 111
  7.4.3 Configuration III... 112
7.5 NOT gate.. 114
  7.5.1 Configuration IV... 114

7.5.2 Configuration V.. 115
7.6 AND gate.. 115
7.6.1 Configuration VI... 115
7.6.2 Configuration VII.. 117
7.6.3 Configuration VIII... 118
7.7 OR gate... 119
7.7.1 Configuration IX... 119
7.7.2 Configuration X... 120
7.7.3 Configuration XI... 122
7.8 General method of logic gate construction.. 123
7.8.1 Configuration V: NOT gate.. 123
7.8.2 Configuration IV: NOT gate... 125
7.8.3 Configurations I and II: NAND gates... 126
7.8.4 Configuration III: NAND gate.. 127
7.8.5 3D parametric model applications in photonic logic........... 129
7.9 Proposed Experimental Configurations... 130
7.9.1 Configurations I-V... 130
7.9.2 Configurations VI.. 132
7.9.3 Configurations VII.. 134
7.9.4 Configurations IX.. 135
7.9.5 Configurations X... 137
7.9.6 Configurations XI.. 138
7.10 Bit rate.. 140
7.11 Summary... 140

Chapter 8. Conclusion.. 141
8.1 Thesis Outcomes... 141
8.2 Future Work... 142

Bibliography... 144
Appendix.. 153
A. Derivation of the system of equations (5.1)-(5.4)................................ 153
B. Fourth Order Runge-Kutta Method of Solution................................ 157
Curriculum Vitae.. 159

List of Figures

Figure 2.1:	Schematic of the observed scattered light intensity [1].	**13**
Figure 2.2:	Stokes Brillouin scattering [1]. (a) Relative orientations of the wavevectors $\boldsymbol{k}_1$ and $\boldsymbol{k}_2$, (b) $\boldsymbol{k}_1$, $\boldsymbol{k}_2$ and $\boldsymbol{q}$ relationship, Schematic of SBS interaction.	**16**
Figure 2.3:	Anti-Stokes Brillouin scattering [1]. (a) Relative orientations of the wavevectors $\boldsymbol{k}_1$ and $\boldsymbol{k}_3$, (b) $\boldsymbol{k}_1$, $\boldsymbol{k}_3$ and $\boldsymbol{q}$ relationship, Schematic of SBS interaction.	**17**
Figure 2.4:	SBS generator [1].	**19**
Figure 2.5:	SBS amplifier [1].	**19**
Figure 2.6:	Schematic arrangement of SBS in a fiber of length L. Pump and probe configuration: $A_1(z)$ – Pump wave, $A_2(z)$ – probe wave (incident pulse).	**21**
Figure 2.7:	Schematic distribution of the pump and probe intensities during SBS [1].	**23**
Figure 2.8:	Schematic arrangement of SBS in a PMF of length L. PW and pulse configuration: A_1 – pump wave, A_2 – Stokes wave, A_3 – anti-Stokes wave.	**24**
Figure 2.9:	Different polarization states, figure taken from *Wikipedia*.	**25**
Figure 2.10:	Polarization Ellipse.	**27**
Figure 2.11:	Poincaré Sphere.	**28**
Figure 3.1:	Relative error of $\mathrm{Y}_1(0)$: Linear Approximation of *3D parametric model* of output PW. L=1000m, $0<P_{pump}<10$mW , $0<P_{Stokes}<40$mW.	**42**
Figure 3.2:	Relative error of $Y_1(0)$: Quadratic Approximation of *3D parametric model* of output PW. L=1000m, $0<P_{pump}<10$mW , $0<P_{Stokes}<40$mW.	**43**
Figure 3.3:	Linear Approximation of $Y_1(0)$: *3D parametric model* of output PW. Dimensionless output intensity of the PW versus dimensionless parameters β_1 and β_3. γ_e=0.902, v=5616 m/s, n=1.48, λ=1.319µm, ρ_0=2.21 g/cm^3, Γ_B = 0.1 GHz, L=1000m, $0<P_{pump}<10$mW , $0<P_{Stokes}<40$mW.	**44**
Figure 3.4:	Linear Approximation of $Y_2(\ell)$: *3D parametric model* of output SW. Dimensionless output intensity of the SW versus dimensionless parameters β_1 and β_3. γ_e=0.902, v=5616 m/s, n=1.48, λ=1.319µm, ρ_0=2.21 g/cm^3, Γ_B = 0.1 GHz, L=1000m, $0<P_{pump}<10$mW, $0<P_{Stokes}<40$mW.	**45**
Figure 3.5:	Linear Approximation of $Y_1(0)$: *3D parametric model* of output PW. Dimensionless output intensity of the PW versus dimensionless parameters β_1 and β_3. γ_e=0.902, v=5616 m/s, n=1.48, λ=1.319µm, ρ_0=2.21 g/cm^3, Γ_B = 0.1 GHz, L=1000m, $0<P_{pump}<10$mW , $0<P_{Stokes}<40$mW.	**47**
Figure 3.6:	Analytical results, normalized intensity units of the SW. P_{SW} (mW) = ○ 0.01; △ 1.8; x 6.6; □ 12.1; ▽ 17.1; + 22.4; ✱ 27.2; --- 31.8; ▬ 36.3; n=1.48, γ_e=0.902, λ=1319nm, ρ_0=2.21 g/cm^3, v=5616 m/s, L=1000 m, Γ_B=0.1 GHz, P_{PW} = 1.0 mW.	**50**

Figure 3.7:	Pump depletion as a function of probe spectral distortion. P_{SW} (mW) = ○ 0.01; △ 1.8; × 6.6; □ 12.1; ▽ 17.1; + 22.4; ✱ 27.2; ■ 31.8; ♦ 36.3; n=1.48, γ_e=0.902, λ=1319nm, ρ_0=2.21 g/cm^3, v=5616 m/s, L=1000 m, Γ_B=0.1 GHz, P_{PW} = 1.0 mW.	**51**
Figure 3.8:	Shaded area depicts range of β_1 and β_3 values which yield curvatures within 20% of the Lorentz Curvature for both PW and SW spectra.	**54**
Figure 3.9:	Experimental setup.	**55**
Figure 3.10:	Experimental results, normalized intensity units of the SW. P_{SW} (mW) = ○ 0.01; △ 1.8; × 6.6; □ 12.1; ▽ 17.1; + 22.4; ✱ 27.2; --- 31.8; ▬ 36.3; n=1.48, γ_e=0.902, λ=1319nm, ρ_0=2.21 g/cm^3, v=5616 m/s, L=1000m, Γ_B=0.1 GHz, P_{PW} = 1.0 mW.	**56**
Figure 4.1:	Form factor as a function of ξ_1.	**61**
Figure 4.2:	Gain factor as a function of ξ_1.	**62**
Figure 4.3:	Experimental setup.	**63**
Figure 4.4:	Optical phase modulator construction.	**67**
Figure 4.5:	Optical network construction.	**69**
Figure 5.1:	Schematic arrangement of SBS in an optical fiber of length L. E_{1x} – Pump wave, E_{1y} – Pump wave, E_{2x} – Stokes wave, E_{2y} – Stokes wave.	**74**
Figure 5.2:	(a) Output pump spectrum, (b) output Stokes spectrum. Birefringence Δn: *10^{-4}; — 10^{-5}; --- 10^{-6}; LHP(1,0,0); L=1000m. P_{1x0} = 0.5 mW, P_{1y0} = 0.5 mW, P_{2x0} = 0.5 mW, P_{2y0} = 0.5 mW.	**80**
Figure 5.3:	Brillouin shift dependence on beat length, L=1000m, LHP (1,0,0). (a) P_{1x0} = 0.9 mW, P_{1y0} = 0.1 mW, P_{2x0} = 0.9 mW, P_{2y0} = 0.1 mW. (b) P_{1x0} = 0.5 mW, P_{1y0} = 0.5 mW, P_{2x0} = 0.5 mW, P_{2y0} = 0.5 mW.	**81**
Figure 5.4:	Left: output pump spectrum; Right: output Stokes spectrum. (a)-(b) steady-state; (c)-(d) 240ns pulse; (e)-(f) 79ns pulse; Birefringence Δn=10^{-4}; L=1 km. -··-: P_{1x0} = 10.0 mW, P_{1y0} = 1.0 mW, P_{2x0} = 10.0 mW, P_{2y0} = 1.0 mW; LHP (1,0,0); —: P_{1x0} = 10.9 mW, P_{1y0} = 0.1 mW, P_{2x0} = 10.9 mW, P_{2y0} = 0.1 mW; LHP (1,0,0); ---: P_{1x0} = 10.0 mW, P_{1y0} = 1.0 mW, P_{2x0} = 10.0 mW, P_{2y0} = 1.0 mW; no pol (0,0,0).	**82 -83**
Figure 5.5:	(a) x-comp. of output Stokes spectrum; (b) y-comp. of output Stokes spectrum. Birefringence Δn = * 10^{-4} ; — 10^{-5}; --- 10^{-6}; Random4 (0.1,0.9,0.42), L=1000m. P_{1x0} = 10.0 mW, P_{1y0} = 1.0 mW, P_{2x0} = 10.0 mW, P_{2y0} = 1.0 mW.	**87**
Figure 5.6:	(a) Output pump spectrum, (b) Output Stokes spectrum. Birefringence Δn: □ 10^{-6} *Random1 (0.6, 0.25, 0.76)*; --- 10^{-6} *Random2 (0.3, 0.7, 0.65)*; L=1000m. ○ 10^{-6} *Random3 (0.58, 0.58, 0.58)*; * 10^{-6} *Random4 (0.1, 0.9,0.42)*; — 10^{-10} no pol (0,0,0); P_{1x0} = 1.0 mW, P_{1y0} = 1.0 mW, P_{2x0} = 1.0 mW, P_{2y0} = 80.0 mW.	**88**
Figure 5.7:	(a) Output pump spectrum, (b) output Stokes spectrum. Birefringence Δn: □ 10^{-6} *Random1 (0.6, 0.25, 0.76)*; --- 10^{-6} *Random2 (0.3, 0.7, 0.65)*; L=1000m. ○ 10^{-6} *Random3 (0.58, 0.58, 0.58)*; * 10^{-6} *Random4 (0.1, 0.9,0.42)*; — 10^{-10} no pol (0,0,0); P_{1x0} = 10.0 mW, P_{1y0} = 1.0 mW, P_{2x0} = 60.0 mW, P_{2y0} = 1.0 mW.	**89**
Figure 6.1:	Schematic arrangement of SBS in an optical fiber of length L. E_{1x} –	

	Pump wave, E_{1y} – Pump wave, E_{2x} – Stokes wave, E_{2y} – Stokes wave, E_{3x} – anti-Stokes wave, E_{3y} – anti-Stokes wave.	**92**
Figure 6.2:	Output pump spectra. $\boldsymbol{S}$=(0.1, 0.9, 0.42). L=45m. $P_{1x}=P_{1y}$=1mW. (a) $P_{2x}=P_{2y}=P_{3x}=P_{3y}$=0.1mW; (b) $P_{2x}=P_{2y}=P_{3x}=P_{3y}$=0.2mW; (c) $P_{2x}=P_{2y}=P_{3x}=P_{3y}$=0.3mW; (d) $P_{2x}=P_{2y}=P_{3x}=P_{3y}$=0.4mW; (e) $P_{2x}=P_{2y}=P_{3x}=P_{3y}$=0.5mW; (f) $P_{2x}=P_{2y}=P_{3x}=P_{3y}$=0.6mW. —— : Δn =$10^{-4}$; —••—•• : Δn =$10^{-5}$; —•—•— : Δn =$10^{-6}$; - - - : Δn =$10^{-10}$ $\boldsymbol{S}$=(0, 0, 0).	**99**
Figure 6.3:	(A) $\Delta\upsilon_B$ dependence on Δn; (B) *Ratio* dependence on Δn. L=45m, $\boldsymbol{S}$=(0.1, 0.9, 0.42). (a) $P_{2x}=P_{2y}=P_{3x}=P_{3y}$=0.1mW; (b) $P_{2x}=P_{2y}=P_{3x}=P_{3y}$=0.2mW; (c) $P_{2x}=P_{2y}=P_{3x}=P_{3y}$=0.3mW; (d) $P_{2x}=P_{2y}=P_{3x}=P_{3y}$=0.4mW; (e) $P_{2x}=P_{2y}=P_{3x}=P_{3y}$=0.5mW; (f) $P_{2x}=P_{2y}=P_{3x}=P_{3y}$=0.6mW.	**100**
Figure 6.4:	Output pump spectra. $\boldsymbol{S}$=(0.1, 0.9, 0.42). L=45m. $P_{1x}=P_{1y}$=1mW. (a) $P_{2x}=P_{2y}=P_{3x}=P_{3y}$=0.7mW; (b) $P_{2x}=P_{2y}=P_{3x}=P_{3y}$=0.8mW; (c) $P_{2x}=P_{2y}=P_{3x}=P_{3y}$=0.9mW; —— : Δn =$10^{-4}$; —••—•• : Δn =$10^{-5}$; —•—•— : Δn =$10^{-6}$; - - - : Δn =$10^{-10}$ $\boldsymbol{S}$=(0, 0, 0).	**102**
Figure 6.5:	(A) $\Delta\upsilon_B$ dependence on Δn; (B)-(C) *Ratio* dependence on Δn. L=45m, $\boldsymbol{S}$=(0.1, 0.9, 0.42). (a) $P_{2x}=P_{2y}=P_{3x}=P_{3y}$=0.7mW; (b) $P_{2x}=P_{2y}=P_{3x}=P_{3y}$=0.8mW; (c) $P_{2x}=P_{2y}=P_{3x}=P_{3y}$=0.9mW.	**103**
Figure 7.1:	ASW power distribution inside the optical fiber. (a) Gain *and* Loss regime: P_{20}=10mW; (b) Gain *or* Loss regime: P_{20}=0mW. n=1.48, γ_e=0.902, λ=1550nm, ρ_0=2.21 g/cm^3, v=5616 m/s, Γ_B=0.1 GHz, α=0.2 dB/km, L=350m, P_{10}=10mW, P_{30}=10mW.	**110**
Figure 7.2:	NAND gate switching contrast plots. (a) Configuration I: Low threshold: 54.7%, High threshold: 74.8%, Tolerance: 20.6%. (b) Configuration II: Low threshold: 35.8%, High threshold: 87.8%, Tolerance: 52.7%. (c) Configuration III: Low threshold: 5.9%, High threshold: 87.7%, Tolerance: 82.8%.	**111**
Figure 7.3:	Output ASW power spectra. (a) ‘0 0’ input, (b) ‘0 1’ input, (c) ‘1 0’ input, (d) ‘1 1’ input.	**112 -113**
Figure 7.4:	NOT gate switching contrast plots. (a) Configuration IV: Low threshold: 38.9%, High threshold: 91.1%, Tolerance: 52.9%. (b)Configuration V: Low threshold: 13.3%, High threshold: 90.0%, Tolerance: 77.6%.	**114**
Figure 7.5:	Schematic of Configuration VI: AND gate.	**116**
Figure 7.6:	AND gate switching contrast plots. Configuration VI: Low threshold: 40.2%, High threshold: 83.1%, Tolerance: 42.3%. Configuration VII: Low threshold: 16.1%, High threshold: 77.1%, Tolerance: 61.8%.	**116**
Figure 7.7:	Schematic of Configuration VII: AND gate.	**117**
Figure 7.8:	Schematic of Configuration IX: OR gate.	**119**
Figure 7.9:	OR gate switching contrast plot. Low threshold: 6.8%, High threshold: 88.9%, Tolerance: 83.0%.	**120**
Figure 7.10:	(a) Schematic of configuration X: OR gate, (b) OR gate switching contrast plot, Low threshold: 7.04%, High threshold: 90.6%,	

	Tolerance: 83.6%.	**121**
Figure 7.11:	(a) Schematic of configuration XI: OR gate, (b) OR gate switching contrast plot, Low threshold: 7.22%, High threshold: 89.6%, Tolerance: 82.4%.	**122**
Figure 7.12:	Flow chart for NOT gate of configuration V.	**124**
Figure 7.13:	Flow chart for NOT gate of configuration IV.	**125**
Figure 7.14:	Flow chart for NAND gate of configurations I and II.	**126**
Figure 7.15:	Flow chart for NAND gate of configuration III.	**128**
Figure 7.16:	NOT experimental setup for test of NAND/NOT gates. (a) Configurations I-IV, (b) Configuration V. DFB: Distributed Feedback, RF: radio frequency, C: circulator, CC: fiber coupler, FUT: fiber under test, I: isolator, EOM: Electro-Optic Modulator, FBG: Fiber Bragg Grating, PC: polarization controller, EDFA: Erbium-doped fiber amplifier, DAQ: Data Acquisition.	**131**
Figure 7.17:	Configuration VI: AND gate. DFB: Distributed Feedback, RF: radio frequency, C: circulator, CC: fiber coupler, RR: ring resonator, FUT: fiber under test, I: isolator, EOM: Electro-Optic Modulator, FBG: Fiber Bragg Grating, PC: polarization controller, EDFA: Erbium-doped fiber amplifier, DAQ: Data Acquisition.	**133**
Figure 7.18:	Configuration VII: AND gate. DFB: Distributed Feedback, RF: radio frequency, C: circulator, CC: fiber coupler, RR: ring resonator, FUT: fiber under test, I: isolator, EOM: Electro-Optic Modulator, FBG: Fiber Bragg Grating, PC: polarization controller, EDFA: Erbium-doped fiber amplifier, DAQ: Data Acquisition.	**134**
Figure 7.19:	Configuration IX: OR gate. DFB: Distributed Feedback, RF: radio frequency, C: circulator, CC: fiber coupler, RR: ring resonator, FUT: fiber under test, I: isolator, EOM: Electro-Optic Modulator, FBG: Fiber Bragg Grating, PC: polarization controller, EDFA: Erbium-doped fiber amplifier, DAQ: Data Acquisition.	**136**
Figure 7.20:	Configuration XI: OR gate. DFB: Distributed Feedback, RF: radio frequency, C: circulator, CC: fiber coupler, RR: ring resonator, FUT: fiber under test, I: isolator, EOM: Electro-Optic Modulator, FBG: Fiber Bragg Grating, PC: polarization controller, EDFA: Erbium-doped fiber amplifier, DAQ: Data Acquisition.	**139**

List of Tables

Table 4.1: Simulation results for the experimental setup...................................... **66**
Table 7.1: Simulation Parameters... **109**

List of Acronyms

DFB:	Distributed Feedback
RF:	Radio Frequency
C:	circulator
CC:	Fiber Coupler
RR:	Ring Resonator
FUT:	Fiber Under Test
I:	Isolator
EOM:	Electro-Optic Modulator
FBG:	Fiber Bragg Grating
PC:	Polarization Controller
EDFA:	Erbium-doped fiber amplifier
DAQ:	Data Acquisition
eVOA:	Electronic Variable Optical Attenuator
AOM:	Acoustic-Optic Modulator
BGS:	Brillouin gain spectrum
BLS:	Brillouin loss spectrum
BOFDA:	Brillouin Optical Frequency Domain Analysis
BOTDA:	Brillouin Optical Time Domain Analysis
BOTDR:	Brillouin Optical Time Domain Reflectometer
CW:	Continuous wave
PW:	Pump wave
SW:	Stokes wave
ASW:	Anti-Stokes wave
AW:	Acoustic wave
DBS:	Distributed Feedback laser
EM	Electromagnetic
EOM:	Electro-Optic Modulator
FWHM:	Full width at Half Maximum
ODPA:	Optical Differential Parametric Amplification
OSA:	Optical Spectrum Analyzer
OTDA:	Optical Time Domain Analysis
OTDR:	Optical Time Domain Reflectometer
PM:	Polarization Maintaining
PMF:	Polarization Maintaining Fiber
SBS:	Stimulated Brillouin Scattering
SNR:	Signal-to-Noise Ratio
SOP:	State of Polarization
PDL:	Polarization Dependent Loss
PMD:	Polarization Mode Dispersion
HOM:	High-Order Mode
LHS:	Left-hand side
RHS:	Right-hand side
SMF:	Single-mode fiber
AM:	Amplitude-Modulated

UPA:	Undepleted Pump Approximation
RK4	Fourth Order Runge-Kutta
RK6	Sixth Order Runge-Kutta
LP:	Linear Polarization or Linearly Polarized
LHP:	Linearly Horizontally Polarized
LVP:	Linearly Vertically Polarized
L+45P:	Linear +45° Polarized
L-45P:	Linear -45° Polarized
LCP:	Left Circularly Polarized
RCP:	Right Circularly Polarized
BOCDA:	Brillouin optical correlation-domain analysis
MZI:	Mach-Zehnder Interferometer
SOA:	Semiconductor Optical Amplifiers
HNLF:	Highly Nonlinear Fiber

Chapter 1

Introduction

1.1 Overview

In 1920, a new kind of light scattering was discovered by Leon Brillouin – Brillouin scattering – which occurs as a result of the interaction of light with a transparent material's temporal periodic variations in density and refractive index. The result of this interaction between the light wave and the material is a change in the momentum of the light wave (frequency and energy) along preferential angles, similar to the diffraction off a moving grating. Many advances have since been made in the study of Brillouin scattering, in particular in the field of fiber sensing and fiber optics.

This thesis focuses on the investigation and applications of Brillouin scattering in optical fibers. The current chapter introduces the background, motivation, and contributions of the research work. Section 1.2 describes previously obtained solutions for SBS, which are numerical with analytical portions, and illustrates the motivation of developing a fully analytical solution of the Brillouin amplification problem valid for an arbitrary high depletion. Section 1.3 provides an overview of existing optical phase modulation devices and techniques and their limitations, and presents an optical phase modulation technique based on the principles of SBS, which would mitigate the disadvantages of existing technologies. Section 1.4 focuses on the investigation of a more accurate model of the polarization-dependent SBS interaction, including the possibility of elliptical birefringence, and its effect on the SBS process. Section 1.5 presents a polarization-independent technique to accurately realize all-optical logic gates based on the principles of combined Brillouin gain and loss in an optical fiber. Section 1.6 explains the thesis contributions, and section 1.7 provides the thesis outline.

1.2 *3D parametric model*

Since the discovery of stimulated Brillouin scattering (SBS) in optical fibers, several mathematical models of the pump-probe interaction undergoing SBS in the steady-state regime have emerged, which are valid for pulse lengths greater than the phonon relaxation time [1]. The two-wave interaction is modeled by a system of ordinary differential equations, which in most cases [2, 3] has solved numerically. However, numerical solutions not lend themselves easily to the high pump wave depletion-related optimization procedures that are essential for applications in strain and temperature sensing. For example, distributed sensing, using an EDFA (Erbium Doped Fiber Amplifier) and distributed Raman amplifiers [4, 5, 6] has the potential to lead to high pump depletion and would require an appropriately accurate solution.

Several attempts have been made to find analytical solutions of this system of equations. The most common is the undepleted pump approximation (UPA), employed in [7], which imposes the assumption that the pump wave depletion, due to energy transfer between the pump and probe waves, is negligible. The lack of pump wave depletion is a coarse approximation which does not reflect the challenges of fiber sensing techniques.

In [8, 9] an analytical solution for a lossless fiber has been attempted without putting limits on the level of depletion. However, this attempt has been only partially successful – the system of ordinary differential equations has been reduced to a transcendental equation, which still has to be solved numerically.

An interesting technique has been used in [1] to find the analytical solutions for a lossy fiber, placing no limits on the level of depletion in the fiber. The system of ordinary differential equations has been reduced to a transcendental equation involving an integral, which, unfortunately, could only be evaluated numerically. As a result, neither intensity distribution along the fiber, nor Brillouin spectra could be expressed analytically. A variation of the perturbation technique has been used in [10] with the intention of obtaining an analytical solution for a lossy fiber. However, a solution in the zero-approximation with respect to the attenuation constant has been taken from [9], which, as described above, requires the numerical solutions of a transcendental equation. Contrary to the claim in [10], only a hybrid solution has been obtained, which extends the solution in [6] to a lossy fiber, but otherwise has similar limitations.

Therefore, there is still an unsatisfied need for a fully analytical solution of the Brillouin amplification problem valid for an arbitrary high depletion, as well as a model which would characterize the Brillouin amplification process and help mitigate the detrimental effects of spectral depletion.

1.3 SBS optical phase modulator

At present, there exists a multitude of electro-optic modulators (EOM), which are used to modulate the amplitude, frequency, phase and polarization of a beam of light [11, 12, 13, 14]. Among these modulators, phase modulation provides the highest quality of transmitted signal – though at the expense of a widened spectrum. In view of the benefits, optical phase modulation has various applications in the field of optical networks and data transmission.

The most common phase modulator uses a Lithium Niobate crystal ($LiNbO_3$) [15, 16, 17], which has an index of refraction that depends linearly on the applied electric field, and a phase linearly dependent on the index of refraction. As the electric field changes, the resulting phase is modulated. The achievable variation of the refractive index in Lithium Niobate is relatively small, requiring either large voltages or long electrode lengths to obtain sufficient phase modulation. Such modulators may also perform the task of amplitude modulation.

ThorLabs^{TM}, for example, produces Lithium Niobate phase modulators made of Titanium Indiffused Z-Cut $LiNbO_3$, which are especially designed to be integrated into transponders. The Lithium Niobate component is required for all-optical frequency shifting, and applications such as sensing and data encryption. These phase modulators are designed to operate in the 1550 nm range.

Jenoptik^{TM} produces integrated optical phase modulators, which employ a combination of Magnesium oxide (MgO) and Lithium niobate ($LiNbO_3$) crystals to realize phase modulation in the GHz range. An advantage with Jenoptik^{TM} phase modulators is that a relatively low modulation voltage is required to achieve the desired phase modulation, thus being suitable for wavelengths in the visible and infrared spectral range.

Other methods of optical phase modulation have also been employed. For example, optical phase modulation has been achieved in a traveling wave semiconductor laser amplifier [18]. In this work, the optically controlled phase modulation is independent of the signal wavelength.

In spite of advances made in the area of optical phase modulation, there is still a need in the industry for developing alternative methods of optical phase modulation and further improvements to optical networks.

1.4 Polarization effects in SBS

In recent years, due to its robustness, low threshold power, and simplicity of operation, stimulated Brillouin scattering (SBS) has become a favourable underlying mechanism in fiber-base devices used for both sensing and telecommunication applications [4, 19, 20, 21]. Since birefringence is a detrimental effect for both, it is important to devise a comprehensive characterization of the SBS process in the presence of birefringence in an optical fiber, so that a prediction of the Brillouin frequency shift and birefringence variation over different sensing lengths can be made. All previous theoretical works [19, 22, 23, 24, 25, 26, 27] are related to the Brillouin gain variation due to the state of polarization (SOP) change. Although the effects of fiber birefringence on Brillouin frequency shift and linewidth have been studied experimentally [28], no report has been made regarding the Brillouin frequency shift associated with the SOP and birefringence change in relation to the fiber position.

A quantitative study of the fiber birefringence versus frequency shift is essential in finding the maximum impact of the fiber birefringence on the measurement precision of temperature and strain, for distributed Brillouin optical time domain analysis (BOTDA) or Brillouin optical time domain reflectometry (BOTDR) sensors, since it will be helpful in designing the best suitable fiber for BOTDA or BOTDR applications as well as optimizing system design.

Early works which investigated the polarization effects on SBS in optical fibers [22, 23, 24, 25] showed that the Stokes gain is strongly dependent on polarization effects, and in [29], this theoretical work was experimentally confirmed. [26] examines the applications of optical birefringence in SBS sensing for strain and temperature measurements, while [19] devises a technique to overcome the sensitivity of pulse delay to polarization perturbations, enhancing SBS slow light delay. In [27], a vector formalism was used to characterize the effects of birefringence on the SBS interaction. One such effect was signal broadening as a result of polarization effects. However, only linearly polarized (LP) pump and signal waves were investigated in [26, 27]. Additionally, [27] assumed an undepleted pump regime, which has applications only for short fiber lengths, while the BOTDA and BOTDR often operate on long fiber distances; the convolution of the birefringence and depletion would induce much larger distortion on the Brillouin spectrum, and hence lower the temperature and strain resolution. Thus the undepleted and linear polarized models are not adequate to address real problems.

The above mentioned works [23, 24, 25, 27, 29], however, treat a steady-state SBS system where both the pump and Stokes waves are continuous. Additionally, none of these references investigated the effect of birefringence and polarization on the spectral distortion – namely Brillouin frequency shift of pulses undergoing SBS. In [19], though pulse length was taken into account, Brillouin spectrum distortion was not. More importantly, the impact of the nonlinear effect under different pump powers convoluted with the fiber birefringence and its impact on the Brillouin spectrum shape and peak shift have not yet been examined. An extension of [27] was published in the work [30], whereby signal pulses were taken into consideration and pulse distortion was observed. However, this work still did not take into consideration the most general case of birefringence, which is elliptical birefringence. Finally, none of the aforementioned works investigated the effects of polarization and birefringence in the combined Brillouin gain and loss regime in an optical fiber.

The authors feel that it was important to investigate a more accurate model of the polarization-dependent SBS interaction – including elliptical birefringence. Besides being able to accommodate the most general case of elliptical birefringence, the effects of polarization mode dispersion (PMD), polarization dependent loss (PDL), phonon resonance structures, pulse length, as well as the overall attenuation of the fiber must be taken into account. Finally, since spectral distortion is detrimental for fiber sensing and telecommunications, an in depth investigation into the effects of birefringence and polarization on the SBS process, and methods of minimizing these effects have been investigated.

1.5 Photonic Logic

In recent years, photonic computing has received considerable attention due to its numerous applications, such as high-speed optical signal processing, which would yield much faster computing times and higher bandwidths. For this reason, optical logic has been the focus of many research efforts, and several schemes to improve conventional logic gates have been proposed. In [31, 32, 33], optically programmable and reversible Boolean logic units are proposed, consisting of a circuit which is designed by the implementation of a 2 x 2 optoelectronic switch [34]. The drawback of this scheme is that the switching speed of the 2 x 2 switching element is about 10^6 times slower compared to, for example, a semiconductor optical amplifier (SOA) based interferometric switch. In view of the speed limitations inherent in electronic circuits, all-optical data processing devices have become the focus of many research efforts, especially in optical fibers, as these devices provide compatibility to fiber links with low connection loss and easy implementation. One category of such devices is the all-optical logic gate, which is projected to be a main component in future integrated photonic circuits.

Some established techniques for achieving functional all-optical logic gates include the use of integrated optical and waveguide structure Mach-Zehnder interferometers (MZIs) [35, 36, 37] that are often limited by back-reflections of the optical signal, which are minimized by extending the cladding and substrate layers; the use of nonlinear optical processes in semiconductor optical amplifiers (SOA), such as four-wave mixing [38] and cross-gain modulation [39, 40, 41]; and the use of a combination thereof – integrated Mach-Zehnder interferometers based on SOA [42, 43, 44, 45]. SOA-based techniques are often limited by the carrier’s recovery time which in turn slows down the operation of the device. In addition, these techniques often require the use of multiple SOAs to achieve functional all-optical logic gates, and fall victim to additional noise such as spontaneous emission noise [46, 47], time dependent modulation due to time jitter, and birefringence induced signal distortion.

Additionally, there exist logic gates proposed by terahertz optical asymmetric demultiplexer (TOAD) based switches [48, 49, 50, 51]. The TOAD consists of a loop mirror and a nonlinear element, usually an SOA, which is positioned asymmetrically in the fiber loop. In addition to the limitations of the SOA mentioned above, the TOAD scheme suffers from a walk-off problem due to dispersion, intensity losses due to beam splitter, optical circulators, etc. In addition, if there is an attempt to remedy the aforementioned finite propagation time of the pulse across the SOA by decreasing the offset length, the decrease in effective SOA length causes a reduction in contrast ratio of the TOAD switching mechanism, which hinders the functionality of the logic gate.

Techniques, based on the design of simple passive optical components, also exist. These techniques include optical logic parallel processors [52] and the multi-output polarization-encoded optical shadow-casting scheme [53]. Both schemes are based on the polarization of light, whereby the switching mechanism consists of the polarization switching of output light. Drawbacks of such schemes include polarization instability, inherent in any polarization-dependent device, and detrimental diffraction effects.

Other such techniques also exist, such as using a Kerr nonlinear prism to realize binary-to-gray-to-binary code conversion, whereby the switching mechanism is the deviation of light due to nonlinear refraction [54]. However, to function correctly, such a scheme requires several such prisms and mirrors to be aligned in series, the configuration of which is both bulky and requires extensive calibration. In addition, very large intensities are required for the function of the proposed setup.

Fiber nonlinearity-based techniques provide comparable functionality, without the limitations mentioned above. Among fiber nonlinearity-based logic gates, one of the techniques includes using the Kerr effect in highly nonlinear fibers (HNLF) to induce birefringence, thereby rotating the polarization state of an output light wave [55, 56], which represents the optical gate operation with an ultimate speed limitation above 100 Gb/s. However, one limitation of this technique is that long fiber lengths introduce polarization instabilities in conventional single mode fibers. A relatively short fiber length of 2 km was used to realize the XOR gate in [55]. Since polarization rotation is necessary in [55, 56], the presence of birefringence is another limitation of the technique, which may cause polarization mode dispersion (PMD) of the optical signal.

Therefore, there is a need for a polarization-independent technique to accurately realize all-optical logic gates, which could be realized in the frequency domain through the combined Brillouin gain and loss spectrum. Polarization maintaining fibers (PMFs) help to eliminate the influence of polarization mode dispersion (PMD) [57], as well as other polarization maintaining applications [58, 59]. Using PMFs ensures that the technique based on combined Brillouin gain and loss is free of polarization induced signal fluctuations at different positions, which cause spectral distortion.

1.6 Thesis contributions

In this thesis, the mechanisms of stimulated Brillouin scattering, and combined Brillouin gain and loss, are investigated and applied to the development and improvement of current technologies.

Firstly, highly accurate, fully analytic solutions for the Brillouin amplification process have been discovered, void of any underlying assumptions about the pump and Stokes waves. These analytic solutions are valid in the 0-100% depletion regimes, which are detrimental for sensing applications, since depletion and spectral distortion makes it difficult to accurately measure the center frequency of the spectrum. It is experimentally confirmed that the reported analytic solution can account for spectral distortion and pump depletion in the parameter space that is relevant to Brillouin fiber sensor applications. The fully analytic solutions allowed for the construction of a *3D parametric model* which has been used to characterize the SBS interaction, and as a tool to avoid the undesirable spectral distortion via limitations of the parameter space that is relevant to Brillouin fiber sensing applications. The *3D parametric model* also has applications in photonic logic and, in particular, in the optimal construction of logic gates.

Furthermore, an improved method of phase-modulation, based on the principles of stimulated Brillouin scattering, and an optical phase network employing the same have been developed. This proposed optical-phase modulator mitigates the drawbacks of current phase-modulation technologies, which require either large voltages or long electrode lengths to obtain sufficient phase modulation, as in the case of Lithium Niobate based optical phase modulators.

Additionally, the most general model of elliptical birefringence in an optical fiber has been developed for a steady-state and transient stimulated Brillouin scattering (SBS) interaction, as well as the combined Brillouin gain and loss regime. The impact of the elliptical birefringence is to induce a Brillouin frequency shift and distort the Brillouin spectrum – which varies with different light polarizations, pulse widths, and degrees of birefringence. The model presented in this thesis investigates the effects of birefringence on the Brillouin process, and proposes methods of maintaining a pulse fidelity and full width at half maximum (*FWHM*), as compared to non-polarized light in a non-birefringent fiber – providing a valuable prediction tool for distributed sensing applications and data transmission. This tool also allows for the avoidance, or mitigation, of detrimental spectral distortion effects caused by birefringence in optical fibers, providing a means of increasing the ease of operation and efficiency of fiber sensing technology.

Finally, configurations to realize all-optical NAND/NOT/AND/OR logic gates in the frequency domain, based on the principles of combined Brillouin gain and loss in an optical fiber, have been proposed. Through the optimization of the pump depletion and gain saturation in the combined gain and loss process, switching contrasts of 20-83% have been simulated for different configurations. The proposed gates are free from polarization instabilities and polarization mode dispersion (PMD) which plague current fiber nonlinearity-based techniques of optical gate construction. A general method of finding additional optical gate constructions has been proposed in the form of a computer algorithm, as well as using the *3D parametric model* described in Chapter 3. Finally, experimental configurations have been proposed for the testing and construction of the proposed optical gates.

1.7 Thesis outline

This thesis contains eight Chapters and is organized as follows.

Chapter 2 is dedicated to the study of the principles of stimulated Brillouin scattering (SBS), including the concepts of combined Brillouin gain and loss. Standard coupled wave equations will be derived to mathematically describe the behaviour of the amplitudes of the interacting waves in the SBS interaction.

Chapter 3 will provide a fully analytical solution of the Brillouin amplification problem, valid for an arbitrarily high depletion, as well as a *3D parametric model*, which can be used to investigate the Brillouin amplification process.

Chapter 4 will propose an optical phase modulator based on the principles of stimulated Brillouin scattering, which would avoid or mitigate the disadvantages of existing technologies.

Chapter 5 will present a model which describes the complete SBS picture, including birefringence and polarization effects. The most comprehensive SBS equations, considering elliptical birefringence effects in an optical fiber, will be presented. Chapter 6 will present a comparable model for the regime of combined Brillouin gain and loss.

Chapter 7 will describe in detail a polarization-independent technique to construct all-optical logic gates based on the principles of stimulated Brillouin scattering and combined Brillouin gain and loss in an optical fiber.

Chapter 8 will conclude the work presented in the thesis, and suggest some possible future directions.

Chapter 2

Physics of Brillouin Scattering

2.1 Introduction

The present chapter is dedicated to the study of the principles of stimulated Brillouin scattering (SBS). Section 2.2 explains the mechanism of light scattering in different media, while sections 2.3 and 2.4 apply these concepts to particular cases of Brillouin scattering. Section 2.3 provides an overview of spontaneous Brillouin scattering while section 2.4 describes in detail the case of stimulated Brillouin scattering. Section 2.5 provides an overview of the concepts of polarization and birefringence in optical fibers. Section 2.6 provides a summary.

2.2 Light Scattering

When an electro-magnetic (EM) wave [60], or light, is launched into a material such as an optical fiber, the incident EM wave interacts with the molecules of the material, resulting in a scattering phenomenon. The result is a scattering spectrum. Depending on the intensity of the incident light, we may get either *spontaneous* scattering for low intensities of incident light, or *stimulated* scattering for high intensities of incident light. Figure 2.1 shows a typical spectrum for spontaneous scattering from solid state matter. In inelastic scattering, the light having a lower frequency than the incident light is called the *Stokes branch*, while the light having a higher frequency than the incident light is called the *anti-Stokes branch*.

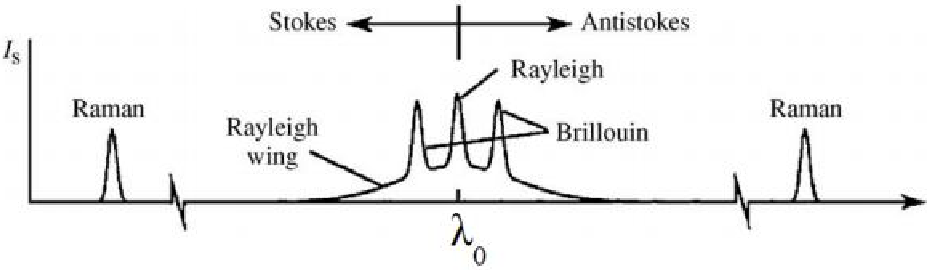

Figure 2.1 Schematic of the observed scattered light intensity [1].

Brillouin scattering arises from the interaction of light with propagating density waves, caused by the part of the $\chi^{(3)}$-nonlinearity of the medium related to acoustic phonons [1, 61]. Brillouin scattering may occur *spontaneously* when incident light scatters off the sounds waves that are present in thermal equilibrium. Due to the Doppler effect, the frequency of the scattered light is downshifted from the frequency of the incident light. Because of this difference, the incident and scattered waves beat together, causing variations of the density of the media, which in turn causes refractive index variations. In optical fibers, the incident light scatters off the refractive index variations in the direction opposite to the direction of propagation of the incident light, thus giving rise to the *Brillouin scattering* phenomenon.

Brillouin Scattering may also be *stimulated*. As mentioned above, for intense beams such as laser light, traveling in a medium such as an optical fiber, the interaction of the thermally excited acoustic wave “seeds” the resonance SBS. This phenomenon is known as *electrostriction*, during which the tendency of materials is to become more dense in regions of high optical intensity. *Electrostriction* creates a dynamic acoustic grating, which in turn causes variations in the refractive index of the material. As a result, laser light may undergo stimulated Brillouin scattering (SBS) due to the variations in the medium. SBS is frequently encountered when narrow-band optical signals are amplified in a fiber amplifier. In fact, SBS introduces the most stringent power limit, commonly referred to as the Brillouin threshold, for the amplification or even passive propagation of narrow-band optical signals, such as those used in telecommunications [62, 63].

2.3 Spontaneous Brillouin Scattering

It is important to develop a macroscopic description of the light scattering process, whereby the light scattering process occurs as a result of fluctuations in material density and temperature. Assuming that the scattering volume, *V*, may be divided into smaller volumes, *V'*, whereby all the atoms in *V'* have the characteristic that they radiate in phase in the θ direction. Letting $\Delta\epsilon$ be the fluctuation of the dielectric constant in the volume *V'*, then we have $\Delta\varepsilon = \Delta\chi$, where χ is the susceptibility of the material. This equality is deduced from the relation $\varepsilon = 1 + \chi$. Due to this change in optical susceptibility, an additional polarization is developed, where $\tilde{E}_0$ is the electric field.

$$\tilde{P} = \Delta\chi\tilde{E}_0 \tag{2.1}$$

As a result, the dipole moment becomes

$$\tilde{p} = \varepsilon_0 V'\tilde{P} = \varepsilon_0 \Delta\varepsilon V'\tilde{E}_0 \tag{2.2}$$

The change in dielectric constant can also be expressed as

$$\Delta\varepsilon = \left(\frac{\partial\varepsilon}{\partial\rho}\right)_T \Delta\rho + \left(\frac{\partial\varepsilon}{\partial T}\right)_\rho \Delta T \tag{2.3}$$

It is also important to note that the electrostrictive constant of the material, γ_e, can be expressed as

$$\gamma_e = \left(\rho\frac{\partial\varepsilon}{\partial\rho}\right)_{\rho=\rho_0} \tag{2.4}$$

From the field of acoustics [64], the equation of motion for a pressure wave is as follows

$$\frac{\partial^2\Delta\tilde{p}}{\partial t^2} - \Gamma'\nabla^2\frac{\partial\Delta\tilde{p}}{\partial t} - v^2\nabla^2\Delta\tilde{p} = 0 \tag{2.5}$$

Here v is the velocity of sound inside the material, which is defined thermodynamically as

$$v^2 = \left(\rho\frac{\partial p}{\partial\rho}\right)_s \tag{2.6}$$

And Γ' is the damping parameter, defined as

$$\Gamma' = \frac{1}{\rho}\left[\frac{4}{3}\eta_s + \eta_b + \frac{\kappa}{C_p}(\gamma - 1)\right] \tag{2.7}$$

where η_s is the shear viscosity coefficient, η_b is the bulk viscosity coefficient, γ is the adiabatic index, and κ is the thermal conductivity.

To illustrate the nature of the acoustic wave, we propose the following wave equation

$$\Delta\tilde{p} = \Delta p e^{i(qz-\Omega t)} + c.c. \tag{2.8}$$

By substituting (2.8) into the equation (2.5), we see that q and Ω are related by a dispersion relation of the form

$$\Omega^2 = q^2\left(v^2 - i\Omega\Gamma'\right) \tag{2.9}$$

Which, after rearranging, can be written in the form

$$q^2 \approx \frac{\Omega^2}{v^2}\left(1 + \frac{i\Omega\Gamma'}{v^2}\right) \tag{2.10}$$

Which leads to the following expression

$$q \approx \frac{\Omega}{v} + \frac{i\Gamma}{2v} \tag{2.11}$$

Where $\Gamma = \Gamma_B$ is the phonon decay rate, and is related to q in the following way

$$\Gamma_B = q^2\Gamma' \tag{2.12}$$

In terms of Brillouin scattering, the phonon decay rate can also be expressed as the inverse of the phonon lifetime, τ_B, as follows: $\Gamma_B = 1/\tau_B$. Assuming that the incident optical field obeys the driven wave equation,

$$\nabla^2\tilde{E} - \frac{n^2}{c^2}\frac{\partial^2\tilde{E}}{\partial t^2} = \frac{1}{\varepsilon_0 c^2}\frac{\partial^2\tilde{P}}{\partial t^2} \tag{2.13}$$

and is described by the following expression

$$\tilde{E}_0(z,t) = E_0 e^{i(\mathbf{k}\cdot\mathbf{r} - \omega t)} + c.c. \tag{2.14}$$

combining the expressions (2.8) and (2.14), it becomes apparent that the scattered field obeys the following wave equation

$$\nabla^2\tilde{E}-\frac{n^2}{c^2}\frac{\partial^2\tilde{E}}{\partial t^2}=-\frac{\gamma_e C_s}{c^2}\begin{bmatrix}(\omega-\Omega)^2 E_0\Delta p^* e^{i(k-q)\cdot r-i(\omega-\Omega)t}\\ +(\omega+\Omega)^2 E_0\Delta p e^{i(k+q)\cdot r-i(\omega+\Omega)t}+c.c.\end{bmatrix} \tag{2.15}$$

Where C_s is the compressibility at constant entropy, and $\boldsymbol{k}$ is the wavevector. In the above expression, the $(\omega\text{-}\Omega)$ term leads to Stokes wave scattering, while the $(\omega+\Omega)$ terms leads to anti-Stokes scattering.

In *Stokes scattering*, the scattered wavevector, $\boldsymbol{k}_2$, may be expressed in terms of the incident and acoustic wavevector, $\boldsymbol{k}_1$, and $\boldsymbol{q}$, as follows: $\boldsymbol{k}_2 = \boldsymbol{k}_1 - \boldsymbol{q}$, having a frequency $\omega_2 = \omega_1 - \Omega$. The frequency and wavevector of the incident field, ω_1 and $\boldsymbol{k}_1$, are related by: $\omega_1 = |\boldsymbol{k}_1|c/n$, while the frequency and wavevector of the acoustic wave, Ω and $\boldsymbol{q}$, are related as follows: $\Omega = |\boldsymbol{q}|v$.

Efficient scattering can occur only if the frequency and wavevector of the scattered wave, ω_2 and $\boldsymbol{k}_1$, are related by the dispersion relation for optical waves, namely: $\omega_2 = |\boldsymbol{k}_2|c/n$.

Stokes scattering is illustrated on Figure 2.2 below, with scattering angle θ.

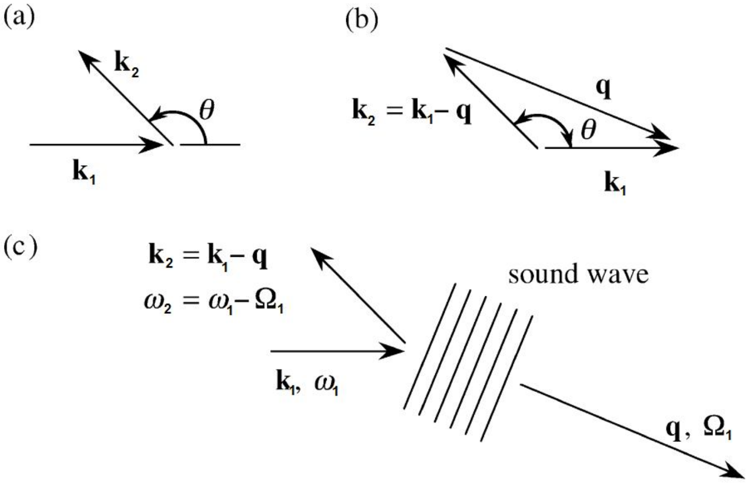

Figure 2.2. Stokes Brillouin scattering [1].
(a) Relative orientations of the wavevectors $\boldsymbol{k}_1$ and $\boldsymbol{k}_2$, (b) $\boldsymbol{k}_1$, $\boldsymbol{k}_2$ and $\boldsymbol{q}$ relationship,
(c) Schematic of SBS interaction.

Since $|\boldsymbol{k}_1| \approx |\boldsymbol{k}_2|$, we have the following relation: $|\boldsymbol{q}| = 2|\boldsymbol{k}_1|sin(\theta/2)$. According to the dispersion relation $\Omega = |\boldsymbol{q}|v$, we therefore have the following expression for the acoustic frequency

$$\Omega_1 = 2n\omega_1(v/c)sin(\theta/2) \tag{2.16}$$

Taking into account that the majority of scattering occurs for $\theta=180°$, the maximum frequency shift becomes: $\Omega_B = 2n\omega_1(v/c)$. As such, *Stokes scattering* can be visualized from a retreating acoustic wave.

The same analysis may be applied to the case of *anti-Stokes scattering*. The scattered wavevector, $\boldsymbol{k}_3$, may be expressed in terms of the incident and acoustic wavevectors, $\boldsymbol{k}_1$, and $\boldsymbol{q}$, as follows: $\boldsymbol{k}_2 = \boldsymbol{k}_1 + \boldsymbol{q}$, having a frequency $\omega_3 = \omega_1 + \Omega$. As before, efficient scattering can occur only if the frequency and wavevector of the scattered wave, ω_3 and $\boldsymbol{k}_1$, are related by the dispersion relation for optical waves, namely: $\omega_3 = |\boldsymbol{k}_3|c/n$.

Anti-Stokes scattering is illustrated on Figure 2.3 below, with scattering angle θ.

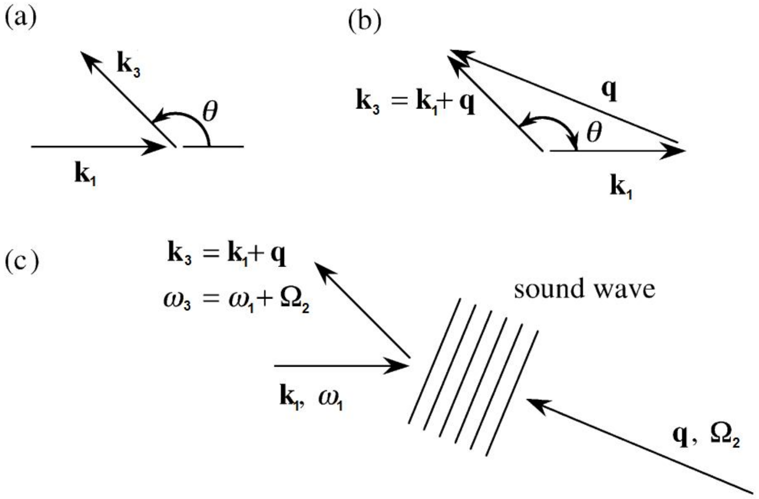

Figure 2.3. Anti-Stokes Brillouin scattering [1].

(a) Relative orientations of the wavevectors $\boldsymbol{k}_1$ and $\boldsymbol{k}_3$, (b) $\boldsymbol{k}_1$, $\boldsymbol{k}_3$ and $\boldsymbol{q}$ relationship,

(c) Schematic of SBS interaction.

Since $|\boldsymbol{k}_1| \approx |\boldsymbol{k}_3|$, we once again have the following relation: $|\boldsymbol{q}| = 2|\boldsymbol{k}_1|\sin(\theta/2)$. According to the dispersion relation $\Omega = |\boldsymbol{q}|v$, we therefore have the same expression for acoustic frequency as in expression (2.16)

$$\Omega_2 = 2n\omega_1(v/c)\sin(\theta/2) \tag{2.17}$$

Taking into account that the majority of scattering occurs for $\theta=0°$ for *anti-Stokes scattering*, the maximum frequency shift becomes: $\Omega_B=2n\omega_1(v/c)$. *Anti-Stokes scattering* can be visualized from an oncoming acoustic wave.

2.4 Stimulated Brillouin Scattering

The previous section 2.3 discussed the mechanisms of spontaneous Brillouin scattering, where the applied optical fields were sufficiently weak to leave the acoustic properties of the material unaltered. However, if the laser light is sufficiently intense, the incident and scattered field can beat together, creating a dynamic acoustic grating via *electrostriction*. The incident field will then scatter off the acoustic grating at the Stokes frequency and add constructively with the scattered, Stokes or anti-Stokes, field. In this way, the amplitudes of the acoustic grating and scattered light are reinforced. Though the $\chi^{(3)}$-nonlinearity of a medium is rather small, Brillouin scattering can grow exponentially to a large amplitude in optical fibers.

2.4.1 SBS Generator

There exist two conceptually different configurations in which SBS can be studied [1]. Figure 2.4 shows the configuration of the SBS generator, in which only the laser beam is applied externally, a pump wave with frequency ω_1, while both the Stokes wave with frequency ω_2, and the acoustic wave, are created from the noise within the region of interaction. The noise is typically generated by the scattering of pump laser light from thermally-generated density fluctuations (phonons).

Figure 2.4 SBS generator [1].

2.4.2 SBS Amplifier

Figure 2.5 shows the configuration for a SBS amplifier, in which both the laser and Stokes fields are applied externally. In this configuration, the pump and Stokes fields are counter-propagating, and a strong interaction takes place when the frequency of the injected Stokes wave is equal to that which would be created by the SBS generator. In this manuscript, the SBS amplifier configuration will be considered.

Figure 2.5 SBS amplifier [1].

2.4.3 Electrostriction

Electrostriction is the tendency of materials to acquire a higher overall density in the presence of an applied electric field. Certain third-order optical responses are caused by the electrostriction phenomenon, including stimulated Brillouin scattering (SBS) which is the focus of this thesis.

We can explain the origin of this effect by taking a look at the change in potential energy per unit volume of a material placed in the presence of an electric field *E*.

$$u = \frac{1}{2}\varepsilon\varepsilon_0 E^2 \tag{2.18}$$

Here ε is the relative dielectric constant, and ε_0 is the permittivity of free space. In the presence of the electric field $\vec{E}$, each molecule experiences a dipole moment

$$\vec{p} = \varepsilon_0 \alpha \vec{E} \tag{2.19}$$

Where α is the molecular polarizability. It follows that the energy of the molecule is

$$U = -\int_0^{\vec{E}} \vec{p} \cdot d\vec{E}' = -\frac{1}{2}\varepsilon_0 \alpha E^2 \tag{2.20}$$

As such, the resultant force acting on the molecule is given by

$$\vec{F} = -\nabla U = \frac{1}{2}\varepsilon_0 \alpha \nabla\left(E^2\right) \tag{2.21}$$

From expression (2.21), it is apparent that the force acting on the molecule pulls it into the region of increasing electric field strength. Hence, an applied electric field $\vec{E}$ onto a material will result in the molecules of the material, at the vicinity of the applied force, to be pulled in the direction of increasing field strength. As such, the density in this vicinity will increase, in turn causing the local index of refraction to change as well. The result is a dynamic acoustic grating along the length of the fiber, characterized by periodic differences in density, and consequently the index of refraction.

2.4.4 SBS Coupled wave equations and configuration

The previous section 2.4.3 described the mechanism of *electrostriction* by which the dynamic acoustic grating, inherent in stimulated Brillouin scattering, is created. In this section, we will describe the possible configurations of the laser lights and fiber which allow us to attain the electrostriction effect most efficiently, and derive the standard coupled wave equations related to each configuration.

An incident electric field at a certain frequency scatters off the refractive index variations, the scattered light being at the same frequency as the incident light. As such, the scattered light interacts constructively with the incident pulse which originally produced the acoustic disturbance, both mutually reinforcing each other's existence. The incident pulse, which may be either a Stokes or an anti-Stokes wave, is launched into the beginning of the fiber $z=0$, where z is the coordinate inside the fiber. The pump wave (PW) is launched into the opposite end of the fiber $z=L$, where L is the total length of the fiber. This configuration is shown on Figure 2.6 below.

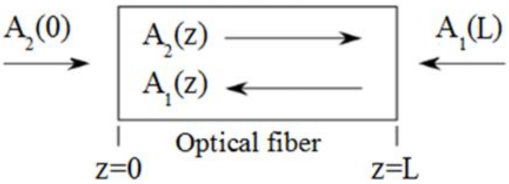

Figure 2.6 Schematic arrangement of SBS in a fiber of length *L*.
Pump and probe configuration: $A_1(z)$ – Pump wave, $A_2(z)$– probe wave (incident pulse).

Firstly, we consider the case when the incident pulse has a downshifted frequency as compared to the frequency of the PW, by a frequency of Ω_B=10-11 GHz, also known as the Brillouin frequency. Such a pulse is called the Stokes wave (SW), and is responsible for Brillouin *gain* in the SBS amplifier.

We begin with the equations representing the incident waves involved in the Brillouin interaction.

$$\tilde{E}_1(z,t) = A_1(z,t)e^{i(\mathbf{k}_1 z-\omega_1 t)} + c.c. \tag{2.22}$$

$$\tilde{E}_2(z,t) = A_2(z,t)e^{i(-\mathbf{k}_2 z-\omega_2 t)} + c.c. \tag{2.23}$$

Where $\tilde{E}_1$ represents the pump wave incident at the end of the fiber, and $\tilde{E}_2$ represents the pulse incident at the beginning of the fiber, or Stokes wave. $\boldsymbol{k}_1$, $\boldsymbol{k}_2$ are the wavevectors of the pump wave (PW) and Stokes waves (SW) respectively, and ω_1 and ω_2 are the frequencies of the PW and SW respectively. The acoustic wave may be expressed in terms of material density distribution, where $\Omega = \omega_1 - \omega_2$, $\boldsymbol{q} \approx 2\boldsymbol{k}_1$, and ρ_0 denotes the density of the material.

$$\tilde{\rho}_1(z,t) = \rho_0 + \left[\rho_1(z,t)e^{i(\mathbf{q}z-\Omega_1 t)} + c.c.\right] \tag{2.24}$$

The scattered field obeys the wave equation

$$\nabla^2 \tilde{E}_i - \frac{n^2}{c^2}\frac{\partial^2 \tilde{E}_i}{\partial t^2} = \frac{1}{\varepsilon_0 c^2}\frac{\partial^2 \tilde{P}_i}{\partial t^2}, \qquad i=1,2 \tag{2.25}$$

Where the polarization $\tilde{P}_i$ of the medium is given in terms of the electrostrictive constant, γ_e, the permittivity of free space, ε_0, mean density of the material ρ_0, and in terms of density $\tilde{\rho}(z,t)$.

$$\tilde{P}(r,t) = \frac{\varepsilon_0 \gamma_e}{\rho_0} \tilde{\rho}(z,t) \tilde{E}(z,t) \tag{2.26}$$

The equation of motion for a pressure wave, which we have used to describe the propagation of the acoustic wave inside the fiber, follows the acoustic wave equation

$$\frac{\partial^2 \Delta\tilde{p}}{\partial t^2} - \Gamma' \nabla^2 \frac{\partial \Delta\tilde{p}}{\partial t} - v^2 \nabla^2 \Delta\tilde{p} = 0 \tag{2.27}$$

Here v is the velocity of sound inside the material, Γ' is the damping parameter, defined as $\Gamma_B = q^2 \Gamma'$, where $\Gamma_B = 1/\tau_B$ is the inverse of the phonon lifetime, τ_B. Substituting equations (2.22)-(2.23) into (2.25) and equation (2.24) into (2.27), we get the following system of equations describing the interaction of the pump, Stokes and acoustic waves.

$$-\frac{\partial A_1}{\partial z} + \frac{1}{c/n} \frac{\partial A_1}{\partial t} = \frac{i\omega_1 \gamma_e}{2nc\rho_0} \rho_1 A_2 - \frac{1}{2} \alpha A_1 \tag{2.28}$$

$$\frac{\partial A_2}{\partial z} + \frac{1}{c/n} \frac{\partial A_2}{\partial t} = \frac{i\omega_1 \gamma_e}{2nc\rho_0} \rho_1^* A_1 - \frac{1}{2} \alpha A_2 \tag{2.29}$$

$$\left(\Omega_B^2 - \Omega_1^2 - i\Omega_1 \Gamma_B\right) \rho_1 = \frac{\gamma_e q_1^2}{4\pi} A_1 A_2^* \tag{2.30}$$

Where α is the fiber attenuation parameter, and $\mathbf{q}$ has been denoted as $\mathbf{q}_1$, and ρ has been denoted as ρ_1. The following approximations have been made to attain this system of equations: the phonon propagation distance is considered to be small compared to the distance over which the amplitude of the acoustic wave fluctuates [1]. For the optical waves, the slowly-varying amplitude approximation has been applied.

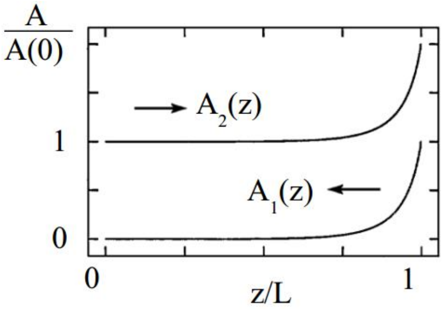

Figure 2.7 Schematic distribution of the pump and probe intensities during SBS [1].

Figure 2.7 above shows a typical intensity distribution of the pump and Stokes powers inside an optical fiber, in the steady state regime of SBS.

The incident pulse may also have an upshifted frequency as compared to the frequency of the PW, such a pulse is called the anti-Stokes wave (ASW), and is responsible for Brillouin *loss* in the SBS amplifier. The same analysis may be applied to obtain equations for this case, and the result will be very similar to the system of equations (2.28)-(2.30), with the difference that the Stokes wave parameters will be replaced by corresponding anti-Stokes parameters. In fact, from a physical point of view, since the PW is now downshifted from the ASW by the Brillouin frequency, the anti-Stokes may be viewed as a new 'pump wave' and the PW may be viewed as a new 'Stokes wave'.

2.4.5 Combined Brillouin gain and loss coupled wave equations and configuration

In this section we will derive the equations governing the SBS interaction for the case of simultaneous gain and loss. Following section 2.4.4, we may add an additional wave, representing the anti-Stokes wave to the pump and Stokes waves described by equations (2.22) and (2.23):

$$\tilde{E}_3(z,t) = A_3(z,t)e^{i(-k_3 z - \omega_3 t)} + c.c. \tag{2.31}$$

and an additional acoustic field, which results from the interaction of the PW and ASW

$$\tilde{\rho}_2(z,t) = \rho_0 + \left[\rho_2(z,t)e^{i(qz - \Omega_2 t)} + c.c.\right] \tag{2.32}$$

Repeating the analysis of section 2.4.4, we get the following system of equations, describing the interaction of the PW, SW, ASW and two acoustic waves [1, 65].

$$-\frac{dA_1}{dz}=\frac{i\omega_1\gamma_e}{2nc\rho_0}\rho_1 A_2+\frac{i\omega_1\gamma_e}{2nc\rho_0}\rho_2^* A_3-\frac{1}{2}\alpha A_1 \tag{2.33}$$

$$\frac{dA_2}{dz}=\frac{i\omega_2\gamma_e}{2nc\rho_0}\rho_1^* A_1-\frac{1}{2}\alpha A_2 \tag{2.34}$$

$$\frac{dA_3}{dz}=\frac{i\omega_3\gamma_e}{2nc\rho_0}\rho_2 A_1-\frac{1}{2}\alpha A_3 \tag{2.35}$$

$$\left(\Omega_B^2-\Omega_1^2-i\Omega_1\Gamma_B\right)\rho_1=\frac{\gamma_e q_1^2}{4\pi}A_1A_2^* \tag{2.36}$$

$$\left(\Omega_B^2-\Omega_2^2-i\Omega_2\Gamma_B\right)\rho_2=\frac{\gamma_e q_2^2}{4\pi}A_3A_1^* \tag{2.37}$$

Where $\Omega_1=\omega_1-\omega_2$, $\Omega_2=\omega_3-\omega_1$, $\boldsymbol{q}_1$ and $\boldsymbol{q}_2$ are the acoustic wavevectors defined as $\boldsymbol{q}_1=\boldsymbol{k}_1-\boldsymbol{k}_2\approx 2\boldsymbol{k}_1$ and $\boldsymbol{q}_2=\boldsymbol{k}_3-\boldsymbol{k}_1\approx 2\boldsymbol{k}_1$, where $\boldsymbol{k}_1$, $\boldsymbol{k}_2$ and $\boldsymbol{k}_3$ are the wavevectors of the PW, SW and ASW respectively, defined as $\left|\vec{k}_i\right|=n\omega_i/c$, $i=1,2,3$.

The configuration related to this case is shown in Figure 2.8, whereby both a Stokes wave and an anti-Stokes wave are launched into the beginning of the fiber ($z=0$), while a pump wave is launched into the end of the fiber ($z=L$) as usual. This setup allows for simultaneous Brillouin *gain and loss* to occur from the interaction of the lights inside the fiber.

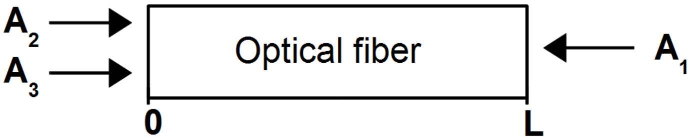

Figure 2.8 Schematic arrangement of SBS in a PMF of length *L*.
PW and pulse configuration: A_1 – pump wave, A_2 – Stokes wave, A_3 – anti-Stokes wave.

2.5 Polarization and birefringence

2.5.1 Polarization states

Polarization is a property of waves which can oscillate with more than one orientation [66, 67, 68]. Electromagnetic waves, such as light, exhibit polarization whereby the electric field vector traces out an ellipse. The shape and orientation of this ellipse (or line) defines the *polarization state*. The following Figure 2.9 shows some examples of the evolution of the electric field vector, with time (the vertical axes), at a particular point in space, along with its *x* and *y* components.

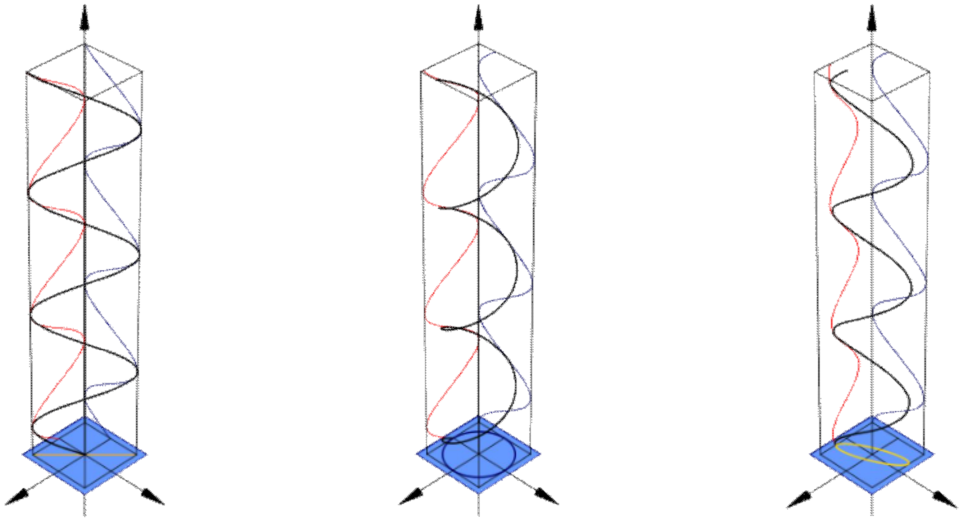

Linear (a) *Circular* (b) *Elliptical* (c)

Figure 2.9 Different polarization states, figure taken from *Wikipedia.*

In Figure 2.9(a), the electric field's *x* and *y* components are exactly in phase. The net result is polarization along a particular direction in the *x*-*y* plane over each cycle. Since the vector traces out a single line in the plane, this special case is called *linear polarization*. In Figure 2.9(b), the *x* and *y* components maintain the same amplitude but now are exactly 90° out of phase. In this special case, the electric field vector traces out a circle in the plane, and is thus referred to as *circular polarization*. Depending on whether the phase difference is + or −90°, it may be qualified as *right-hand circular polarization* or *left-hand circular polarization*.

The most general case occurs when the *x* and *y* components are out of phase by an arbitrary amount, or 90° out of phase but with different amplitudes, and is called *elliptical polarization*. In this case, the electric field vector traces out an ellipse (the *polarization ellipse*). This case is depicted in Figure 2.9(c). The ellipse shape may be produced either by a clockwise or counterclockwise rotation of the field, corresponding to distinct polarization states.

In summary, in the most general case, the optical field $\vec{E}$ is elliptically polarized, but there exist several combinations of amplitudes and phases which describe particular cases of polarization. These states of polarization are called *degenerate polarization states*: linearly horizontal/vertical polarized light (LHP/LVP), linear ±45° polarized light (L+45P/L-45P), and right/left circularly polarized light (RCP/LCP).

2.5.2 Polarization ellipse

According to Fresnel's theory [66], orthogonal components of a field $\vec{E}$ may be expressed by wave equations

$$\nabla^2 E_x(z,t) = \frac{1}{c^2}\frac{\partial^2 E_x(z,t)}{\partial t^2} \tag{2.38}$$

$$\nabla^2 E_y(z,t) = \frac{1}{c^2}\frac{\partial^2 E_y(z,t)}{\partial t^2} \tag{2.39}$$

Where $E_x(z,t)$ and $E_y(z,t)$ are the optical field components, which describe sinusoidal oscillations in the *x-z* and *y-z* planes, *c* is the velocity of propagation of the optical field in space, and *t* is time. The simplest solution of equations (2.38) and (2.39) is in terms of sinusoidal functions. For propagation in the +*z*-direction, the solutions may be represented as

$$E_x(z,t) = E_{0x}\cos(\omega t - kz + \delta_x) \tag{2.40}$$

$$E_y(z,t) = E_{0y}\cos(\omega t - kz + \delta_y) \tag{2.41}$$

Where E_{0x} *and* E_{0y} are the maximum amplitudes, $\omega t\text{-}kz$ is the propagator, and δ_x and δ_y are arbitrary phases of the components respectively. Equations (2.40) and (2.41) can be re-written in the following way

$$\frac{E_x(z,t)}{E_{0x}} = \cos(\omega t - kz)\cos\delta_x - \sin(\omega t - kz)\sin\delta_x \tag{2.42}$$

$$\frac{E_y(z,t)}{E_{0y}} = \cos(\omega t - kz)\cos\delta_y - \sin(\omega t - kz)\sin\delta_y \tag{2.43}$$

After some algebra, the following relations can be derived

$$\frac{E_x(z,t)}{E_{0x}}\sin\delta_y - \frac{E_y(z,t)}{E_{0y}}\sin\delta_x = \cos(\omega t - kz)\sin(\delta_y - \delta_x) \tag{2.44}$$

$$\frac{E_x(z,t)}{E_{0x}}\cos\delta_y - \frac{E_y(z,t)}{E_{0y}}\cos\delta_x = \cos(\omega t - kz)\sin(\delta_y - \delta_x) \tag{2.45}$$

By squaring equations (2.44) and (2.45) and adding them together, the following equation is obtained

$$\frac{E_x(z,t)^2}{E_{0x}{}^2} + \frac{E_y(z,t)^2}{E_{0y}{}^2} - \frac{2E_x(z,t)E_y(z,t)}{E_{0x}E_{0y}}\cos\delta = \sin^2\delta \tag{2.46}$$

where $\delta = \delta_x - \delta_y$ and δ_x and δ_y are arbitrary phases. Equation (2.46) is referred to as the *polarization ellipse*, which represents a locus of points described by the optical field as it propagates. A schematic diagram of the polarization ellipse is shown in Figure 2.10.

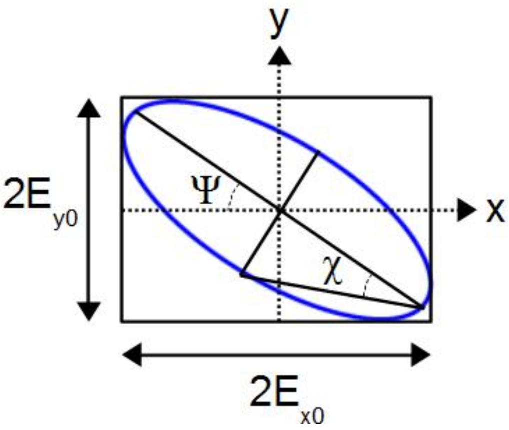

Figure 2.10 Polarization Ellipse.

The *polarization ellipse* of Figure 2.10 can be expressed in terms of angular parameters: the *orientation angle*, ψ, and the *ellipticity angle*, χ. These angles may be expressed in terms of the parameters of the *polarization ellipse* as follows

$$\tan 2\psi = \frac{2E_{0x}E_{0y}}{E_{0x}^2 - E_{0y}^2}\cos\delta\,, \quad 0 \le \psi \le \pi \tag{2.47}$$

$$\sin 2\chi = \frac{2E_{0x}E_{0y}}{E_{0x}^2 - E_{0y}^2}\sin\delta\,, \quad -\pi/4 \le \chi \le \pi/4 \tag{2.48}$$

2.5.3 Poincaré Sphere

In general, the *polarization ellipse* is a good way to visualize the polarization behaviour of a propagating polarized optical beam. However, during the propagation of polarized light, the orientation and ellipticity angles of the polarization ellipse change. The calculations required to determine the new orientation and ellipticity angles are time-consuming and tedious. An alternate representation, which would mitigate these drawbacks is called the *Poincaré Sphere* [66, 67, 68, 69], shown on Figure 2.11 below.

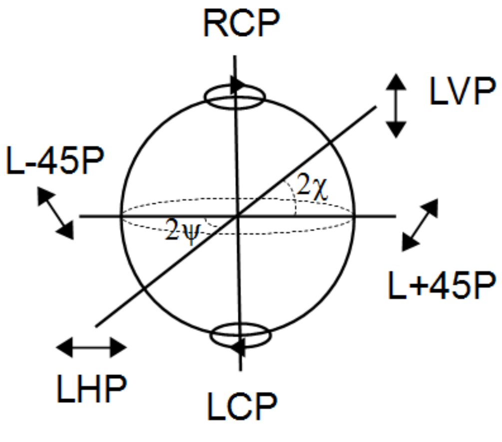

Figure 2.11 Poincaré Sphere.

Since any point of a sphere can be represented by the equation $x^2 + y^2 + z^2 = 1$, where x, y and z are the Cartesian coordinates of the axes of the sphere, it is therefore possible to express the Poincaré Sphere in terms of the orientation and ellipticity ψ and χ, as follows

$$x = \cos(2\chi)\cos(2\psi) \quad (2.49)$$

$$y = \cos(2\chi)\sin(2\psi) \quad (2.50)$$

$$z = \sin(2\chi) \quad (2.51)$$

Equation (2.49)-(2.51) relate the Cartesian coordinates *(x, y, z)* to the Poincaré Spherical coordinates *(1, ψ, χ)*.

Applying the time average definition to the polarization ellipse of equation (2.46) yields the following equation

$$\left(E_{0x}^2 + E_{0y}^2\right)^2 - \left(E_{0x}^2 - E_{0y}^2\right)^2 - \left(2E_{0x}E_{0y}\cos\delta\right)^2 = \left(2E_{0x}E_{0y}\sin\delta\right)^2 \quad (2.52)$$

Defining the terms of equation (2.52) in the following way

$$S_0 = E_{0x}^2 + E_{0y}^2 \quad (2.53)$$

$$S_1 = E_{0x}^2 - E_{0y}^2 \quad (2.54)$$

$$S_2 = 2E_{0x}E_{0y}\cos\delta \quad (2.55)$$

$$S_3 = 2E_{0x}E_{0y}\sin\delta \quad (2.56)$$

We obtain the following relation

$$S_0^2 = S_1^2 + S_2^2 + S_3^2 \quad (2.57)$$

Where S_0, S_1, S_2 and S_3 are the observables of the polarized field, and are called the *Stokes polarization parameters*. The S_0 parameter describes the total intensity of the optical beam, which is usually normalized to 1. The S_1 parameter describes the domination of LHP light over LVP, the S_2 parameter describes the domination of L+45P light over L-45P light, while the S_3 parameter describes the domination of RCP light over LCP.

The normalized *Stokes vector* may be expressed as $\boldsymbol{S}=(S_1, S_2, S_3)$, and may be used to express degenerate polarization states as follows: $\boldsymbol{S}_{LHP}=(1,0,0)$, $\boldsymbol{S}_{LVP}=(-1,0,0)$, $S_{L+45P}=(0,1,0)$, $\boldsymbol{S}_{L-45P}=(0,-1,0)$, $\boldsymbol{S}_{RCP}=(0,0,1)$, and $\boldsymbol{S}_{LCP}=(0,0,-1)$. An elliptically polarized light will have a Stokes vector whereby S_1, S_2, $S_3 \neq 0$, while a first order approximation to unpolarized light will have a Stokes vector $\boldsymbol{S}=(0,0,0)$.

2.5.4 Birefringence

Birefringence is an optical property of a material having a refractive index which depends on the polarization and propagation direction of light [1, 61]. The birefringence is often quantified as the maximum difference between refractive indices exhibited by the material. In optical fibers, birefringence results from the difference in indices of refraction between the two principal *x*- and *y*- axes, also referred to as the fast and slow axes, since light will propagate with different speeds along two axes having different indices of refraction. *Intrinsic birefringence* results from asymmetry of the fiber core, usually caused by imperfections of the fiber drawing process. *Induced birefringence* results from induced stress on the fiber, such as bending or twisting. For all practical purposes, the fiber manufactured would possess a various degree of birefringence either due to imperfections in the fiber drawing process, or in the later cabling and installation processes, as well as environmental perturbations. The different kinds of birefringence include *linear birefringence*, which causes the orthogonally polarized modes to have linear polarizations (LP). *Circular birefringence* produces left- and right-circularly polarized (CP) modes, while *elliptical birefringence* causes elliptical polarization of the orthogonally polarized modes. The difference in refractive indices of the principle axes causes the light to travel along orthogonally polarized modes at different phase velocities, yielding a phase difference between the two waves. The two waves will arrive at the end of the fiber at different times, causing the output spectrum of light to spread out, resulting in polarization mode dispersion (PMD). The length of the fiber required to bring the two polarization modes back in phase and reproduce the original polarization state is the *beat length*, L_B, defined as $L_B = \lambda/\Delta n$, where λ is the wavelength of light, and n is the refractive index.

2.6 Summary

In conclusion, nonlinear optics studies the interaction between moderate and intense optical fields. When light travels through matter, various scatterings, which are caused by fluctuations of the optical properties of the medium can occur. The spontaneous Brillouin scattering arises from the interaction between a light wave and an acoustic wave. The acoustic wave can be considered as a propagating grating that diffracts the incident wave and induces the periodic variation of the material density, and consequently, the refractive index change. The diffracted wave experiences a frequency shift with an amount proportional to the acoustic velocity inside the material due to the Doppler Effect. Stimulated Brillouin scattering arises from the *electrostriction* caused by the incident optical fields. When two counter-propagating light waves are present inside the fiber, the beating of these two waves can induce the density and refractive index variation caused by *electrostriction*. The acoustic wave inside the fiber is enhanced when the beat frequency of the two lightwaves matches with the frequency of the acoustic wave. The scattered Stokes wave is then increased by the enhanced acoustic wave. The positive feedback between the acoustic wave and the scattered Stokes wave leads to Stimulated Brillouin scattering. This mechanism can also include both the Stokes and anti-Stokes waves, to yield combined Brillouin gain and loss in an optical fiber. In this regime, there are two scattered waves, the SW and the ASW, and two counter-propagating acoustic gratings inside the optical fiber.

Since SBS originates from the mixing of the two light waves, the efficiency of this effect is polarization dependent. Polarization states arise from the oscillation of the electric field with different orientations in a *polarization ellipse*. A *Poincaré sphere* is used to derive *Stokes vectors*, which are used to define polarization states. *Birefringence* is an optical property of a material having a refractive index which depends on the polarization and propagation direction of light, and is defined as the maximum difference between the refractive indices exhibited by the material. In optical fibers, this is the difference between the indices of refraction of the *x*- and *y*- principal states of polarization.

Chapter 3

3D parametric model

3.1. Introduction

As described in section 1.2, previously obtained solutions for SBS are numerical with analytical portions, and, therefore, qualify as hybrid solutions. Though the analytical portions provide useful information about intensity distributions along the fiber, they fall short in describing spectral characteristics of the Brillouin amplification conveyed by the transcendental equation. The lack of analytical expressions for Brillouin spectra substantially limits the utility of the hybrid solution [8] for applications, since spectral measurement is a leading technique for strain and temperature sensing. Methods of avoiding systematic errors in distributed fiber sensing are described in [3, 70, 71, 72], but do not include the correct conditions under which an undesirable effect of spectral distortion occurs in optical fibers, nor how to more accurately obtain a Lorentzian profile for sensing applications.

We propose a *3D parametric model* of Brillouin amplification that will reflect the effects of input pump and pulse powers on the level of pump wave depletion in the lossless fiber, and act as a classification tool to describe the level of similarity between various Brillouin amplification processes in optical fibers. This model is valid in *any* power regime capable of sustaining SBS, corresponding to $0<P_{pump}<10$mW and $0<P_{Stokes}<40$mW, and for an arbitrary depletion of the PW and pulses, acting as an effective, universal, tool for avoiding the undesirable spectral distortion via limitations of the parameter space that is relevant to distributed Brillouin fibers.

Additionally, the *3D parametric model* has been used to find fully analytic solutions for calculating the distribution of a pump wave (PW), which has been taken to be a continuous wave, and a Stokes wave (SW) intensities and phases, for an arbitrary pump depletion (0-100%), and an arbitrary range of pump and pulse intensities, in fiber lengths of up to a few kilometers. These solutions are valid for expressing the Brillouin spectrum under different depletion conditions, including the spectral distortion effect that occurs for high levels of pump depletion and high Stokes powers, which has been confirmed experimentally.

3.2 Model

The process of stimulated Brillouin scattering has been studied in a lossless single mode optical fiber, with core radius of 4.1μm. Attenuation terms have been neglected due to the short fiber lengths inherent in the model. The schematic arrangement and typical intensity distributions are shown on Figures 2.6 and 2.7 in Chapter 2.

In the slowly varying amplitude approximation, recall that the steady state interaction between the PW, the SW and an acoustic wave (AW_1) is described by the following system of equations [9]. The system operates in the steady-state regime when pulse lengths greater than 10ns.

$$-\frac{\partial A_1}{\partial z} = \frac{i\omega_1\gamma_e}{2nc\rho_0}\rho_1 A_2 \tag{3.1}$$

$$\frac{\partial A_2}{\partial z} = \frac{i\omega_2\gamma_e}{2nc\rho_0}\rho_1^* A_1 \tag{3.2}$$

$$\left(\Omega_B^2 - \Omega_1^2 - i\Omega_1\Gamma_B\right)\rho_1 = \frac{\gamma_e q_1^2}{4\pi} A_1 A_2^* \tag{3.3}$$

Where:
$\Omega_1 = \omega_1 - \omega_2$
A_1 – complex amplitude of the PW
A_2 – complex amplitude of the SW
ρ_1 – complex amplitude of the AW_1 caused by interaction of PW + SW
ω_1 – angular frequency of the PW
ω_2 – angular frequency of the SW
γ_e – electrostrictive constant
z – coordinate along the fiber
$\mathbf{q}_1$ – acoustic wavevector: $\mathbf{q}_1 \approx 2\mathbf{k}_1$

Ω_1 – angular frequency of the AW_1 caused by interaction of PW + SW
Ω_B – Brillouin frequency: $\Omega_B = 2n \cdot \frac{v}{c} \cdot \omega_1$
c – speed of light
ρ_0 – density of the fiber
Γ_B – Brillouin linewidth
v – speed of sound in the fiber
n – index of refraction of the fiber
$\mathbf{k}_1$ – wavevector of the PW: $|\mathbf{k}_1| = n\omega_1/c$

Recall that in the above arrangement, the SW input parameters are known only at the beginning of the fiber, i.e. at $z=0$. Correspondingly, the PW input parameters are known only at the end of the fiber, i.e. at $z=L$, where L is the length of the fiber. Therefore, the boundary conditions for system of equations (3.1)-(3.3) are as follows

$$|A_1(L)|^2 = A^2_{10}; \qquad |A_2(0)|^2 = A^2_{20} \tag{3.4}$$

where A^2_{10} and A^2_{20} are known squared absolute values of the complex amplitudes A_1 and A_2, respectively.

The goal is to find analytical expressions for the intensities and phases of the PW and SW. Introducing the intensities of the waves as $I_i = \frac{nc}{2\pi}|A_i|^2$, where I_i is the intensity of the *i-th* wave, the system of equations (3.1)-(3.3) is transformed into the following system of equations (3.5)-(3.7).

$$\frac{dI_1}{dz} = \frac{2\gamma_e^2 k^3}{n^3 c\rho_0 \Omega_1 \Gamma_B} \cdot \frac{1}{1+\xi_1^2} I_1 I_2 \tag{3.5}$$

$$\frac{dI_2}{dz} = \frac{2\gamma_e^2 k^3}{n^3 c\rho_0 \Omega_1 \Gamma_B} \cdot \frac{1}{1+\xi_1^2} I_1 I_2 \tag{3.6}$$

$$|\rho_1|^2 = \left(\frac{2\gamma_e k^2}{nc\rho_0 \Omega_1 \Gamma_B} \right)^2 \cdot \frac{1}{1+\xi_1^2} I_1 I_2 \tag{3.7}$$

$$\xi_1 = \frac{\Omega_B^2 - \Omega_1^2}{\Omega_1 \Gamma_B} \tag{3.8}$$

Equations (3.5)-(3.7) are similar to those derived in [8]. Correspondingly, the boundary conditions (3.4) become as follows, where I_{10} and I_{20} are the input intensities of the PW and SW respectively

$$|I_1|^2_{z=L} = I_{10}; \qquad |I_2|^2_{z=0} = I_{20} \tag{3.9}$$

Let us also further introduce the dimensionless variables l, Y_1, Y_2 and $Y_{acoustic}$ by the following relations

$$l = \frac{z}{L}; \quad Y_1 = \frac{P_1}{P_{10}}; \quad Y_2 = \frac{P_2}{P_{20}}; \quad Y_{acoustic} = \left|\frac{\rho_1}{\rho_0}\right|^2 \tag{3.10}$$

where L is the length of the fiber, P_{10} is the input power of the PW, P_1 is the power of the PW inside the fiber, P_{20} is the input power of the SW and P_2 is the power of the SW inside the fiber, where the following relation was used: $P=I\cdot\pi r^2$, where r is the radius of the fiber. For the convenience of notation, let us introduce dimensionless coefficients β_1, β_3 and β_5 which determine the rate of energy transfer for the PW, SW and AW_1 correspondingly:

$$\beta_1 = \frac{2\gamma_e^2 k^3 L P_{20}}{\pi r^2 n^3 c \rho_0 \Omega_1 \Gamma_B} \cdot \frac{1}{1+\xi_1^2} \tag{3.11}$$

$$\beta_3 = \frac{2\gamma_e^2 k^3 L P_{10}}{\pi r^2 n^3 c \rho_0 \Omega_1 \Gamma_B} \cdot \frac{1}{1+\xi_1^2} \tag{3.12}$$

$$\beta_5 = \left(\frac{2\gamma_e k^2}{\pi r^2 n c \rho_0 \Omega_1 \Gamma_B}\right)^2 \cdot \frac{1}{1+\xi_1^2} \cdot P_{10} P_{20} \tag{3.13}$$

In the dimensionless notation, the system of equations (3.5)-(3.7) becomes

$$\frac{dY_1}{dl} = \beta_1 Y_1 Y_2 \tag{3.14}$$

$$\frac{dY_2}{dl} = \beta_3 Y_1 Y_2 \tag{3.15}$$

$$Y_{acoustic} = \beta_5 Y_1 Y_2 \tag{3.16}$$

Correspondingly, the boundary conditions

$$Y_1(1)=1; \qquad Y_2(0)=1 \tag{3.17}$$

3.3 Solution

The following analysis will be performed on the system of equations (3.14)-(3.16) to determine the dimensionless intensities Y_1 and Y_2 of the interacting optical waves, in a similar way to the one performed in [8].

Since $\beta_3 \neq 0$, we can find the product of Y_1 and Y_2 from equation (3.15), and substitute the product into equation (3.14), determining thereby the first integral of the system

$$Y_1 - \frac{\beta_1}{\beta_3} Y_2 = C_1 \tag{3.18}$$

Determining the arbitrary constant C_1 from the boundary conditions (3.17) at $\ell = 0$, we yield

$$C_1 = Y_1(0) - \frac{\beta_1}{\beta_3} \tag{3.19}$$

where $Y_1(0)$ is the output intensity of the PW. Finding Y_2 from the first integral (3.18) and substituting it into equation (3.14), we yield the following differential equation for Y_1

$$\frac{dY_1}{dl} = \beta_3 Y_1 (Y_1 - C_1) \tag{3.20}$$

Since $Y_2(\ell)$ is a monotonically increasing function of its argument, starting from $Y_2(0)=1$, and assuming that the PW is never depleted completely, we conclude that $Y_1 \neq 0$ and $Y_2 \neq 0$ for any $\ell \in [0, 1]$. Therefore, it follows from (3.18) that $Y_1 - C_1 \neq 0$. This allows for separation of variables in (3.20), resulting in the following second integral of the system of equations (3.14)-(3.16).

$$\int \frac{dY_1}{Y_1\cdot(Y_1-C_1)} = \int \beta_3\cdot dl + C_3 \tag{3.21}$$

Determining the arbitrary constant C_3 from the boundary conditions (3.17) and introducing a dummy variable τ, we yield

$$\int_{Y_1(l)}^{1} \frac{d\tau}{\tau\cdot(\tau-C_1)} = \beta_3(1-l) \tag{3.22}$$

Expression (3.22) contains the yet unknown output intensity $Y_1(0)$ of the PW as a part of the arbitrary constant C_1. At $\ell=0$, the expression (3.22) turns into a nonlinear equation for determining $Y_1(0)$

$$\int_{Y_1(0)}^{1} \frac{d\tau}{\tau\cdot\left[\tau-Y_1(0)+\frac{\beta_1}{\beta_3}\right]} = \beta_3 \tag{3.23}$$

Once $Y_1(0)$ is determined from (3.23) and $Y_1(\ell)$ is determined from (3.22), $Y_2(\ell)$ can be found from the first integral (3.18) as follows

$$Y_2(l) = \frac{\beta_3}{\beta_1}\left[Y_1(l)-Y_1(0)\right]+1 \tag{3.24}$$

Here we will only consider the case when $C_1\neq 0$. The integrand can be expanded into a sum of simple fractions, each fraction being continuous on the interval of integration $[Y_1(\ell), 1]$.

$$\frac{1}{\tau\cdot(\tau-C_1)} = \frac{1}{C_1}\cdot\left(\frac{1}{\tau-C_1}-\frac{1}{\tau}\right) \quad ; \quad C_1\neq 0 \tag{3.25}$$

Integration and further simplification yield

$$Y_1(l)=\frac{Y_1(0)-\frac{\beta_1}{\beta_3}}{1-\frac{\beta_1}{\beta_3}\cdot\frac{1}{Y_1(0)}\cdot \mathrm{e}^{\left(Y_1(0)-\frac{\beta_1}{\beta_3}\right)\cdot\beta_3\cdot l}};\quad Y_1(0)\neq\beta_1/\beta_3 \tag{3.26}$$

Correspondingly, from (3.24) it follows that

$$Y_2(l)=1+G_{SW}\,;\qquad Y_1(0)\neq\beta_1/\beta_3 \tag{3.27}$$

Where

$$G_{SW}=\frac{\mathrm{e}^{\left(Y_1(0)-\frac{\beta_1}{\beta_3}\right)\cdot\beta_3\cdot l}-1}{1-\frac{\beta_1}{\beta_3}\cdot\frac{1}{Y_1(0)}\cdot \mathrm{e}^{\left(Y_1(0)-\frac{\beta_1}{\beta_3}\right)\cdot\beta_3\cdot l}} \tag{3.28}$$

is the gain the SW experiences. Expression (3.27), re-written in terms of dimensional intensities $I_1(z)$ and $I_2(z)$, coincides with the expression for the intensity of the Stokes wave in [8].

The solution of the system of equations (3.14)-(3.16) for the intensities (3.26) and (3.27) is not complete until an expression for the output intensity $Y_1(0)$ of the PW is determined, which corresponds to the root of the transcendental equation [8], shown in expression (3.29). As such, previously known solutions, being formally analytical, require the numerical solution of expression (3.29). Therefore, for all practical purposes, previously obtained solutions are better qualified as hybrid solutions (i.e. partly numerical or graphical and partly analytical).

$$\frac{1}{Y_1(0)-\frac{\beta_1}{\beta_3}}\cdot\ln\left\{\frac{\beta_3}{\beta_1}\cdot Y_1(0)\cdot\left[1+\frac{\beta_1}{\beta_3}-Y_1(0)\right]\right\}-\beta_3=0;\qquad Y_1(0)\neq\beta_1/\beta_3 \tag{3.29}$$

Unfortunately, the simplified equation (3.29) has many undesirable mathematical properties, which make the equation ill-suited even for numerical, let alone analytical, solution. Indeed, the left part of the equation is not a continuous function, the equation has more than one root, and for $\beta_1/\beta_3<1$ the removable singularity of $Y_1(0)=\beta_1/\beta_3$ falls within the interval of physical significance of $Y_1(0)\in(0, 1]$.

The analytical solution of $Y_1(0)$ lies in transforming equation (3.29) into a form suitable for analytical approximation. This form is shown below as expression (3.30).

$$1-Y_1(0)-\beta_1\cdot\frac{e^{\beta_3\cdot Y_1(0)-\beta_1}-1}{\beta_3\cdot Y_1(0)-\beta_1}=0 \tag{3.30}$$

The transcendental equation of (3.30) has a single root "$Y_1(0)$" that depends only on two dimensionless parameters β_1 and β_3, i.e. $Y_1(0)=x(\beta_1,\beta_3)$. Additionally, this root falls within the range $[0,1]$ which represents the range of possible dimensionless output intensities of the PW, giving it a physical significance.

Using equation (3.27), we get the following expression for the output intensity of the SW, assuming $Y_1(0)$ is known.

$$Y_2(1)=1+\frac{\beta_3}{\beta_1}\left[1-Y_1(0)\right] \tag{3.31}$$

3.4 Analytic Solutions

Fully analytic expressions (3.26) and (3.27) can only be complete when an analytic expression for $Y_1(0)$ is found. Since we are looking for a solution placing no limits on $Y_1(0)$, let us expand the left-hand side (LHS) of the equation (3.30) into a MacLauren series with respect to the variable β_3. If we define, for convenience, $x=Y_1(0)$, and

$$F(\beta_1,\beta_3,x)=1-x-\beta_1\cdot\frac{e^{\beta_3\cdot x-\beta_1}-1}{\beta_3\cdot x-\beta_1}$$

Then $F(\beta_1,0,x)=e^{-\beta_1}-x$, and $\frac{1}{n!}\cdot\frac{\partial^n F(\beta_1,0,x)}{\partial\beta_3{}^n}=-e^{-\beta_1}\cdot C_n\cdot x^n$ where

$$C_n=\frac{e^{\beta_1}-\left(1+\beta_1+\ldots+\frac{1}{n!}\beta_1{}^n\right)}{\beta_1{}^n}$$

The corresponding MacLauren series is

$$F(\beta_1,\beta_3,x)=e^{\beta_1}-x-e^{-\beta_1}\sum_{n=1}^{\infty}C_n\cdot x^n\cdot\beta_3{}^n$$

Thus, the equation (3.30) takes a form suitable for finding approximate analytical solutions.

$$e^{\beta_1}-x-e^{-\beta_1}\sum_{n=1}^{\infty}C_n\cdot x^n\cdot\beta_3{}^n=0 \qquad (3.32)$$

3.4.1 Linear approximation

Keeping only linear terms in (3.32) we yield the simplest approximation as follows

$$e^{\beta_1}-x-\beta_3\cdot e^{-\beta_1}\frac{e^{\beta_1}-(1+\beta_1)}{\beta_1}\cdot x\approx 0$$

Collecting like terms and solving for “*x*” yields

$$x=\frac{\beta_1}{(\beta_1+\beta_3)\cdot e^{\beta_1}-\beta_3\cdot(1+\beta_1)} \qquad (3.33)$$

If better accuracy is required, the quadratic approximation is in order.

3.4.2 Quadratic approximation

Keeping additionally $\beta_3{}^2$ terms in (3.32), we yield the next approximation as follows

$$e^{-\beta_1} - x - \beta_3 \cdot e^{-\beta_1} \frac{e^{\beta_1} - (1+\beta_1)}{\beta_1} \cdot x - \beta_3{}^2 \cdot e^{-\beta_1} \cdot \frac{e^{\beta_1} - \left(1+\beta_1+\frac{1}{2}\beta_1{}^2\right)}{\beta_1{}^2} \cdot x^2 \approx 0$$

After some simple but tedious algebra, we obtain a more accurate expression for the output intensity of the PW.

$$x = x_{linear} \cdot \frac{1}{\frac{1}{2} + \sqrt{\frac{1}{4} + x_{linear}^2 \cdot \beta_3{}^2 \cdot \frac{e^{\beta_1} - 1 - \beta_1 - \frac{1}{2}\beta_1{}^2}{\beta_1{}^2}}} \qquad (3.34)$$

where x_{linear} is the output intensity of the PW in the linear approximation, defined by (3.33). In a similar way, one can also get the cubic and quartic approximations, which we do not show here due to their complexity.

3.5 Relative error

To gauge the accuracy of our analytical solutions (3.33) and (3.34), we compare them to the numerically calculated solution for the output dimensionless PW intensity. The transcendental equation (3.30) lends itself to numerical solution with the use of standard methods of computational physics.

3.5.1 Linear Approximation

The relative error is less than 33% in the worst case, on the interval $0<\beta_1<25.4$, $0<\beta_3<6.4$, in this case, corresponding to $0<P_{pump}<10$mW , $0<P_{Stokes}<40$mW, as it is shown on Figure 3.1 below.

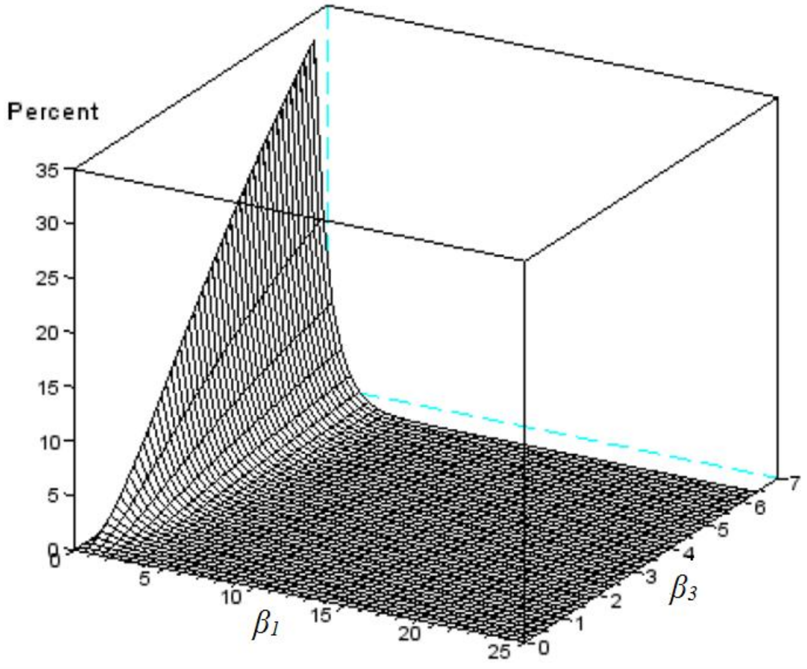

Figure 3.1 Relative error of $Y_1(0)$: Linear Approximation of *3D parametric model* of output PW. L=1000m, $0<P_{pump}<10$mW , $0<P_{Stokes}<40$mW

3.5.2 Quadratic Approximation

The relative error of the quadratic approximation is shown on Figure 3.2 below.

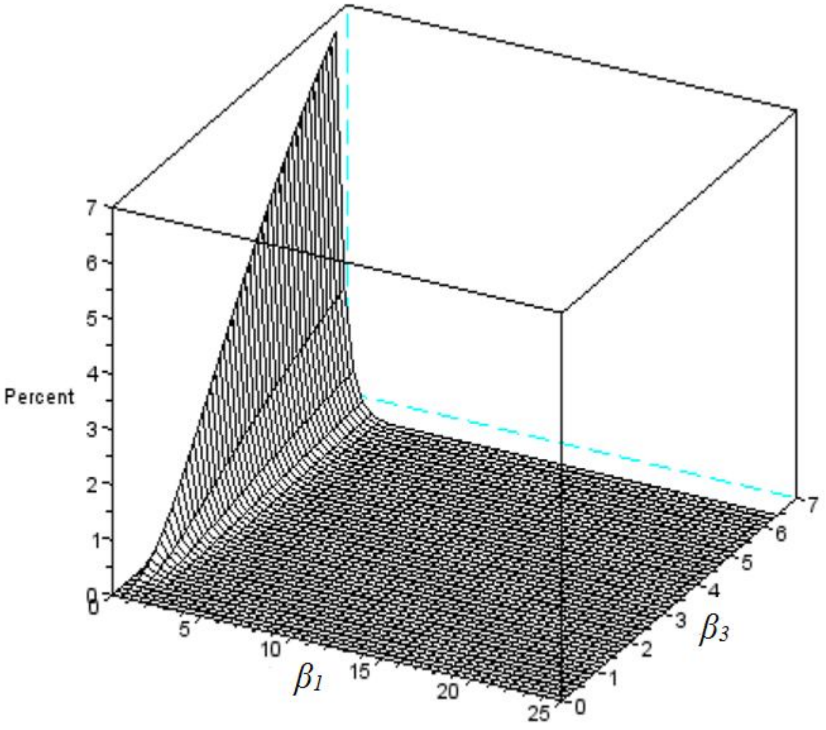

Figure 3.2 Relative error of $Y_1(0)$: Quadratic Approximation of *3D parametric model* of output PW. L=1000m, $0<P_{pump}<10$mW , $0<P_{Stokes}<40$mW

The relative error of the quadratic approximation is 6.5% in the worst case, which is more than three times smaller than the relative error given by the linear approximation.

Notice, however, that except for a limited combination of parameters for which there is an increase in relative error, deemed to be the "worst case", the relative error in most of the calculations shown in Figures 3.1 and 3.2 is 0%. This confirms the utility of the analytic approximations.

3.6 *3D parametric model*

An analytic *3D parametric model,* attained by plotting the linear approximation solution as a function of dimensionless parameters β_1 and β_3 is shown in Figure 3.3 below.

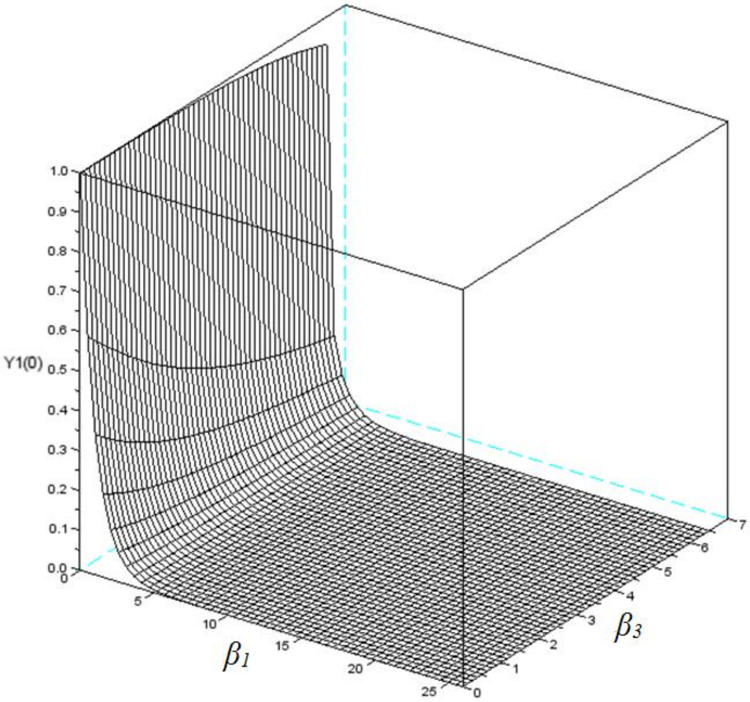

Figure 3.3 Linear Approximation of $Y_1(0)$: *3D parametric model* of output PW. Dimensionless output intensity of the PW versus dimensionless parameters β_1 and β_3.
γ_e=0.902, v=5616 m/s, n=1.48, λ=1.319μm, ρ_0=2.21 g/cm^3, Γ_B = 0.1 GHz
L=1000m, $0<P_{pump}<10$mW , $0<P_{Stokes}<40$mW

As can be seen from Figure 3.3, the linear approximation (3.34) covers the entire range of values of output intensities of the PW (i.e. from weak depletion, to full depletion when $Y_1(0)$~0). In spite of its simplicity, this *3D parametric model* is valid in a wide range of combinations of dimensionless parameters β_1 and β_3.

Using equation (3.31), a similar *3D parametric model* for the output Stokes intensity is calculated and shown below in Figure 3.4.

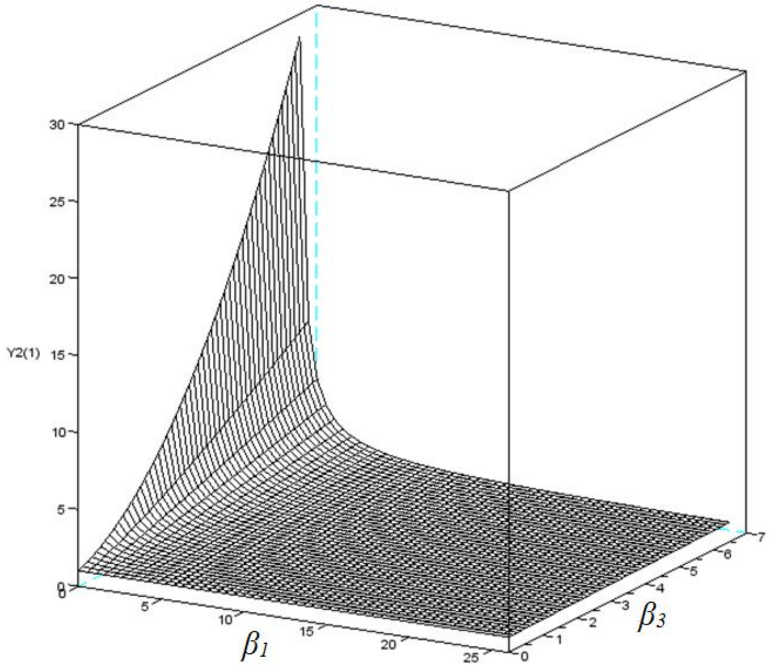

Figure 3.4 Linear Approximation of $Y_2(\ell)$: *3D parametric model* of output SW.
Dimensionless output intensity of the SW versus dimensionless parameters β_1 and β_3.
γ_e=0.902, v=5616 m/s, n=1.48, λ=1.319µm, ρ_0=2.21 g/cm^3, Γ_B = 0.1 GHz
L=1000m, $0<P_{pump}<10$mW , $0<P_{Stokes}<40$mW

As expected, while the PW experiences depletion, the SW experiences amplification.

3.7 *3D parametric model*: Similar and Dis-similar Processes

The *3D parametric model* for the output PW intensity allows for the easy interpretation of the effects of pump and pulse powers on the level of PW depletion in the fiber. Parameters of the fiber are described in Figures 3.3 and 3.4, and the range of pump and Stokes powers $0<P_{pump}<10$mW, $0<P_{Stokes}<40$mW, correspond to the following range of dimensionless parameters β_1 and β_3: $0<\beta_1<6.4$; $0<\beta_3<25.4$. This power range models PW depletion from 0-100%, corresponding to $0<Y_1(0)<1$ from Figure 3.1. For example, restricting the range of SW power to 1.6 mW$<P_{Stokes}<$40 mW yields a depletion of 55-100%. Further changes in SW power change the level of depletion accordingly. Being a very versatile model, a change in Stokes power, parameters of the fiber, or fiber length would alter the restrictions on β_1 and β_3, therefore allowing for the “picking and choosing” of the preferred level of depletion for the given fiber. For example, in optical fibers it is often preferable to avoid large depletion, which would require a Stokes power of <1.6mW for the parameters given in Figures 3.3 and 3.4.

The study of analytical solutions for the output PW intensity $Y_1(0)$ have led us to notice that certain patterns of similarity exist between various amplification processes in each regime, even though each process may be described by different combinations of parameters of amplification. On this basis, a system of classification of the Brillouin amplification processes has been developed and is described below for the PW and SW arrangement.
Below, we will provide several definitions which characterize the *3D parametric model*.

Statement 1.
Any Brillouin amplification process in a lossless media can be characterized by two dimensionless parameters, β_1 and β_3, determining the outcome of energy exchange between the PW and the SW.

Statement 2.
All possible outcomes of energy exchange between the PW and the SW are described by the relation $Y_1(0)=F(\beta_1,\beta_3)$ and can be graphically depicted as a *3D parametric model*, each point on the surface corresponding to a subset of Brillouin amplification processes, determined by the values of the dimensionless parameters β_1 and β_3.

Definition 1.
A point on the *3D parametric model* of *Statement 2*, corresponding to a subset of Brillouin amplification processes, determined by the values of the dimensionless parameters β_1 and β_3, is called the *representative point*.

Definition 2.
Two Brillouin amplification processes are called *similar* if they are characterized by the same representative point.

Definition 3.

Two Brillouin amplification processes are called *dis-similar*, if they are characterized by different representative points.

Definition 3.

The *degree of similarity* between two Brillouin amplification processes A and B is determined by the distance between their representative points, a bigger distance indicating a smaller degree of similarity, and vice versa.

Figure 3.5 below shows an example of two similar, and two dis-similar processes. Processes A and B are represented by points A and B, while Process C is represented by point C.

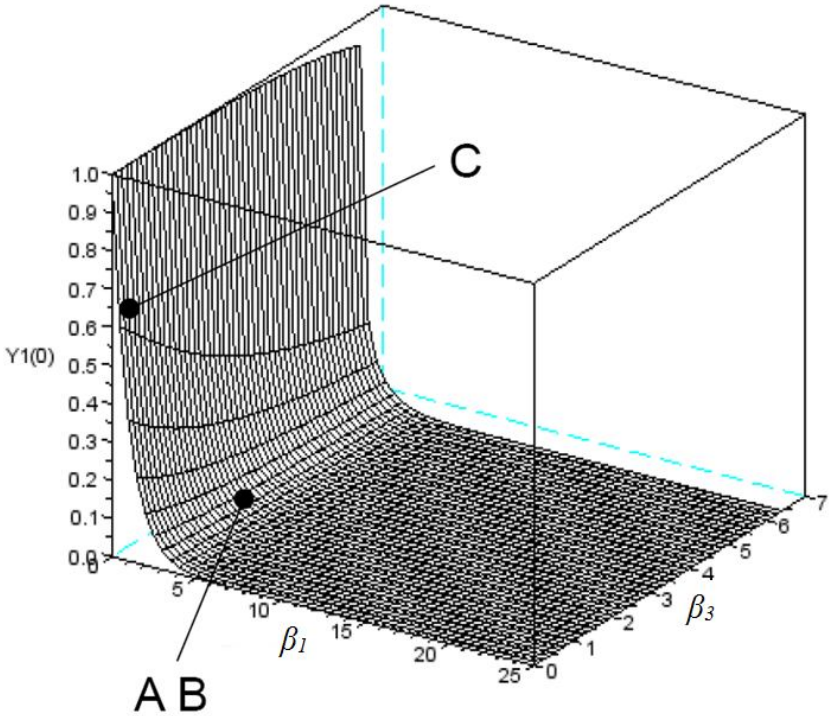

Figure 3.5 Linear Approximation of $Y_1(0)$: *3D parametric model* of output PW.
Dimensionless output intensity of the PW versus dimensionless parameters β_1 and β_3.
γ_e=0.902, v=5616 m/s, n=1.48, λ=1.319μm, ρ_0=2.21 g/cm^3, Γ_B = 0.1 GHz
L=1000m, $0<P_{pump}<10$mW , $0<P_{Stokes}<40$mW

Example 1.

Similar Processes: $(\beta_1)_A=3.18$, $(\beta_3)_A=1.59$, $(\beta_1)_B=3.18$, $(\beta_3)_B=1.59$

Process A: $\gamma_e=0.902$, $\omega_1=8.381097\cdot10^5$ GHz, $\omega_2=8.380692\cdot10^5$ GHz, $\Omega_1=4.053668\cdot10^1$ GHz, $\Omega_B=4.053668\cdot10^1$ GHz, $P_{10}=6.3$ mW, $P_{20}=12.7$ mW, n=1.48, c= 299792.458 km/s, $v=5000$ m/s, $\rho_0=2.21$ g/cm^3, $\Gamma_B = 0.1$ GHz, $r=4.1$ µm, $L=350$ m.

Process B: $\gamma_e=0.8$, $\omega_1=8.381097\cdot10^5$ GHz, $\omega_2=8.380692\cdot10^5$ GHz, $\Omega_1=4.053668\cdot10^1$ GHz, $\Omega_B=4.053668\cdot10^1$ GHz, $P_{10}=3.2$ mW, $P_{20}=6.3$ mW, $n=1.15$, $c=299792.458$ km/s, $v=5000$ m/s, $\rho_0=1.74$ g/cm^3, $\Gamma_B = 0.1$ GHz, $r=4.1$ µm, $L=350$ m.

Dis-similar Processes: $(\beta_1)_A=3.18$, $(\beta_3)_A=1.59$, $(\beta_1)_B=4.07\cdot10^{-1}$, $(\beta_3)_B=6.79\cdot10^{-2}$

Process A: $\gamma_e=0.902$, $\omega_1=8.381097\cdot10^5$ GHz, $\omega_2=8.380692\cdot10^5$ GHz, $\Omega_1=4.053668\cdot10^1$ GHz, $\Omega_B=4.053668\cdot10^1$ GHz, $P_{10}=6.3$ mW, $P_{20}=12.7$ mW, $n=1.48$, $c=$ 299792.458 km/s, $v=5000$ m/s, $\rho_0=2.21$ g/cm^3, $\Gamma_B = 0.1$ GHz, $r=4.1$ µm, $L=350$ m.

Process C: $\gamma_e=0.7$, $\omega_1=8.381097\cdot10^5$ GHz, $\omega_2=8.380692\cdot10^5$ GHz, $\Omega_1=4.053668\cdot10^1$ GHz, $\Omega_B=4.053668\cdot10^1$ GHz, $P_{10}=4.2$ mW, $P_{20}=25.3$ mW, $n=1.53$, $c=$ 299792.458 km/s, $v=5000$ m/s, $\rho_0=2.21$ g/cm^3, $\Gamma_B = 0.8$ GHz, $r=4.1$ µm, $L=350$ m.

3.8 Applications in Fiber Sensing

Classification of the Brillouin amplification processes, in terms of their degree of similarity as described above, may have useful applications in the design of various devices based on Brillouin scattering, such as fiberoptic sensors. Indeed, a design specification for a device is likely to require that a certain level of output signal be achieved within a certain margin to ensure normal operation of the device. Practice shows that there often exist severe design and technological constraints for many such devices; therefore, though theoretical considerations may suggest a combination of parameters of the Brillouin amplification process which meets the design specification requirements, this theoretical combination may be impractical, expensive, or simply unavailable technologically. In this case, the *3D parametric model* would be useful in finding an alternate combination of parameters that is available technologically, and which either meets the requirements of the design specification or is reasonably close to it. Such a model would allow for the quick and inexpensive attainment of the maximum utility and performance from such a device.

3.9 Spectral Characteristics

3.9.1 Analytical expressions

The starting point in the analysis of analytical expressions for Brillouin output spectra are the previously derived expressions for the output intensities of the PW $x(\beta_1, \beta_3)$, expressed in equation (3.34), and the SW $\mu(\beta_1, \beta_3)$, expressed in equation (3.31). Denoting $x=Y_1(0)$ and $\mu=Y_2(1)$, the following standard approximations are made.

$$\frac{\Omega_{\mathrm{B}}}{\Omega_1} \approx 1; \quad \frac{\omega_1}{\omega_2} \approx 1; \quad \Omega_B+\Omega_1 \approx 2\Omega_B \tag{3.35}$$

With these approximations in mind, we yield instead of (3.34) much simpler expressions (3.36) and (3.37).

$$x(\xi_1) = \frac{b}{(1+b)\cdot e^{\beta_1(\xi_1)} - 1 - \beta_1(\xi_1)} \tag{3.36}$$

$$\mu(\xi_1) = 1 + \frac{1}{b} - \frac{1}{(1+b)\cdot e^{\beta_1(\xi_1)} - 1 - \beta_1(\xi_1)} \tag{3.37}$$

Where $b = \frac{P_{10}}{P_{20}}$, $\xi_1 \approx \frac{\Omega_B - \Omega_1}{\frac{1}{2}\Gamma_B}$.

And

$$\beta_1(\xi_1) = \frac{\beta_{10}}{1+\xi_1^2}; \beta_3(\xi_1) = \frac{\beta_{30}}{1+\xi_1^2}; \beta_{10} = \frac{2\gamma_e^{\mathbf{2}} k_{air}^2 \mathbf{P_{20}} L}{\pi r^2 c \rho_{\mathbf{0}} \Gamma_B \mathbf{\Omega_B}}; \beta_{30} = \frac{2\gamma_e^{\mathbf{2}} k_{air}^2 \mathbf{P_{10}} L}{\pi r^2 c \rho_{\mathbf{0}} \Gamma_B \mathbf{\Omega_B}} \tag{3.38}$$

$$x_0 = x(0) = \frac{b}{(1+b)\cdot e^{\beta_{10}} - 1 - \beta_{10}}$$

Analytical expressions for the full width at half maximum (*FWHM*) of the spectra may also be obtained, valid for 0-100% nonlinearity. For the simplicity of notation, we introduce $x_0=x(0)$, $\mu_0=\mu(0)$ and recall that $b=\beta_{10}/\beta_{30}$.

$$FWHM = 2\sqrt{\beta_{10}\frac{1+x_0}{1-x_0}\left(\frac{1}{2}+\frac{1}{2}\sqrt{1+2\frac{1+b}{b}\frac{1-x_0}{1+x_0}}\right)-1} \qquad \text{(units of } \Gamma_B\text{)} \quad (3.39)$$

Using the expressions (3.26) and (3.27), we are able to describe the behaviour of the PW and SW at every coordinate inside the fiber, and the corresponding output intensity spectrums obtained from expressions (3.36) and (3.37) above.

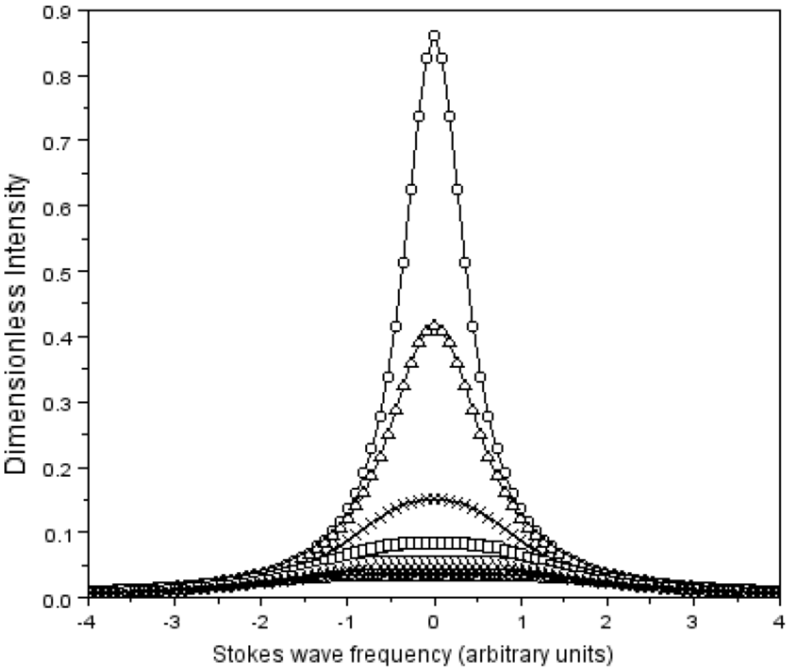

Figure 3.6 Analytical results, normalized intensity units of the SW.

P_{SW} (mW) = ○ 0.01; △ 1.8; × 6.6; □ 12.1; ▽ 17.1; + 22.4; ✱ 27.2; --- 31.8; ▬ 36.3

n=1.48, γ_e=0.902, λ=1319nm, ρ_0=2.21 g/cm^3, v=5616 m/s, L=1000 m, Γ_B=0.1 GHz, P_{PW} = 1.0 mW.

Looking at the Stokes wave spectrum in Figure 3.6, we can see that spectral distortion occurs with increasing Stokes wave power. Energy is transferred from the Pump (higher frequency) to the SW (lower frequency). A strong SW signal can induce pump depletion [73], since it causes the pump to transfer more energy. However, since $P_{PW}<P_{SW}$, saturation effects occur because there is not enough energy supplied by the Pump.

To better demonstrate the correlation between pump depletion and SW spectrum distortion, the $Ratio=FWHM/G_{SW}$ is plotted versus pump depletion in Figure 3.7 for various Stokes powers, where *FWHM* is the full width at half maximum of the Stokes spectrum from expression (3.39), and G_{SW} is the gain of the SW from expression (3.28). The more distorted the Stokes spectrum, the higher its *Ratio* value will be. Depletion of the pump was calculated using expression (3.26).

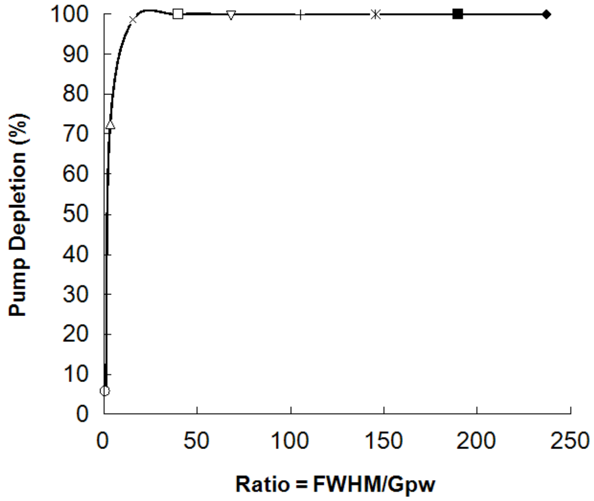

Figure 3.7 Pump depletion as a function of Stokes spectral distortion.

P_{SW} (mW) = ○ 0.01; △ 1.8; × 6.6; □ 12.1; ▽ 17.1; + 22.4; ✱ 27.2; ■ 31.8; ♦ 36.3

n=1.48, γ_e=0.902, λ=1319nm, ρ_0=2.21 g/cm^3, v=5616 m/s, L=1000 m, Γ_B=0.1 GHz, P_{PW} = 1.0 mW.

As can be seen from Figure 3.7, the stronger the Stokes power, the greater the pump depletion. Consequently, the spectral distortion of the SW spectrum is higher (higher *Ratio*). The Lorentzian shape of the spectrum then becomes flattened and the *FWHM* increases, as saturation effects begin to become prominent. As such, an output Lorentzian Stokes wave spectrum (low *Ratio*) is an *indication* of low pump depletion, while an increase in spectral distortion (high *Ratio*) is symptomatic of an increase in pump depletion and saturation effects.

Pump depletion is detrimental in the field of fiberoptic sensing devices, since it causes a deviation of the peak frequency of the recorded spectrum from the local Brillouin frequency shift, resulting in a systematic error in temperature/strain evaluation [73]. Hence, a Lorentzian SW spectral shape is desired to ensure minimal pump depletion. It is possible to use the *3D parametric model* to avoid parameter combinations which would lead to such a spectral distortion effect and, instead, choose parameter combinations which would yield an approximate Lorentzian profile. This will be described in more detail in section 3.9.2.

3.9.2 Transition to a Lorentzian Spectra (Curvature)

As can be seen from Section 3.9.1, in the nonlinear case, the general expression for the Stokes wave spectrum (3.37) does not represent a Lorentzian profile. However, it can be seen from Figure 3.6, as well as experimental results (Figure 3.10 below), that for certain combinations of parameters, the output SW spectrum is very close, if not indistinguishable, from the Lorentzian spectrum. In this section, the conditions for which the output PW and SW spectra have a Lorentzian profile will be determined, within a given level of tolerance.

Since a purely Lorentzian spectrum is characteristic of linear systems, it is expected to occur for small nonlinearities, i.e. for small β_{10}, β_{30}. Expanding the expression (3.36) and (3.37) into a power series with respect to β_{10} and β_{30}, we get the following linear approximations

$$P(\xi_1) = -x(\xi_1) + 1 = -\frac{\beta_{30}}{1+\xi_1^2} - \frac{1}{2}\frac{\beta_{30}(\beta_{30}-\beta_{10})}{(1+\xi_1^2)^2}\ldots \tag{3.40}$$

$$S(\xi_1) = \mu(\xi_1) - 1 = \frac{\beta_{10}}{1+\xi_1^2} + \frac{1}{2}\frac{\beta_{30}(\beta_{30}-\beta_{10})}{(1+\xi_1^2)^2}\ldots \tag{3.41}$$

It can be seen from (3.40) and (3.41) that the first (linear) term is representative of a Lorentzian profile, (while higher terms distort it). Ensuring that these distortions are much smaller than the Lorentzian term, we require that

$$\begin{aligned} \beta_{10} &<< 1 \\ \beta_{30} &<< 1 \end{aligned} \tag{3.42}$$

For a nonlinear phenomenon like SBS, the spectral shape inevitably deviates from the Lorentzian profile as either the pump power (β_{30}), or Stokes power (β_{10}) are increased. It can be seen from Figure 3.6 that the spectrum becomes flattened more quickly than it widens in the onset of spectral distortions. As such, the sharpness of the spectral tip is more sensitive to the changes in the spectral shape, as compared to the *FWHM* of the spectrum. For this reason, we measure the deviation of the spectral shape from the Lorentzian shape by using the relative deviation of the curvature, C_R, of the distorted spectral tip as compared to the Lorentzian spectral tip, according to the following expression.

$$C_R = \left| \frac{C_{PW} - C_{Lorentz}}{C_{Lorentz}} \right| \tag{3.43}$$

Using the standard definition of the curvature of the plain curve, as well as expressions (3.36) and (3.37) respectively, we yield the following expressions for the curvatures of the PW and SW, C_{PW} and C_{SW}, respectively.

$$C_{PW} = 2\beta_{10} x_0 \left(\beta_{30} x_0 + 1 \right) \tag{3.44}$$

$$C_{SW} = -2\beta_{30} x_0 \left(\beta_{30} x_0 + 1 \right) \tag{3.45}$$

Where x_0, β_1 and β_3 are defined in (3.38). From expressions (3.40) and (3.41) we find the curvature of the corresponding Lorentzian profiles (maximum curvature) for the PW and SW, respectively, is

$$C_{Lorentz} = 2\beta_{10} \quad \text{for the PW} \tag{3.46}$$

$$C_{Lorentz} = -2\beta_{30} \quad \text{for the SW} \tag{3.47}$$

Choosing a tolerance δ , we get the following inequality for a quasi-Lorentzian spectral shape

$$C_R < \delta \tag{3.48}$$

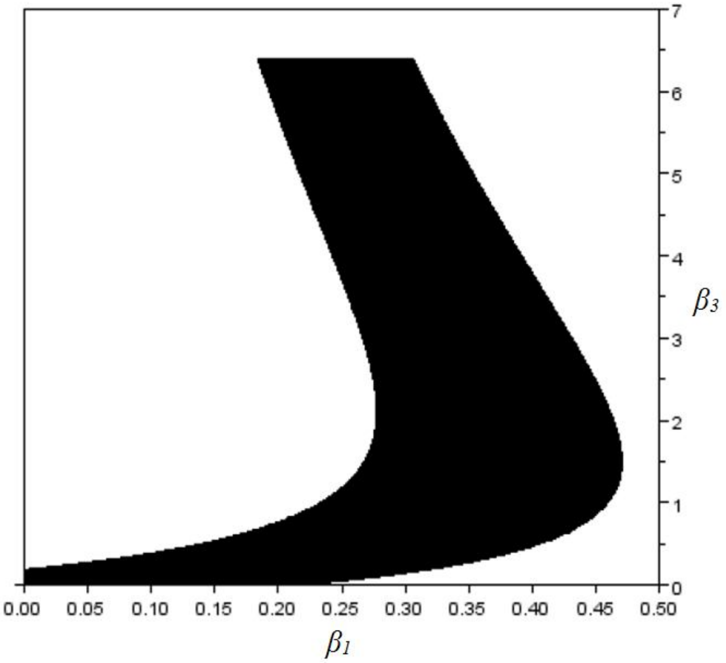

Figure 3.8 Shaded area depicts range of β_1 and β_3 values which yield curvatures within 20% of the Lorentz Curvature for both PW and SW spectra.

The range of β_1 and β_3 values for which the tolerance does not exceed $\delta = 0.20$ from the ideal Lorentzian curvature is shown in Figure 3.8 above. For clarity, the scales along the β_1 and β_3 axes are different. A tolerance of 20% may not be achieved for β_1-values exceeding 0.50, corresponding to a power range of $0<P_{SW}<0.8$mW for fiber parameters in Figure 3.6, while it is possible to choose any β_3-value, which corresponds to the power range $0<P_{PW}<10$mW, provided it is coupled to the correct β_1-value.

This reflects the current theory in which weak pulse powers are usually utilized for sensing applications, since this is the regime in which a Lorentz-like profile may be achieved. As such, fiber and strain measurements (measurements of the Stokes wave) are best conducted within the β-parameters shown in Figure 3.8, provided that other factors, not considered here, do not require otherwise.

3.10 Experiment

3.10.1 Experimental Setup

The spectral distortion from the previous section is verified with an experiment, the setup of which is shown in Figure 3.9. Two narrow linewidth (3kHz) fiber lasers operating at 1310 nm are used to provide the pump and Stokes waves, respectively. The frequency difference is locked by a frequency counter and is automatically swept to cover the Brillouin range. A 12-GHz bandwidth high-speed detector is used to measure the beating signal of the pump and Stokes waves, providing feedback to the frequency counter to lock their frequency differences. The pump laser is launched into an optical circulator, which passes through into the fiber under test (FUT), which is a 1 km Corning SMF-28e capable of sustaining the relatively high powers needed for the 100% depletion regime. The Stokes laser is launched into the FUT, to interact with the pump wave, after which it re-enters the optical circulator.

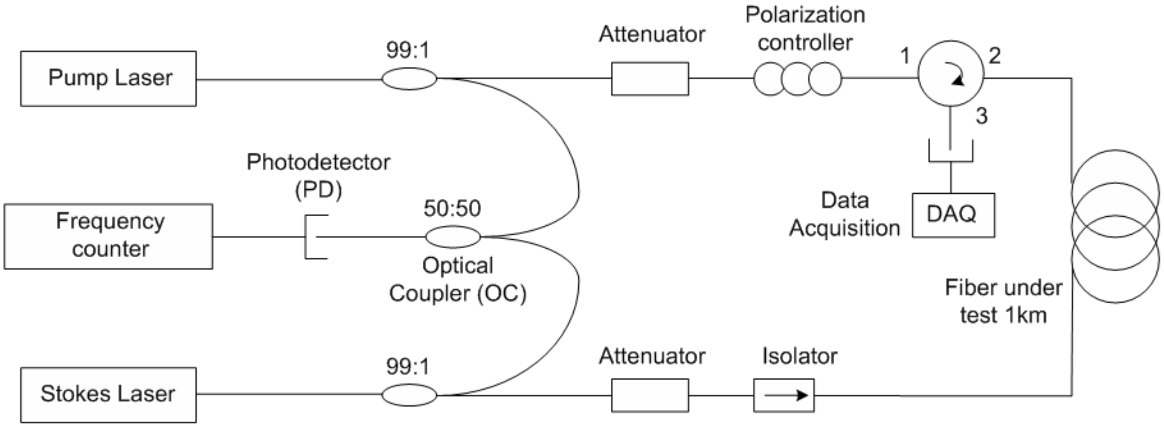

Figure 3.9 Experimental setup.

3.10.2 Experimental Results

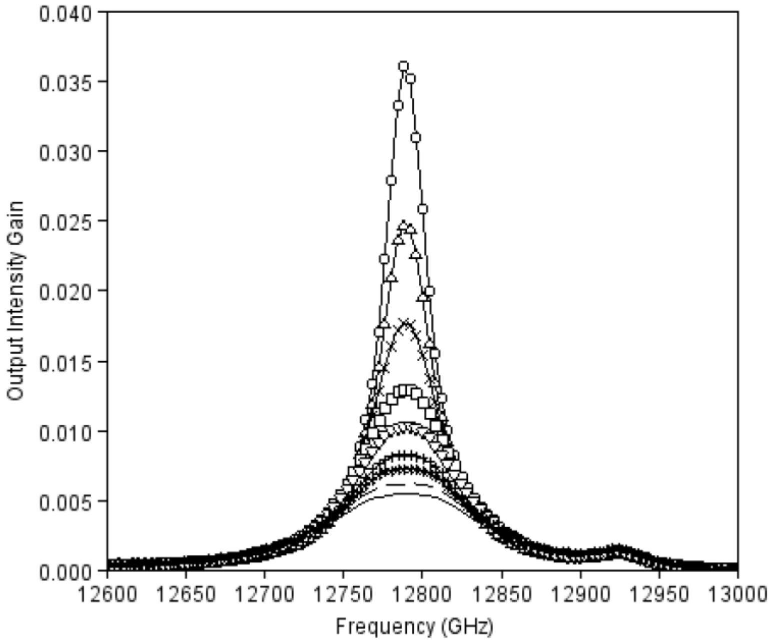

Figure 3.10 Experimental results, normalized intensity units of the SW.

P_{SW} (mW) = ○ 0.01; △ 1.8; × 6.6; □ 12.1; ▽ 17.1; + 22.4; ∗ 27.2; --- 31.8; ▬ 36.3

n=1.48, γ_e=0.902, λ=1319nm, ρ_0=2.21 g/cm^3, v=5616 m/s, L=1000m, Γ_B=0.1 GHz, P_{PW} = 1.0 mW.

As can be seen from Figure 3.10 above, the same kind of spectral distortion is seen in the experimental results as was shown by the analytical expression in Figure 3.6. For both the experimental and theoretical results, the Lorentzian spectrum is maintained for low depletion, i.e. when $P_{SW} <\sim P_{PW}$, and when $P_{SW} >> P_{PW}$, the intensity drop at resonance is more and more gradual, and the shape becomes flatter. The second, smaller peak seen at 12925 MHz is a result of second-order Brillouin scattering effects [74], which are not taken into consideration in this work.

3.11 Summary

Accurate analytic expressions have been obtained for PW Brillouin amplification, describing the intensities of the PW and SW for any coordinate inside the fiber, without any underlying assumptions about the behaviour of the pump or Stokes waves. Among these solutions are: (i) the linear approximation which gives a maximum relative error of 33%, and (ii) the quadratic approximation which gives a maximum relative error of 6.5%. The nonzero relative errors stated above apply to the particular collection of parameters chosen in this chapter, however, the relative error for the above analytic solutions quickly decreases to 0% for the majority of parameters.

Additionally, analytic solutions for the output pump and Stokes spectra have been obtained to good accuracy, as well as an expression for the *FWHM*. These solutions model a spectral distortion effect, which takes place at high pump depletions and high Stokes powers, and is confirmed experimentally. In sensing applications, the *3D parametric model* may be used to avoid parameter combinations which yield this unwanted spectral distortion effect, such as in distributed sensing where PW depletion is substantial.

The *3D parametric model* can also be used to classify the similarity between various Brillouin amplification processes, making it possible to attain the same PW output intensity with a different collection of parameters of the fiber.

Chapter 4

SBS Optical Phase Modulator and Network

4.1 Introduction

Like described in section 1.3, there exist several technologies for optical phase modulation, each having respective drawbacks and limitations. In this section, an optical phase modulator based on the principles of stimulated Brillouin scattering (SBS) and an optical network using the same are proposed, which mitigate the disadvantages of current technology.

4.2 Theory

In this section, new results are presented on the phase relationships between a pump wave (PW), which is taken to be a continuous wave, and a Stokes wave (SW), undergoing stimulated Brillouin scattering (SBS) in an optical fiber, as depicted in the schematic arrangement of Figure 2.6 of Chapter 2.

The pump wave is generated by a pump laser source, which may be a tunable laser source, generating light at about 1549.4 nm, followed by an erbium-doped fiber amplifier (EDFA). The Stokes wave is generated by a SW laser source, which may also be another tunable laser source, or an erbium doped fiber laser. The frequency difference between the pump and Stokes waves is controlled with a phase locked loop which is locked to the resonant Brillouin frequency, Ω_B, of the fiber under test. The optical fiber is a standard single-mode fiber (SMF), such as those manufactured by Corning.

The interaction between the PW, SW, and an acoustic wave (AW_1), created due to electrostriction in the optical fiber, is described by the steady-state system of equations (4.1)-(4.3) from section 2.4.4, shown below. As originally introduced in Chapters 2 and 3, the angular frequency of the acoustic wave, Ω_1, is defined as the frequency difference between the pump and Stokes waves, ω_1 and ω_2 respectively: $\Omega_1=\omega_1-\omega_2$.

$$-\frac{\partial A_1}{\partial z}=\frac{i\omega_1\gamma_e}{2nc\rho_0}\rho_1 A_2 \tag{4.1}$$

$$\frac{\partial A_2}{\partial z}=\frac{i\omega_2\gamma_e}{2nc\rho_0}\rho_1^* A_1 \tag{4.2}$$

$$\left(\Omega_B^2-\Omega_1^2-i\Omega_1\Gamma_B\right)\rho_1=\frac{\gamma_e q_1^2}{4\pi}A_1A_2^* \tag{4.3}$$

Here, $\boldsymbol{q}_1$ is the acoustic wavevector defined as $\boldsymbol{q}_1\approx 2\boldsymbol{k}_1$, where $\boldsymbol{k}_1$ is the wavevector of the PW, defined as $|\boldsymbol{k}_1|=n\omega_1/c$. Complex amplitudes of the waves were represented in polar form as $A=|A|e^{i\varphi}$, and the system of equations (4.1)-(4.3) was transformed into the following extended system of equations.

$$\frac{dY_1}{dl}=\beta_1Y_1Y_2 \tag{4.4}$$

$$\frac{dY_2}{dl}=\beta_3Y_1Y_2 \tag{4.5}$$

$$\frac{d\varphi 1}{dl}=\beta_5Y_2 \tag{4.6}$$

$$\frac{d\varphi_2}{dl}=-\beta_7Y_1 \tag{4.7}$$

Where: φ_1 – phase of pump wave, φ_2 – phase of Stokes wave, and where the β_1, β_3 -coefficients are defined as in equations (3.11) and (3.12) from chapter 3, with

$$\beta_5=\frac{\gamma_e^2k^3LP_{20}}{\pi r^2n^3c\rho_0\Omega_1\Gamma_B}\cdot\frac{\xi_1}{1+\xi_1^2}$$

$$\beta_7=\frac{\gamma_e^2k^3LP_{10}}{\pi r^2n^3c\rho_0\Omega_1\Gamma_B}\frac{\omega_2}{\omega_1}\cdot\frac{\xi_1}{1+\xi_1^2}$$

where ξ_1 is defined in equation (3.8). The sub-system of equations (4.4) and (4.5) can be solved independently of the remaining sub-systems of equations (4.6) and (4.7) for the PW and SW interaction, to determine the intensities of the interacting optical waves Y_1 and Y_2.

Many important properties of the equations (4.4) and (4.5), and (4.6) and (4.7) can be studied even before the formal solution for the intensities are obtained:

a) The rate of change of the phase of the pump wave is proportional to the intensity of the Stokes wave and does not depend on the intensity of the pump wave. Similarly, the rate of change of the phase of the Stokes wave is proportional to the intensity of the pump wave and does not depend on the intensity of the Stokes wave.

b) The rates of change of both optical waves, the pump and the Stokes wave, have common β-coefficients of proportionality, as defined in expressions (3.11)-(3.13). The β-coefficients are comprised of two factors, the first factor being the line-center *gain factor* for the intensities of the optical waves:

$$g_1 = \frac{\gamma_e^2 k_1^3}{n^3 c \rho_0 \Omega_1 \Gamma_B} I_{20} L \tag{4.8}$$

$$g_3 = \frac{\gamma_e^2 k_1^3}{n^3 c \rho_0 \Omega_1 \Gamma_B} \frac{\omega_2}{\omega_1} I_{10} L \tag{4.9}$$

The second factor is a *form factor*

$$F(\xi_1) = \frac{\xi_1}{\xi_1^2 + 1}, \tag{4.10}$$

with $$\xi_1 = \frac{\Omega_B^2 - \Omega_1^2}{\Omega_1 \Gamma_B} \tag{4.11}$$

The *form factor* determines the shape of the phase spectra of the interacting waves. The graph of the *form factor* $F(\xi_1)$ is shown in Figure 4.1 below. This general shape is attributed to the SBS-induced index change [61], Δn_{SBS}, which results from changes in the gain (or loss) of a medium according to the Kramers-Kronig relations [1, 61].

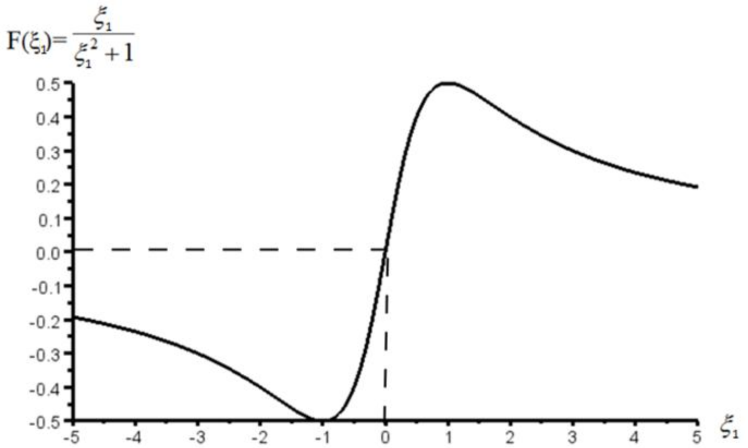

Figure 4.1 Form factor as a function of ξ_1.

Since $F(\xi_1)$ has two extrema at $\xi_1=\pm 1$, the optimum conditions for observing a phase change occur when

$$\frac{\Omega_B^2-\Omega_1^2}{\Omega_1\Gamma_B}=\pm 1 \tag{4.12}$$

Since Ω_1 differs very little from the resonant Brillouin frequency, Ω_B, for many practical cases, we may apply the approximation $\Omega_1+\Omega_B\approx 2\Omega_1$, and the optimum condition for observing the phase change becomes

$$\Omega_1\approx\Omega_B\pm\frac{\Gamma_{\mathbf{B}}}{2} \tag{4.13}$$

In other words, for intensity spectra having a substantially Lorentzian shape, the optimal phase change occurs when the pump wave, or the Stokes wave, or both, are detuned from the resonant Brillouin frequency, Ω_B, by about half of the Brillouin linewidth, Γ_B, of the optical fiber. Similarly, the maximum SBS-induced refractive index change also occurs at the optimum conditions (4.13).

Though not optimal, for other values of detuning off the resonant Brillouin frequency between the pump wave and Stokes wave, the phase change also occurs. For example, the difference of frequencies of the pump wave and the Stokes wave may be conveniently chosen within a range of about ± 25% from half a Brillouin linewidth.

It must be confirmed that the optimal condition (4.12) does not lead to a negligibly small intensity of the interacting waves when they are off-resonance. Performing a similar analysis on the equations (4.4) and (4.5), and (4.6) and (4.7) describing the rate of change of the intensity of the PW and SW, we note that the equations have a common *gain factor* (4.14)

$$G_1(\xi_1) = \frac{1}{1+\xi_1^2} \tag{4.14}$$

The graph of $G(\xi_1)$ is shown on Figure 4.2 below, from which it can be seen that $G_1(\pm 1)=1/2$. This implies that when the angular frequency of the AW$_1$ follows the relation $\Omega_i \approx \Omega_B \pm \frac{\Gamma_B}{2}$, the off-resonance *gain factor* drops only by 50%, as compared with the *gain factor* at $\xi_1=0$ (line-center *gain factor*). This means that the optimum condition (equation 4.12) leads to sufficient intensities, from an experimental point of view, of the interacting waves.

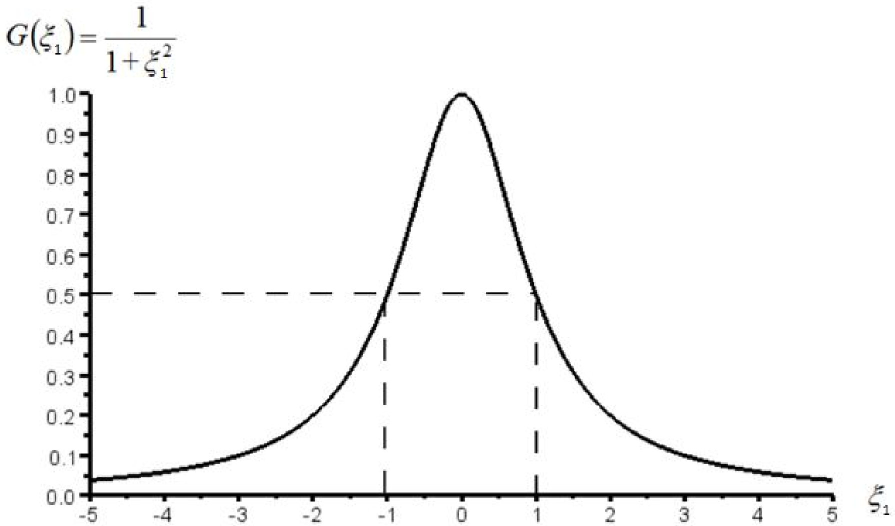

Figure 4.2 Gain factor as a function of ξ_1.

From observation of Figure 4.1, it may be concluded that

$$F(0)=0 \tag{4.15}$$

For which we have $\beta_5=\beta_7=0$, and therefore

$$\frac{\partial \varphi_i}{\partial z}=0 \qquad \text{when } \Omega_1=\Omega_B,\ i=1,2. \tag{4.16}$$

In other words, *at the resonant Brillouin frequency, the phases of the pump wave and the Stokes wave remain constant at every point in the fiber.*

Likewise, off-resonance, i.e. When $\Omega_1 \neq \Omega_B$, we have

$$|F(\xi_1)|>0 \tag{4.17}$$

For which we have $\beta_5, \beta_7 > 0$. Therefore,

$$\frac{\partial \varphi_i}{\partial z} \neq 0, \quad i=1,2. \tag{4.18}$$

In other words, *the phases of the pump wave and Stokes wave change along the fiber if* $\Omega_1 \neq \Omega_B$ *i.e detuned from the resonant Brillouin frequency.*

4.3 Proposed Experimental Setup

To demonstrate the proposed theory of section 4.2, an experimental setup is proposed, which is shown in Figure 4.3.

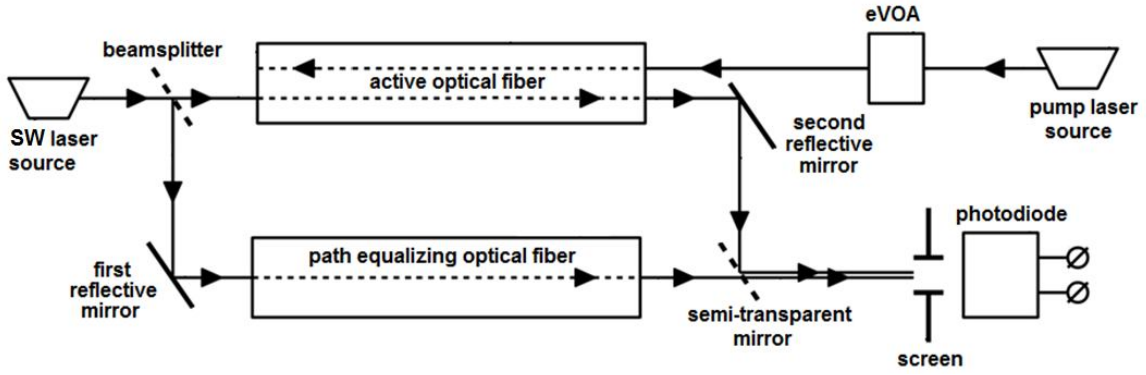

Figure 4.3 Experimental setup.

The experimental setup is comprised of a SW laser source, a beamsplitter, a pump laser source, an electronic variable optical attenuator (eVOA), which is used as a source of amplitude modulation, an active Brillouin scattering optical fiber, a path equalizing optical fiber, a first and second reflective mirror, a semi-transparent mirror, a screen with tiny aperture, and a photodiode.

The experimental setup of Figure 4.3 operates as follows. The pump laser source, for example, a tunable laser source, generates a pump wave, which passes through the eVOA. The resulting wave is an amplitude modulated pump wave, which is injected into one end of the active optical fiber. The SW laser source, for example a tunable laser source, generates a Stokes wave which encounters the beamsplitter, and is split into an incident Stokes wave and a reference optical signal. The incident Stokes wave is injected into the opposite end of the active optical fiber, such that the incident Stokes wave and the amplitude modulated pump wave counter-propagate in the active optical fiber, causing the phase of the incident Stokes wave to change according to the equation (4.7).

For clarity of the experimental setup of Figure 4.3, the second reflective mirror is schematically shown as spatially separated from the pump wave. In practice, the second reflective mirror is replaced with a second semi-transparent mirror.

In accordance with the theory recommendations in the section 4.2 above, the frequency of the Stokes wave is detuned from the resonant Brillouin frequency to create conditions necessary for the phases of the amplitude modulated pump wave and the incident Stokes wave to change. Preferably, the frequency of the Stokes wave is chosen to satisfy the optimal conditions as described in equation (4.13) above, to induce a maximum phase change, thereby making it easier to measure. An output Stokes wave, with the phase changed in accordance with the chosen attenuation of the eVOA, is reflected off the second reflective mirror, at about a 90° angle, creating a phase modulated Stokes beam.

The first reference optical signal is reflected at about a 90° angle off a first reflective mirror, to create a second reference optical signal, which is passed through a path equalizing optical fiber that is substantially identical to the active Brillouin scattering optical fiber in all respects. The result is an output reference beam which exits the path equalizing optical fiber, the purpose of which is to equalize the optical path for the first reference optical signal with the optical path of the incident Stokes wave, keeping both mutually coherent. Since the typical coherence length of a typical laser, such as an He-Ne laser, is around 20 cm, the difference in optical paths between the active Brillouin Scattering optical fiber and the path equalizing optical fiber should be much smaller than 20 cm, preferably not exceeding several centimeters.

The output reference beam passes through a semi-transparent mirror, while the phase modulated Stokes beam is reflected from the semi-transparent mirror, such that both the output reference beam and the phase modulated Stokes beam converge to create an interference pattern on the screen with tiny aperture. The angle of convergence is selected to be small enough (preferably substantially smaller than 1`) to widen the interference pattern, such as a 10 mm wide interference pattern. The required convergence angle can be estimated from the expression $2d\cdot\sin(\vartheta)=\lambda$, where λ is the wavelength, d is the width of the interference patterns, and 2ϑ is the convergence angle between the phase modulated Stokes beam and the output reference beam.

When the interference pattern becomes visible, the convergence angle can be adjusted experimentally as required. To maintain the stability of the interference pattern for the amount of time required for measurements (presumably ~ 5-10 min), the entire setup is preferably mounted on an anti-vibrational table or breadboard, such as produced by Newport Corporation.

The aperture on the screen with tiny aperture is chosen to be much smaller in diameter than the width of the light and dark bands of the interference pattern, which permits the light from the interference pattern to be detected by the photodiode. Initially, the aperture is adjusted to occupy a position of an interference pattern at about a middle point between a light and a dark band of the interference pattern, which provides for a substantially linear region of intensity variation. When the eVOA is controlled to a different attenuation from the initial attenuation, the phase of the output Stokes wave is expected to change relative to the phase of the output reference beam, causing the light and dark bands of the interference pattern to change locations relative to the aperture in the transverse direction. Therefore, the amount of light that reaches the photodiode changes approximately proportionally to the phase shift, allowing the phase shift to be measured.

A controllable change of attenuation of the eVOA allows for the measurement of the phase shift versus the intensity of the amplitude modulated pump wave. Simulation results are shown in Table 4.1 below.

Table 4.1 Simulation results for the experimental setup

Parameters of the Fiber	Detuning	Phase Change of SW (rad)
γ_e=0.902 ω_1=8.381097·10^5 GHz ω_2= 8.380691·10^5 GHz Ω_1=4.053668·10^1 GHz Ω_B=4.053668·10^1 GHz n=1.45, c= 299792.458 km/s v=5000 m/s, ρ_0=2.21 g/cm^3 Γ_B = 0.1 GHz, L=1000 m PW power: P_{PW}=10mW SW power: P_{SW}=9mW	$\Omega_1 \approx \Omega_B \pm 0.5\Gamma_{\mathbf{B}}$ (optimal conditions)	~1.2
	$\Omega_1 \approx \Omega_B \pm 0.25\Gamma_{\mathbf{B}}$	~0.2
	$\Omega_1 \approx \Omega_B \pm 0.1\Gamma_{\mathbf{B}}$	~0.08

As can be seen from Table 4.1, the phase change of the output Stokes wave is sufficiently large and suitable for conducting measurements. It has also been noticed that, when the pump wave is amplitude modulated, the phase change of the output Stokes wave is larger for pump waves experiencing larger depletion, for example, when the depletion of the pump wave is larger than about 50%.

Also, the Stokes wave can be amplitude modulated instead of the pump wave, thus causing a phase modulation of the pump wave.

4.4 Optical phase modulator construction

An optical phase modulator based on the principles outlined in Sections 4.2 and 4.3 is shown in Figure 4.4 below. It comprises an active Brillouin scattering optical fiber, a pump and SW laser source, for example tunable laser sources, an eVOA, and a reflective mirror.

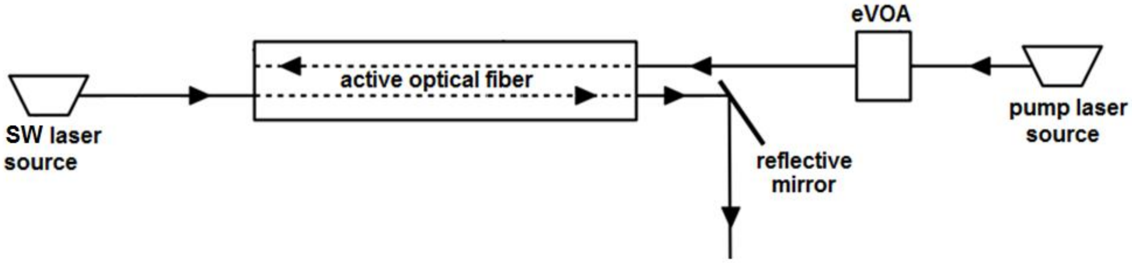

Figure 4.4 Optical phase modulator construction.

For clarity of the setup of Figure 4.4, the reflective mirror is schematically shown being spatially separated from an amplitude modulated pump wave. In practice, the reflective mirror is replaced with a semi-transparent mirror.

In Figure 4.4, the pump laser source generates a pump wave, the amplitude of which is modulated by a low frequency signal (for example speech signal, which is not shown) using the amplitude modulator, such as an eVOA. The resulting amplitude modulated pump wave is injected into one end of the active optical fiber. A Stokes wave is generated by the SW laser source, that is injected into the opposite end of the active optical fiber, such that the two waves counter-propagate in the active optical fiber. The SW laser source is used to detune the frequency of the Stokes wave from the resonant Brillouin frequency, causing the phase of the Stokes wave to change in accordance with the intensity of the amplitude modulated pump wave. Preferably, the frequency of the Stokes wave is chosen to satisfy the optimal conditions of equation (4.13), or to tune the difference to about half of a Brillouin linewidth of the optical fiber, to make the phase change as large as possible, and improve a signal-to-noise ratio (SNR). An output Stokes wave, the phase of which has already been modulated, is reflected off the reflective mirror, creating a phase modulated Stokes wave for carrying the signal, e.g. phase modulated speech signal.

The Stokes wave may also be amplitude modulated independently of the phase modulation, thus allowing for doubling the amount of information carried by the same phase modulated Stokes wave. Also, the Stokes wave can be amplitude modulated instead of the pump wave, thus causing the phase modulation of the pump wave.

4.4 Optical network transmission lines with phase-modulated carriers

It is also possible to construct and optical network employing the optical phase modulator of section 4.3, which would allow for the transmission of a low frequency signal through an optical fiber, via the phase-modulated carrier and demodulation of the carrier into the original low frequency signal.

An optical network utilizing the principles of optical phase modulation from previous sections is shown in Figure 4.5.

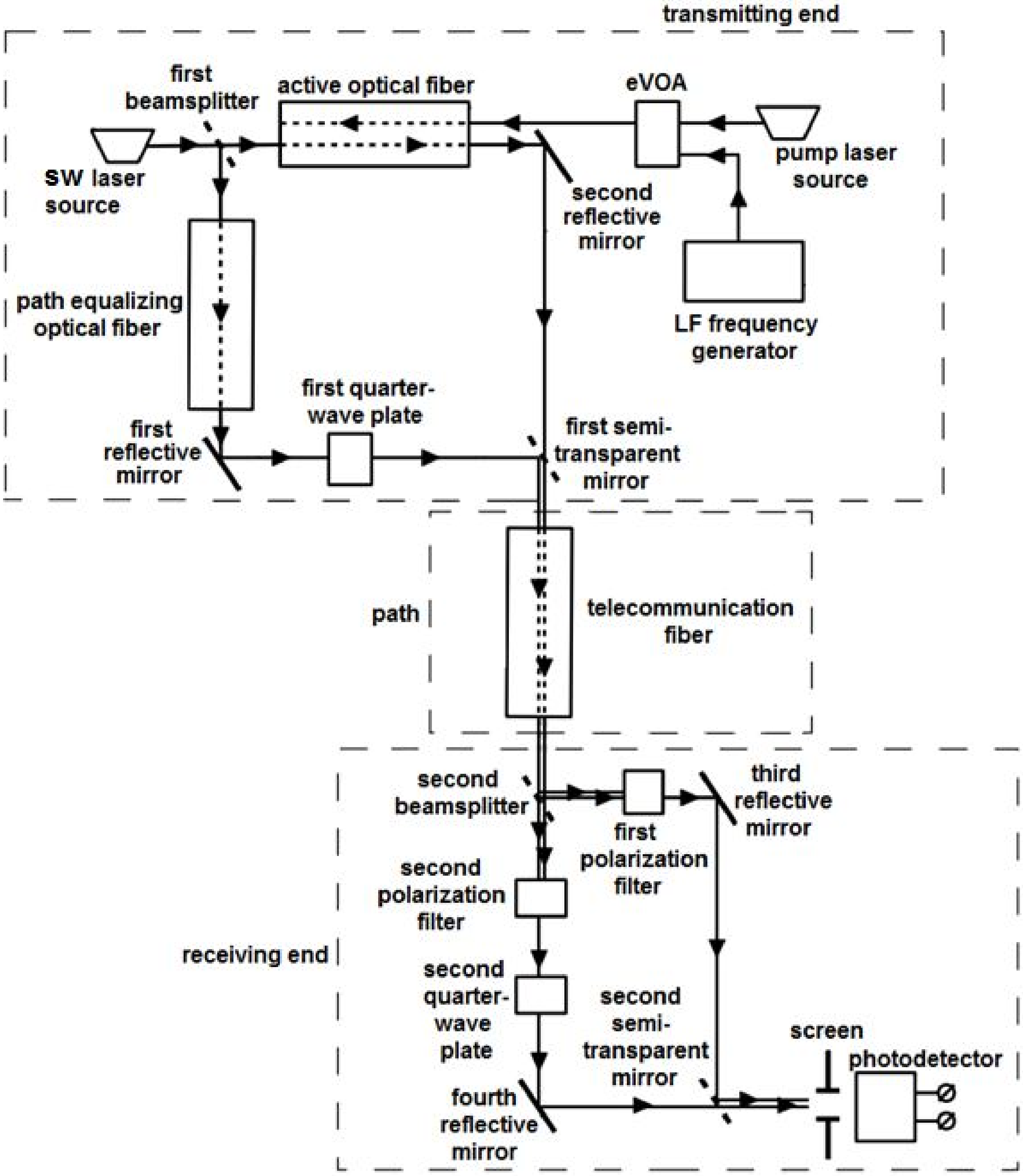

Figure 4.5 Optical network construction.

The optical network of Figure 4.5 comprises a transmitting and receiving end of the optical network from Figure 4.3, which are connected via a path in the optical network. The transmitting end of the optical network comprises a pump laser source, a first beamsplitter, an SW laser source, an amplitude modulator (eVOA), a low frequency (LF) signal generator, an active Brillouin scattering optical fiber, a passive path equalizing optical fiber, a first and second reflective mirror, a first quarter-wave plate, and a first semi-transparent mirror.

The receiving end of the optical network comprises a second beamsplitter, a first and second polarization filter, a second quarter-wave plate, a third and fourth reflective mirror, a second semi-transparent mirror, a screen with a pinhole, and a photodetector.

The path in the optical network comprises a telecommunication fiber acting as a transmission channel.

The pump laser source generates a pump wave, which may also be referred to as a first optical signal. The first beamsplitter acts to split the pump wave into a pump wave to be phase modulated and a reference optical signal, both with parallel polarization.

The SW laser source generates a Stokes wave, which may also be referred to as a second optical signal. The Stokes wave and a low frequency signal, which is generated by the low frequency signal generator, are sent to the amplitude modulator which generates an amplitude-modulated wave, or AM carrier. The AM carrier is injected into one end of the active optical fiber, while the pump wave to be phase modulated is injected into an opposite end of the active optical fiber. The pump wave to be phase modulated and the AM carrier counter-propagate inside the active Brillouin scattering optical fiber, resulting in transforming the pump wave to be phase modulated into a phase modulated pump wave, also with parallel polarization.

For clarity of the setup of Figure 4.5, the first reflective mirror is schematically shown as spatially separated from a AM carrier. In practice, the first reflective mirrors replaced with a third semi-transparent mirror.

The phase modulated pump wave is reflected off the first reflective mirror, at about a 90° angle, creating a phase modulated optical signal. Likewise, the reference optical signal enters the passive path equalizing optical fiber, which acts as an optical path equalizer, and is then reflected off the second reflective mirror at about a 90° angle, creating a reference wave. The reference wave passes through the first quarter-wave plate, which changes its polarization to a perpendicular polarization, resulting in a first perpendicular polarized reference beam. The first perpendicular polarized reference beam is perpendicularly polarized, while the phase modulated optical signal is still parallel polarized.

The phase modulated optical signal passes through the first semi-transparent mirror, resulting in a polarization perpendicular reference beam, while the first perpendicular polarized reference beam is reflected, at about a 90° angle, resulting in a polarization parallel phase modulated beam. Both the polarization perpendicular reference beam and the polarization parallel phase modulated beam, which in Figure 4.5 are drawn separate from each other only for the purpose of clarity, enter the telecommunication fiber. Upon exiting the telecommunication fiber, the polarization perpendicular reference beam becomes a destination reference beam, and the polarization parallel phase modulated beam becomes a destination phase modulated beam. Both the destination reference beam and the destination phase modulated beam encounter the second beamsplitter, which redirects them to the first and second polarization filters.

The first polarization filter allows only the destination phase modulated beam to pass through, to be reflected off the third reflective mirror, as well as the second semi-transparent mirror, to produce a converging phase modulated beam. The polarization filter allows only the destination reference beam to pass through, creating a second perpendicular polarized reference beam. The resulting second perpendicular polarized reference beam passes through the second quarter-wave plate, which is polarization to parallel, resulting in a first parallel polarized reference beam. The first parallel polarized reference beam is reflected off the fourth reflective mirror, and passes through the second semi-transparent mirror, producing a converging reference beam.

The resulting converging phase modulated beam and the converging reference beam, both with the same polarization, converge at a small angle (preferably smaller than 1`), and overlap on a screen with a pinhole. The light passing through is detected by the photodetector.

When the phase of the converging phase modulated beam changes (due to the phase modulation) relative to the phase of the converging reference beam, the interference pattern, of variable intensity, shifts in the transverse direction approximately proportionally to the change in phase. As a result, the intensity of light which passes through the screen with a pinhole also changes respectively. In this way, the low frequency signal is decoded from the converging phase modulated beam. Consequently, we were able to transmit the low frequency signal through an optical network to its destination and restore it at this destination.

It is also possible to amplitude modulate the pump wave with the amplitude modulator, independently of the phase modulation, and as mentioned in previous sections, the pump wave may also be amplitude modulated instead of the Stokes wave, thus causing the phase modulation of the Stokes wave.

Finally, instead of using two differently polarized beams: the phase modulated optical signal and the first perpendicular polarized reference beam, propagating through the same telecommunication fiber, two separate fibers with substantially similar characteristics could be used so that one fiber propagates the phase modulated optical signal, while another fiber propagates the first perpendicular polarized reference beam. In this case, both the phase modulated optical signal and the first perpendicular polarized reference beam may have similar polarizations, and the second quarter-wave plate will not be needed for producing the interference pattern.

4.5 Summary

Therefore, an improved method of phase-modulation, based on the principles of stimulated Brillouin scattering, has been proposed, as well as an optical phase network employing the same.

Chapter 5

Polarization Effects in SBS

5.1 Introduction

As described in section 1.4, this chapter will introduce several important applications of birefringence in optical fibers, relating to telecommunications and fiber sensing. The effect of the spectral shift due to increased birefringence is investigated, as well as spectral distortion due to various degrees of birefringence will be investigated for steady-state and transient pulsed regimes. Namely, the steady-state model presented for linearly polarized (LP) light will be shown to be a valuable measure of the experimentally realistic case of non-ideal LP light in optical fibers. The degree of spectral distortion may be used as an indication of the quality of linear polarization during the SBS interaction, or as a measure of power leaking between the fast and slow modes. Furthermore, increased power leaking between the fast and slow modes for LP can be used to create a regime that is more favourable for sensing applications related to SBS. In the pulsed regime, spectral broadening and depletion of the Stokes spectrum will be observed as a result of increased birefringence. Spectral distortion is detrimental for fiber sensing and telecommunications, hence methods of minimizing this effect are important to investigate.

Additionally, the effects of various elliptical polarizations on output spectral shape will be investigated for the steady-state model, including spectral spreading effects and spectral broadening. Methods of maintaining a pulse fidelity and full width at half maximum (*FWHM*), as compared to non-polarized light in a non-birefringent fiber, will be proposed.

In this chapter, the most comprehensive SBS equations are presented, considering the birefringence effects in optical fibers. Besides the usual slowly varying amplitude approximation, the only extra approximation of the model is the assumption that the phonon fields are established almost instantaneously, namely, the time it takes for the acoustic phonons to build up is considered to be negligible.

5.2 Model

The process of SBS has been studied in a birefringent polarization-maintaining optical fiber (PMF) with a core radius of 4.1μm. The configuration is comprised of a pump wave (PW) launched into one end, and a Stokes wave (SW) launched into the other end. Both the PW and SW have *x*- and *y*- eigen-polarization components. The schematic arrangement is shown in Figure 5.1 below.

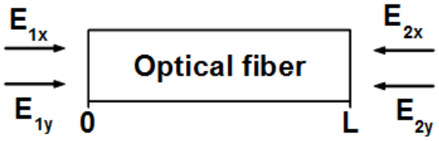

Figure 5.1 Schematic arrangement of SBS in an optical fiber of length *L*.
E_{1x} – Pump wave, E_{1y} – Pump wave, E_{2x} – Stokes wave, E_{2y} – Stokes wave

In the slowly varying amplitude approximation, the interaction between the PW and SW as shown in Figure 5.1, is described by the system of equations (5.1)-(5.4). The only additional approximation in establishing the following equations is the assumption that the phonon fields are established almost simultaneously [1, 9]. The derivation of equations (5.1)-(5.4) is shown in the *Appendix*.

$$\begin{aligned}
&\frac{\partial E_{1x}}{\partial z}+\frac{\overline{n}_1}{c}\frac{\partial E_{1x}}{\partial t}+\left(\overline{\alpha}_1+\frac{\Delta\overline{\alpha}_1}{2}+i\frac{\Delta\overline{n}_1\omega_1}{2c}\right)E_{1x}\\
&=i\frac{\gamma_e^2\omega_1^2}{2\rho_0c^2v}\frac{1}{\left(\Omega_{Bxx}-\Omega_1\right)-i\frac{\Gamma_B}{2}}E_{1x}E_{2x}^*E_{2x}\frac{1}{2}\left(1+\mathbf{S}_{x1}\cdot\mathbf{S}_{x2}\right)\\
&+i\frac{\gamma_e^2\omega_1^2}{2\rho_0c^2v}\frac{1}{\left(\Omega_{Bxy}-\Omega_1\right)-i\frac{\Gamma_B}{2}}E_{1x}E_{2y}^*E_{2y}\frac{1}{2}\left(1+\mathbf{S}_{x1}\cdot\mathbf{S}_{y2}\right)
\end{aligned}\tag{5.1}$$

$$\begin{aligned}&\frac{\partial E_{1y}}{\partial z}+\frac{\overline{n}_1}{c}\frac{\partial E_{1y}}{\partial t}+\left(\overline{\alpha}_1-\frac{\Delta\overline{\alpha}_1}{2}-i\frac{\Delta\overline{n}_1\omega_1}{2c}\right)E_{1y}\\&=i\frac{\gamma_e^2\omega_1^2}{2\rho_0c^2v}\frac{1}{\left(\Omega_{Byy}-\Omega_1\right)-i\frac{\Gamma_B}{2}}E_{1y}E_{2y}^*E_{2y}\frac{1}{2}\left(1+\mathbf{S}_{y1}\cdot\mathbf{S}_{y2}\right)\\&+i\frac{\gamma_e^2\omega_1^2}{2\rho_0c^2v}\frac{1}{\left(\Omega_{Byx}-\Omega_1\right)-i\frac{\Gamma_B}{2}}E_{1y}E_{2x}^*E_{2x}\frac{1}{2}\left(1+\mathbf{S}_{y1}\cdot\mathbf{S}_{x2}\right)\end{aligned}\tag{5.2}$$

$$\begin{aligned}&-\frac{\partial E_{2x}}{\partial z}+\frac{\overline{n}_2}{c}\frac{\partial E_{2x}}{\partial t}+\left(\overline{\alpha}_2+\frac{\Delta\overline{\alpha}_2}{2}+i\frac{\Delta\overline{n}_2\omega_2}{2c}\right)E_{2x}\\&=i\frac{\gamma_e^2\omega_2^2}{2\rho_0c^2v}\frac{1}{\left(\Omega_{Bxx}-\Omega_1\right)-i\frac{\Gamma_B}{2}}E_{2x}E_{1x}^*E_{1x}\frac{1}{2}\left(1+\mathbf{S}_{x1}\cdot\mathbf{S}_{x2}\right)\\&+i\frac{\gamma_e^2\omega_2^2}{2\rho_0c^2v}\frac{1}{\left(\Omega_{Byx}-\Omega_1\right)-i\frac{\Gamma_B}{2}}E_{2x}E_{1y}^*E_{1y}\frac{1}{2}\left(1+\mathbf{S}_{y1}\cdot\mathbf{S}_{x2}\right)\end{aligned}\tag{5.3}$$

$$\begin{aligned}&-\frac{\partial E_{2y}}{\partial z}+\frac{\overline{n}_2}{c}\frac{\partial E_{2y}}{\partial t}+\left(\overline{\alpha}_2-\frac{\Delta\overline{\alpha}_2}{2}-i\frac{\Delta\overline{n}_2\omega_2}{2c}\right)E_{2y}\\&=i\frac{\gamma_e^2\omega_2^2}{2\rho_0c^2v}\frac{1}{\left(\Omega_{Byy}-\Omega_1\right)-i\frac{\Gamma_B}{2}}E_{2y}E_{1y}^*E_{1y}\frac{1}{2}\left(1+\mathbf{S}_{y1}\cdot\mathbf{S}_{y2}\right)\\&+i\frac{\gamma_e^2\omega_2^2}{2\rho_0c^2v}\frac{1}{\left(\Omega_{Bxy}-\Omega_1\right)-i\frac{\Gamma_B}{2}}E_{2y}E_{1x}^*E_{1x}\frac{1}{2}\left(1+\mathbf{S}_{x1}\cdot\mathbf{S}_{y2}\right)\end{aligned}\tag{5.4}$$

Here $\Omega_{Bxx}=\frac{v}{c}\left(n_{1x}\omega_1+n_{2x}\omega_2\right)$, $\Omega_{Byy}=\frac{v}{c}\left(n_{1y}\omega_1+n_{2y}\omega_2\right)$, $\Omega_{Bxy}=\frac{v}{c}\left(n_{1x}\omega_1+n_{2y}\omega_2\right)$, $\Omega_{Byx}=\frac{v}{c}\left(n_{1y}\omega_1+n_{2x}\omega_2\right)$ are the Brillouin frequencies associated with the principal axis beatings [4], where ω_1 is the angular frequency of the PW, and ω_2 is the angular frequency of the SW. n_{1x} and n_{1y}, and n_{2x} and n_{2y}, are the indices of refraction associated with the principal axes of the PW and SW, respectively. Ω_1 is the angular frequency of the AW$_1$ caused by the interaction of the PW and SW. E_{1x} and E_{1y}, and E_{2x} and E_{2y}, are the complex amplitudes of the PW and the SW, respectively. c is the speed of light, ρ_0 is the mean density of the fiber, γ_e is the electrostrictive constant, z is the coordinate along the fiber, v is the speed of sound in the fiber, Γ_B is the Brillouin linewidth, and finally, α_{1x}, α_{1y}, α_{2x}, and α_{2y} represent the fiber attenuations of the principal axes of polarization of the two interacting waves.

The $\boldsymbol{S}_{1x}$, $\boldsymbol{S}_{1y}$, $\boldsymbol{S}_{2x}$, and $\boldsymbol{S}_{2y}$ represent the Stokes vectors in the Poincaré sphere polarization representation [68, 69], and are used to define the polarization of the propagating lights [61, 68]. Some extra relations of importance are the following: $\boldsymbol{S}_{x1} = -\boldsymbol{S}_{y1}$ for forward propagating light (PW), and $\boldsymbol{S}_{x2} = -\boldsymbol{S}_{y2}$ for backward propagating light (SW). Furthermore, it is worthwhile to emphasize that in the above system of equations (5.1)-(5.4), $\boldsymbol{S}_{x1}$ describes the principal state of polarization vector for the forward propagating light, and $\boldsymbol{S}_{x2}$ describes the principal state of the polarization vector of the backward propagating light. In this case, if $\boldsymbol{S}_{x1}$ is defined as $\boldsymbol{S}_{x1} = (a, b, c)$, then it must follow that $\boldsymbol{S}_{y1} = (-a, -b, -c)$, and neglecting the dispersion effect, then $\boldsymbol{S}_{x2} = (a, b, -c)$ and $\boldsymbol{S}_{y2} = (-a, -b, c)$, where a, b and c are the Stokes vector components, the third component, c, describing circular birefringence, and are normalized such that $a^2 + b^2 + c^2 = 1$. From this arrangement it is apparent that for fibers having elliptical birefringence ($0 < |c| < 1$), the most general beating situation will be excited, i.e. there will exist four acoustic resonances.

Lastly, some remaining simplifications were introduced to the system of equations (5.1)-(5.4) to make the birefringence effect more explicit. This can be justified by the fact that birefringence and polarization dependent loss are both small. It is defined $\overline{n}_1 = \frac{n_{1x} + n_{1y}}{2}$, $\Delta\overline{n}_1 = n_{1x} - n_{1y}$, $\overline{n}_2 = \frac{n_{2x} + n_{2y}}{2}$, $\Delta\overline{n}_2 = n_{2x} - n_{2y}$, and $\overline{\alpha}_1 = \frac{\alpha_{1x} + \alpha_{1y}}{2}$, $\Delta\overline{\alpha}_1 = \alpha_{1x} - \alpha_{1y}$, $\overline{\alpha}_2 = \frac{\alpha_{2x} + \alpha_{2y}}{2}$, $\Delta\overline{\alpha}_2 = \alpha_{2x} - \alpha_{2y}$.

In the above arrangement, the PW input parameters are known only at the beginning of the fiber, i.e. at z=0. Correspondingly, the SW input parameters are known only at the end of the fiber, i.e. at z=L, where L is the length of the fiber. Therefore, the boundary conditions for the system of equations (5.1)-(5.4) are similar to previously-studied configurations with one pulse [4, 65]. The conditions for two pulses are as follows:

$$|E_{1x}(0)|^2 = E^2_{1x0}\,; \quad |E_{1y}(0)|^2 = E^2_{1y0}\,; \quad |E_{2x}(L)|^2 = E^2_{2x0}; \quad |E_{2y}(L)|^2 = E^2_{2y0}; \tag{5.5}$$

where E^2_{1x0} , E^2_{1y0} , E^2_{2x0} , and E^2_{2y0} , are known squared absolute values of the complex fields E_{1x} , E_{1y} , E_{2x} , and E_{2y} respectively. In the dimensionless notation, the system of equations (5.1)-(5.4) becomes

$$\frac{\partial Y_{1x}}{\partial \ell} + \overline{n}_1 \frac{\partial Y_{1x}}{\partial \tau} = -\left[\beta_{1a} Y_{2x} + \beta_{1b} Y_{2y}\right] Y_{1x} - \varepsilon_{1x} Y_{1x} \tag{5.6}$$

$$\frac{\partial Y_{1y}}{\partial \ell} + \overline{n}_1 \frac{\partial Y_{1y}}{\partial \tau} = -\left[\beta_{1c} Y_{2y} + \beta_{1d} Y_{2x}\right] Y_{1y} - \varepsilon_{1y} Y_{1y} \tag{5.7}$$

$$-\frac{\partial Y_{2x}}{\partial \ell} + \overline{n}_2 \frac{\partial Y_{2x}}{\partial \tau} = \left[\beta_{3a} Y_{1x} + \beta_{3b} Y_{1y}\right] Y_{2x} - \varepsilon_{2x} Y_{2x} \tag{5.8}$$

$$-\frac{\partial Y_{2y}}{\partial \ell} + \overline{n}_2 \frac{\partial Y_{2y}}{\partial \tau} = \left[\beta_{3c} Y_{1y} + \beta_{3d} Y_{1x}\right] Y_{2y} - \varepsilon_{2y} Y_{2y} \tag{5.9}$$

$$\beta_{1a} = \frac{4\gamma_e^2 k^2 P_{2x0} L}{r^2 \overline{n}_2 \rho_0 c v \Gamma_B} \cdot \frac{1}{2} \frac{1 + \mathbf{S}_{x1} \cdot \mathbf{S}_{x2}}{1 + \xi_{xx}^2} \tag{5.10}$$

$$\beta_{1b} = \frac{4\gamma_e^2 k^2 P_{2y0} L}{r^2 \overline{n}_2 \rho_0 c v \Gamma_B} \cdot \frac{1}{2} \frac{1 + \mathbf{S}_{\mathrm{x}1} \cdot \mathbf{S}_{\mathrm{y}2}}{1 + \xi_{xy}^2} \tag{5.11}$$

$$\beta_{1c} = \frac{4\gamma_e^2 k^2 P_{2y0} L}{r^2 \overline{n}_2 \rho_0 c v \Gamma_B} \cdot \frac{1}{2} \frac{1 + \mathbf{S}_{\mathrm{y}1} \cdot \mathbf{S}_{\mathrm{y}2}}{1 + \xi_{yy}^2} \tag{5.12}$$

$$\beta_{1d} = \frac{4\gamma_e^2 k^2 P_{2x0} L}{r^2 \overline{n}_2 \rho_0 c v \Gamma_B} \cdot \frac{1}{2} \frac{1 + \mathbf{S}_{y1} \cdot \mathbf{S}_{x2}}{1 + \xi_{yx}^2} \tag{5.13}$$

$$\beta_{3a} = \frac{4\gamma_e^2 k^2 P_{1x0} L}{r^2 \overline{n}_1 \rho_0 c v \Gamma_B} \left(\frac{\omega_2}{\omega_1}\right)^2 \cdot \frac{1}{2} \frac{1 + \mathbf{S}_{x1} \cdot \mathbf{S}_{x2}}{1 + \xi_{xx}^2} \tag{5.14}$$

$$\beta_{3b} = \frac{4\gamma_e^2 k^2 P_{1y0} L}{r^2 \overline{n}_1 \rho_0 c v \Gamma_B} \left(\frac{\omega_2}{\omega_1}\right)^2 \cdot \frac{1}{2} \frac{1 + \mathbf{S}_{y1} \cdot \mathbf{S}_{x2}}{1 + \xi_{yx}^2} \tag{5.15}$$

$$\beta_{3c} = \frac{4\gamma_e^2 k^2 P_{1y0} L}{r^2 \overline{n}_1 \rho_0 c v \Gamma_B} \left(\frac{\omega_2}{\omega_1}\right)^2 \cdot \frac{1}{2} \frac{1 + \mathbf{S}_{y1} \cdot \mathbf{S}_{y2}}{1 + \xi_{yy}^2} \tag{5.16}$$

$$\beta_{3d} = \frac{4\gamma_e^2 k^2 P_{1x0} L}{r^2 \overline{n}_1 \rho_0 c v \Gamma_B} \left(\frac{\omega_2}{\omega_1}\right)^2 \cdot \frac{1}{2} \frac{1 + \mathbf{S}_{x1} \cdot \mathbf{S}_{y2}}{1 + \xi_{xy}^2} \tag{5.17}$$

In the above system of equations (5.6)-(5.9), we have employed the dimensionless length variable $\ell = z / L$, the dimensionless time variable $\tau = t / t_c$, where $t_c = \dfrac{L \cdot n_{avg}}{c}$ is the transit time, n_{avg} is the average index of refraction, and r is the radius of the fiber core. The dimensionless intensity variables are defined as the ratio of powers $Y_{1x}=P_{1x}/P_{1x0}$, $Y_{1y}=P_{1y}/P_{1y0}$, $Y_{2x}=P_{2x}/P_{2x0}$, $Y_{2y}=P_{2y}/P_{2y0}$. Additionally, ε_{1x}, ε_{1y}, ε_{2x}, and ε_{2y} are the dimensionless loss terms, defined as $\varepsilon_{1x} = 2L\alpha_{1x}$, $\varepsilon_{1y} = 2L\alpha_{1y}$, $\varepsilon_{2x} = 2L\alpha_{2x}$, and $\varepsilon_{2y} = 2L\alpha_{2y}$. The form factor component of the β-coefficients is defined as $\xi_{ij} = \frac{\Omega_{Bij} - \Omega_1}{\frac{\Gamma_B}{2}}$, where $i=x,y$, and $j=x,y$. The *Method of Characteristics* was employed [61, 75, 76, 77] and the following change of variables was performed, where the approximation $\overline{n}_1 \approx \overline{n}_2 = \overline{n}$ was used.

$$u = \frac{1}{\overline{n}}\tau + \ell \tag{5.18}$$

$$v = \frac{1}{\overline{n}}\tau - \ell \tag{5.19}$$

The resulting system of equations is as follows, with β-coefficients as defined in expressions (5.10)-(5.17).

$$\frac{dY_{1x}}{du} = -\left[\beta_{1a}Y_{2x} + \beta_{1b}Y_{2y}\right]Y_{1x} - \varepsilon_{1x}Y_{1x} \tag{5.20}$$

$$\frac{dY_{1y}}{du} = -\left[\beta_{1c}Y_{2y} + \beta_{1d}Y_{2x}\right]Y_{1y} - \varepsilon_{1y}Y_{1y} \tag{5.21}$$

$$\frac{dY_{2x}}{dv} = \left[\beta_{3a}Y_{1x} + \beta_{3b}Y_{1y}\right]Y_{2x} - \varepsilon_{2x}Y_{2x} \tag{5.22}$$

$$\frac{dY_{2y}}{dv} = \left[\beta_{3c}Y_{1y} + \beta_{3d}Y_{1x}\right]Y_{2y} - \varepsilon_{2y}Y_{2y} \tag{5.23}$$

The change of variables *u* and *v* transforms the system of equations (5.6)-(5.9) of counter-propagating waves into the system of equations (5.20)-(5.23) of co-propagating waves. Consequently, we are able to set the following initial conditions

$$Y_{ij0}(t,0) = \left[\tanh\left(a_1(t-b_1)\right)\right]\cdot\left[\tanh\left(-a_2(t-b_2)\right)\right] + 1 \tag{5.24}$$

both of which take place at the same end of the new coordinate system, where $i=1,2$, and $j=x,y$. The parameters a_1 and a_2 determine the rise time of the PW and SW pulse profiles, while the parameters b_1 and b_2 define the center of the pulses via the expression $|b_2-b_1|/2$.

Though there exist many numerical methods of solution for SBS equations [75, 78, 79, 80, 81, 82, 83], the fourth order Runge-Kutta method (RK4) was used to numerically solve the system of equations (5.20)-(5.23), and was chosen for its stability and relatively large step size. Details of this numerical method of solution are summarized in the *Appendix*.

5.3. Results and Discussion

Output spectra were calculated by detuning the Stokes frequency, ω_2. Output powers were calculated as $P_{1x\text{-}out} = P_{1x0} \cdot Y_{1x\text{-}out}$, $P_{1y\text{-}out} = P_{1y0} \cdot Y_{1y\text{-}out}$, $P_{2x\text{-}out} = P_{2x0} \cdot Y_{2x\text{-}out}$, and $P_{2y\text{-}out} = P_{2y0} \cdot Y_{2y\text{-}out}$, and the total power of the pump and Stokes waves was calculated to be $P_1 = P_{1x} + P_{1y}$ and $P_2 = P_{2x} + P_{2y}$ respectively. Also, the attenuation in the fiber has been approximated as $\alpha_{1x}=\alpha_{1y}=\alpha_{2x}=\alpha_{2y}=\alpha=0.2$ *dB/km*, and the following parameters of the fiber were used: $n_{avg}=1.45$, $\gamma_e=0.902$, $\lambda=1550nm$, $\rho_0=2.21g/cm^3$, $v=5616m/s$, $\Gamma_B=0.1GHz$.

5.3.1 Spectral Shift

The appearance of a fast and slow axis results in two optical modes in the fiber with different SBS frequency shifts, causing a mismatch in the corresponding momentum vectors of the acoustic waves, thereby making it impossible for both principal axes to be resonant with the acoustic phonons in the conventional sense. The mismatch in phonon resonance causes a Brillouin shift, $\Delta\upsilon_B$, and the larger the birefringence, the larger the Brillouin shift.

Figure 5.2 below shows the magnitude of the Brillouin shift in the output PW and SW spectra.

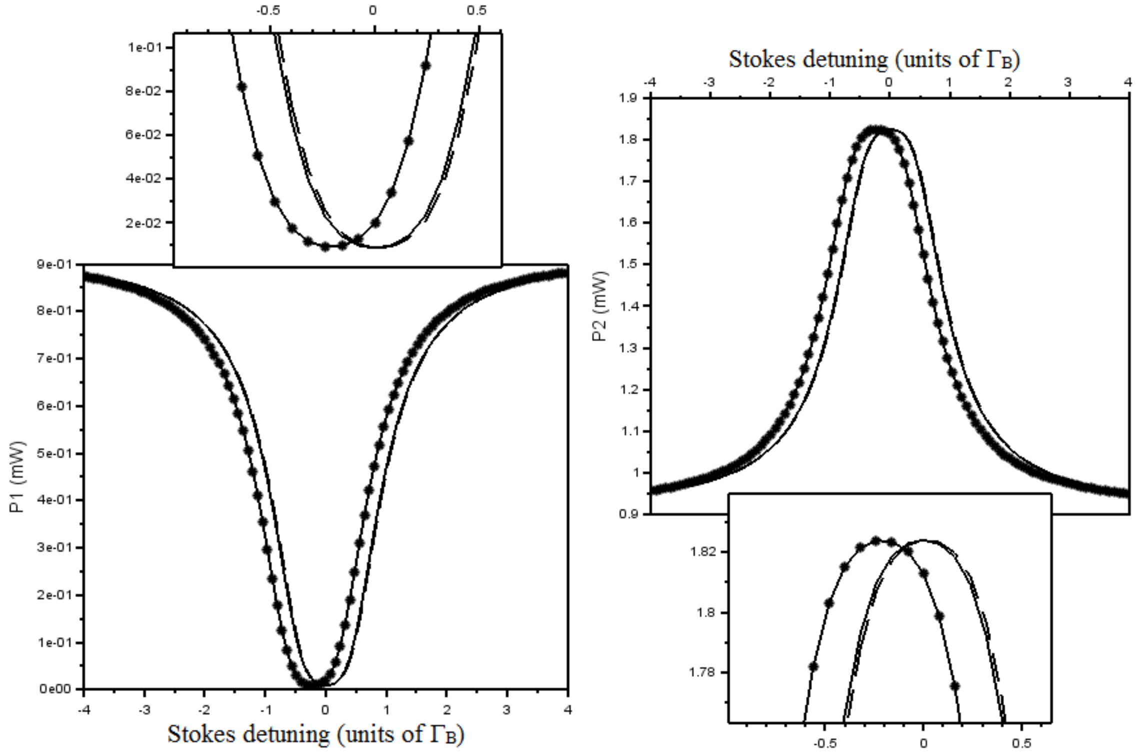

(a) (b)

Figure 5.2 (a) Output pump spectrum, (b) output Stokes spectrum.

Birefringence Δn: *10^{-4}; —— 10^{-5}; - - - 10^{-6}; LHP(1,0,0); L=1000m.

P_{1x0} = 0.5 mW, P_{1y0} = 0.5 mW, P_{2x0} = 0.5 mW, P_{2y0} = 0.5 mW.

The Brillouin shift, $\Delta\upsilon_B$, was measured as a function of beat length, which is defined in expressions (5.25)-(5.26) below [4].

$$L_B = \frac{2\pi}{\left|\left(k_{1x} + k_{2x}\right) - \left(k_{1y} + k_{2y}\right)\right|} \tag{5.25}$$

where $k_{ij} = \frac{n_{ij}}{c}\omega_i$, $i=1,2$ and $j=x,y$. (5.26)

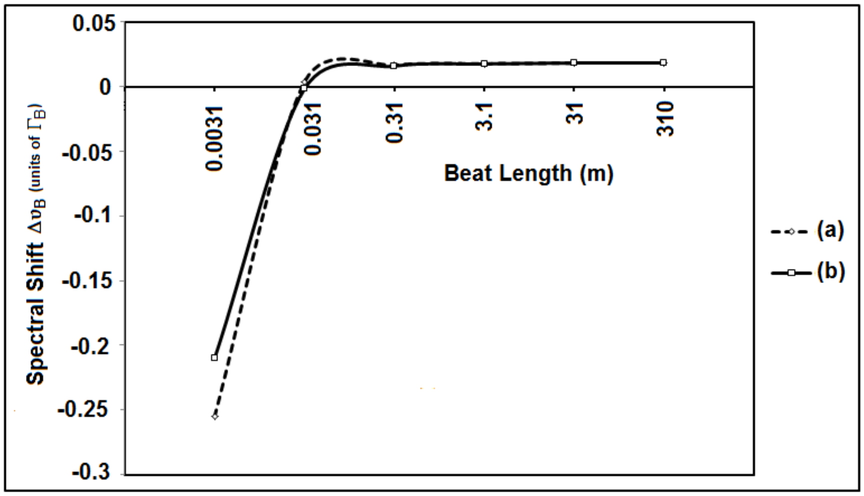

Figure 5.3 Brillouin shift dependence on beat length, *L*=1000m, LHP (1,0,0).
(a) P_{1x0} = 0.9 mW, P_{1y0} = 0.1 mW, P_{2x0} = 0.9 mW, P_{2y0} = 0.1 mW.
(b) P_{1x0} = 0.5 mW, P_{1y0} = 0.5 mW, P_{2x0} = 0.5 mW, P_{2y0} = 0.5 mW.

Figure 5.3 summarizes the simulated values of the $\Delta\upsilon_B$, in comparison to the beat length (and birefringence Δn), for linearly polarized light (LP). Two cases were compared for pump and Stokes input powers of 1 mW: (a) the input powers of the *x*- and *y*- components of the pump and Stokes waves were taken to be unequal, and (b) the input powers of the *x*- and *y*- components of the pump and Stokes waves were taken to be equal. From Figure 5.3, it is apparent that the degree of birefringence has a nonlinear effect on the Brillouin shift $\Delta\upsilon_B$, in particular, the larger the birefringence, the larger the shift. This spectral shift can in turn be used to quantify the birefringence of the optical fiber upon measurement of the output signal. In addition, the spectral shift appears to be more prominent for unequally balanced input powers of the *x*- and *y*- components of the pump and Stokes waves, as compared to the case of equally balanced powers.

5.3.2 Spectral Distortion

A. Linear Polarization (LP)

The following simulations were performed for linearly polarized (LP) light. Figure 5.4 below shows the output spectra of the pump and Stokes waves – both of which were linearly horizontally polarized (LHP) in one simulation, and linearly vertically polarized (LVP) in another, the resulting spectra being identical for both LHP and LVP light.

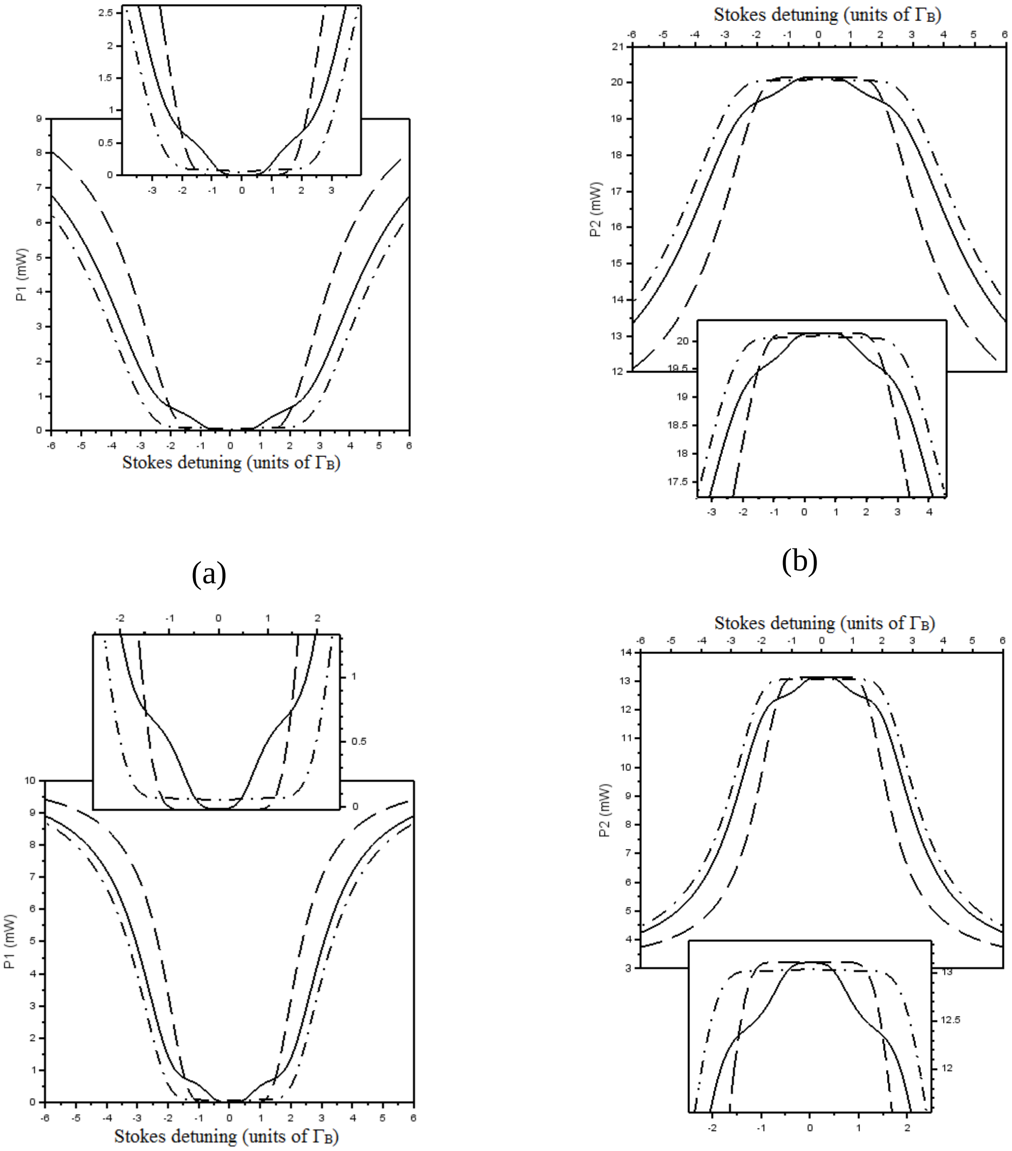

(a) (b)

(c) (d)

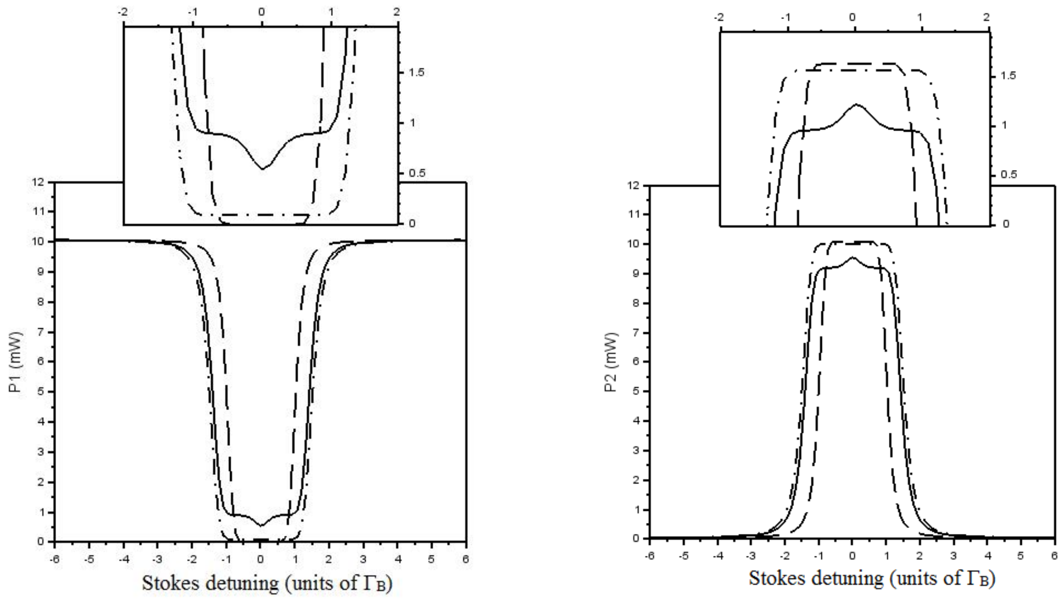

(e) (f)

Figure 5.4 Left: output pump spectrum; Right: output Stokes spectrum.

(a)-(b) steady-state; (c)-(d) 240ns pulse; (e)-(f) 79ns pulse; Birefringence Δn=10^{-4}; L=1 km.

—·—·— : P_{1x0} = 10.0 mW, P_{1y0} = 1.0 mW, P_{2x0} = 10.0 mW, P_{2y0} = 1.0 mW; LHP (1,0,0);

—— : P_{1x0} = 10.9 mW, P_{1y0} = 0.1 mW, P_{2x0} = 10.9 mW, P_{2y0} = 0.1 mW; LHP (1,0,0);

– – – : P_{1x0} = 10.0 mW, P_{1y0} = 1.0 mW, P_{2x0} = 10.0 mW, P_{2y0} = 1.0 mW; no pol (0,0,0).

It is often experimentally not possible to achieve a 100% separation of power between the slow and fast modes of the signal. There is power leakage between the x- and y-axes [84], especially when additional optical components, such a polarization controllers or scramblers [85, 86], are used. Hence, for a 11 mW signal, it is a realistic assumption that as much as 1 mW of power could be present in the vertical mode of the signals for LHP light. Likewise, for LVP lights, it is also experimentally plausible to have as much as 1 mW of power in the horizontal mode.

The shape of the output spectra in Figures 5.4 can be explained by the modified interaction between the pump and Stokes waves during LP. Referring to the system of equations (5.20)-(5.23) and β-coefficients (5.10)-(5.17), we see that the β-coefficients β_{1b}, β_{1d}, β_{3b} and β_{3d} are reduced to zero for both LHP and LVP light. As a result, the system of equations (5.20)-(5.23) is broken up into two smaller systems consisting of equations: a) (5.20) and (5.21), and b)

(5.22) and (5.23) respectively, which are independent of each other. The first system describes the interaction between the horizontal components (*x*-components) of the pump and Stokes waves, and the second system describes the interaction between the vertical components (*y*-components) of the pump and Stokes waves. In other words, interactions along the *x*- and *y*-components become independent from each other, which is to be expected during linear polarization.

In Figure 5.4, which represents the output pump and Stokes spectra of LHP light, the little 'blip' at the bottom/top of the spectra is the *y*-component contribution, while the 'general' shape of the spectra is a result of the *x*-component contribution. Since the power in the horizontal mode is large for LHP light, the resultant depletion of the PW and amplification of the SW are also large, leading to the general trend of the output spectra in Figure 5.4. This is the spectral shape which would be expected for an idealized LHP light (or perhaps light with no consideration for polarization at all). However, the LHP is not ideal, and there exists a small interaction in the vertical component. Since the power along the *y*-axis is small, the resultant contribution is also small. As can be seen from Figure 5.4, the smaller the power in the y-component, the smaller the contribution, and the weaker the spectral distortion of the graph. In other words, increasing powers in the *y*-components have been chosen to demonstrate the increasing degree of spectral distortion. For P_{1y}=P_{2y}=1mW, the spectral 'blip' is much larger than for the case where P_{1y}=P_{2y}=0.1mW. However, while a small power leakage causes a smaller spectral distortion or 'blip', it yields an output spectra with a larger depletion, or 'flat-top', than in the case of larger power leakage. For the steady-state regime, shown in Figures 5.4(a)-(b), where both the pump and Stokes waves are continuous waves, the 'flat-top' effect is more prominent and the spectral 'blip' is less pronounced, as compared to shorter pulse lengths of 240ns and 79ns, shown in Figures 5.4(c)-(d) and 5.4(e)-(f) respectively. With decreasing temporal pulse width, the power leakage causes the distorted spectral tip to be sharper and more pronounced, as compared to longer pulses.

For sensing applications, it is detrimental to have a depleted spectrum [70, 71, 72], since depletion and spectral flattening makes it difficult to accurately measure the center frequency of the spectrum. Although the distorted spectra with smaller depletion, obtained from the steady-state interaction of the PW and SW, may not have a sufficiently prominent spectral tip for sensing applications, it is an improvement none-the-less, as compared to the case of larger depletion, where the 'flat-top' spans an even larger frequency range.

As shown in Figure 5.4(e)-(f), a shorter pulse length of 79ns undergoing spectral leakage between the fast and slow modes has a sufficiently prominent spectral tip for measurement in sensing applications. As such, by using the distortion effects caused by birefringence to our advantage, it is possible to provide a regime that is favourable for sensing applications related to SBS, by increasing the power leakage between the fast and slow modes, as well as decreasing the pulse length during LP.

In the case of LVP, also shown in Figure 5.4, the roles of the *x*- and *y*-components are reversed, but the interaction is identical. For this reason, the two cases of LHP and LVP light, shown in Figures 5.4, give identical results, since in either case, the interaction along the slow or fast axes remains the same.

Also shown in the Figure 5.4, the output spectra of LP light is shown in comparison to light without a dependence on polarization – namely light having a Stokes vector $\boldsymbol{S}=(0,0,0)$, which has been taken to be a first-order approximation to truly unpolarized light. The spectra of the LP is spread out in the frequency domain, as compared to non-polarized light. This effect can be explained by the nature of the LP interaction between the pump and Stokes waves. As discussed above, when LP is not ideal, there exists a small independent interaction along either the fast or slow mode, contributing to the spectral distortion. The interaction along the main axis of polarization, however, contributes the most to the output spectral shape of the light – the SOP of the counter-propagating waves being lined up for maximum gain [22, 24, 25, 27, 29, 30]. Additionally, since this interaction is strong, and the input powers along the main mode are comparatively large, the output light experiences a significant gain/depletion, causing the spectrum itself to be larger and inherently spread out [72]. This effect does not present itself for unpolarized light, where there cannot be polarization alignment for maximum gain. All four lights interact with each other and as a result, the output spectrum is smaller, which contributes to less spectral spreading in the frequency domain.

As a result, the model presented for LP light proves to be a valuable measure of the experimentally realistic case of non-ideally linearly polarized light in optical fibers, or as a measure of power leakage between the fast and slow modes. The degree of spectral distortion may be used as an indication of the quality of LP during the SBS interaction.

B. Elliptical Polarization for steady-state interaction

In this section, the pump and Stokes waves were simulated to have several elliptical polarizations: *Random1 (0.1, 0.9, 0.42)*, *Random2 (0.3, 0.7, 0.65)*, *Random3 (0.58, 0.58, 0.58)*, and *Random4 (0.1, 0.9, 0.42)*. The effect of the elliptical polarization on the spectral shape of the output light was observed for pump and Stokes input powers: a) below the Brillouin threshold, and b) above the Brillouin threshold [1, 61].

In the Figure 5.5 below, the individual *x*- and *y*- components of the Stokes wave have been plotted. Moderate powers have been chosen for various degrees of birefringence: 10^{-4}, 10^{-5}, and 10^{-6}. It can be seen that the spectral distortion which results due to the birefringence is more prominent for higher degrees of birefringence (10^{-4}) as compared to lower degrees of birefringence (10^{-6}).

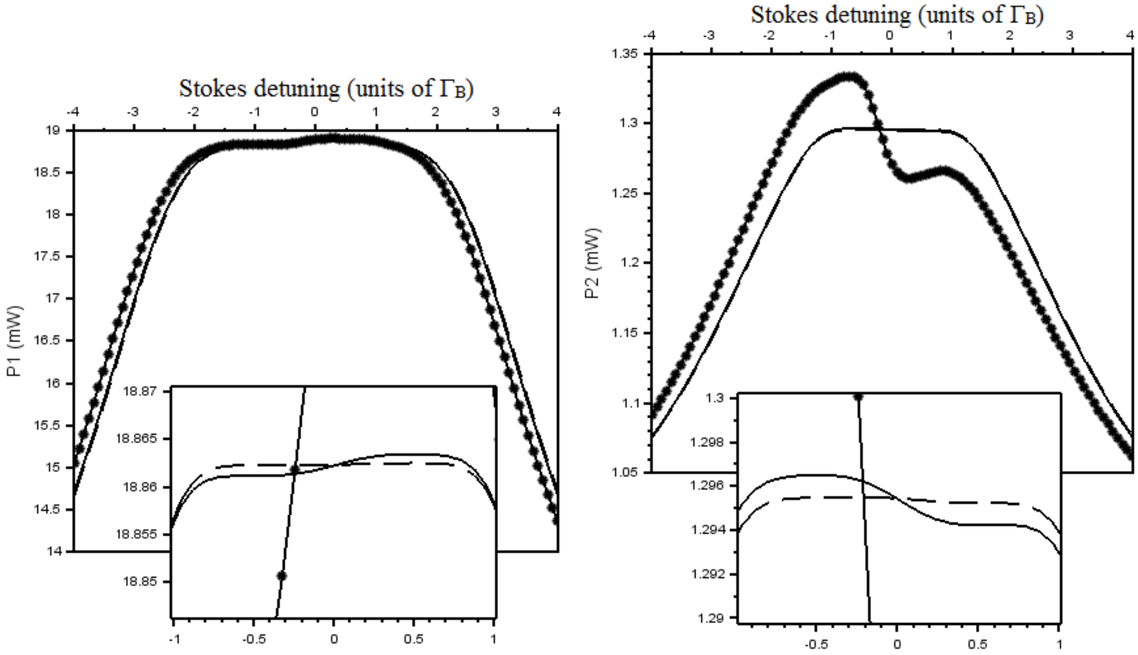

(a) (b)

Figure 5.5 (a) x-comp. of output Stokes spectrum; (b) y-comp. of output Stokes spectrum. Birefringence Δn = * 10^{-4} ; — 10^{-5}; - - - 10^{-6}; Random4 (0.1,0.9,0.42), L=1000m. P_{1x0} = 10.0 mW, P_{1y0} = 1.0 mW, P_{2x0} = 10.0 mW, P_{2y0} = 1.0 mW.

In the most general case of elliptical birefringence, there are four running acoustic waves, each having their own resonance frequency. As a result, each of the fast and slow modes have their own resonant frequency, which is the cause of the multiple peaks on the output spectra in Figure 5.5.

In Figures 5.6-5.7 below, input powers have been taken beyond the Brillouin threshold for various elliptical polarizations. It can be seen that certain polarizations cause a kind of spectral spreading effect [87, 88], to the extent that the two spectra become partially disjoint, while others affect the spectral shape negligibly.

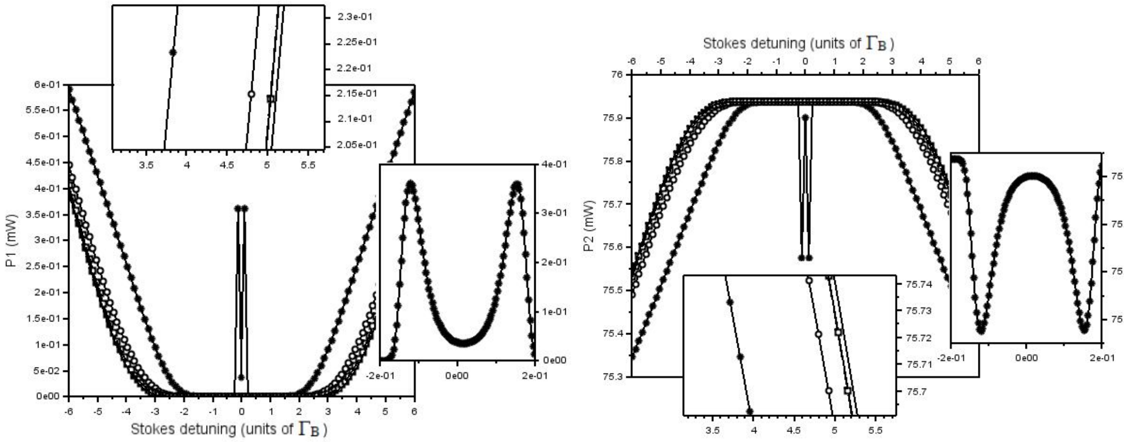

(a) (b)

Figure 5.6 (a) Output pump spectrum, (b) Output Stokes spectrum.

Birefringence Δn: □ 10^{-6} *Random1 (0.6, 0.25, 0.76)*; - - - 10^{-6} *Random2 (0.3, 0.7, 0.65)*; *L*=1000m
○ 10^{-6} *Random3 (0.58, 0.58, 0.58)*; * 10^{-6} *Random4 (0.1, 0.9,0.42)*; —— 10^{-10} no pol (0,0,0);
P_{1x0} = 1.0 mW, P_{1y0} = 1.0 mW, P_{2x0} = 1.0 mW, P_{2y0} = 80.0 mW.

In Figure 5.6, for example, the spectral spreading effect can be explained as a result of a very strong interaction along one mode of the optical fiber, and weak interactions along the other modes for the polarization *Random4 (0.1, 0.9, 0.42)*. In Figure 5.6, since the input power of the Stokes *y*-component is so large (80mW), and the corresponding linear polarization component is also large, it acts to quickly deplete power from the other modes, and since, as mentioned before, there is no single resonant frequency, it does so along multiple resonant frequencies. For polarizations *Random1 (0.6, 0.25, 0.76)*, *Random2 (0.3, 0.7, 0.65)* and *Random3 (0.3, 0.7, 0.65)*, the combination of relatively weak vertical polarization component and strong circular polarization component almost eliminate the effect altogether. Polarizations *Random1* and *Random2* are nearly identical to the non-polarized light, hence these polarizations can be used to maintain the fidelity of the spectral shape to be as close as possible to non-polarized light which is unaffected by birefringence. Additionally, the effects of distortion on the full width at half maximum (*FWHM*) of the output pulse can be minimized, which has numerous applications in communications and data transmission.

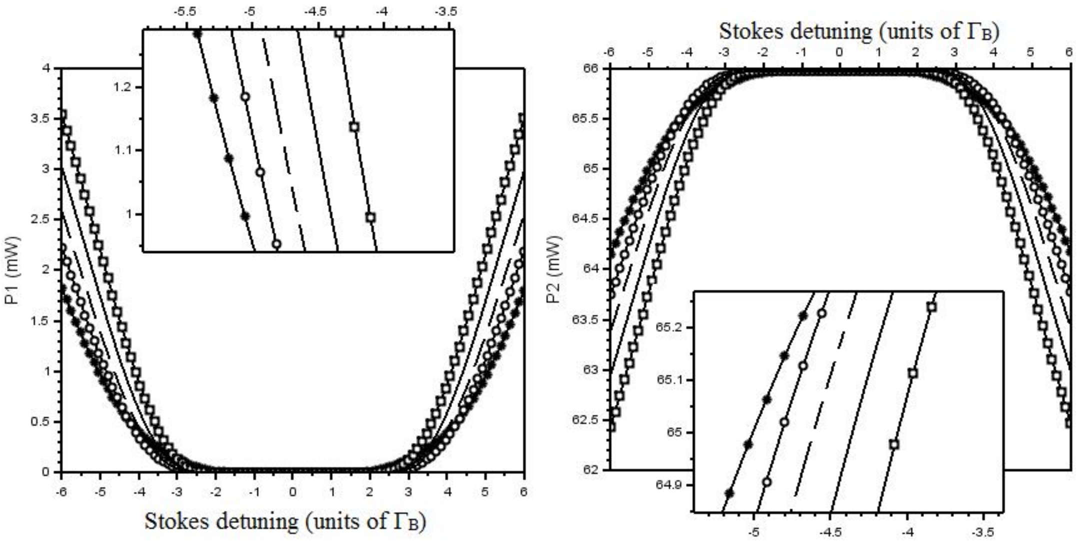

(a) (b)

Figure 5.7 (a) Output pump spectrum, (b) output Stokes spectrum.
Birefringence Δn: □ 10^{-6} *Random1 (0.6, 0.25, 0.76)*; --- 10^{-6} *Random2 (0.3, 0.7, 0.65)*; *L*=1000m
○ 10^{-6} *Random3 (0.58, 0.58, 0.58)*; * 10^{-6} *Random4 (0.1, 0.9,0.42)*; — 10^{-10} no pol (0,0,0);
P_{1x0} = 10.0 mW, P_{1y0} = 1.0 mW, P_{2x0} = 60.0 mW, P_{2y0} = 1.0 mW.

A similar effect can be observed in Figure 5.7 above, though because of the different power distribution among the modes there is no longer a spectral spreading effect. In addition, polarizations *Random1*, *Random2* and *Random3* are no longer nearly identical to the unpolarized light, due to the different interaction between the four lights caused by varied initial power distributions.

As a result, it is shown that elliptical birefringence has a prominent effect on the spectral shape of the output pump and Stokes waves. In some cases, it causes a spectral spreading effect as well as spectral spreading, while in other cases it is possible to choose a polarization and power combination to minimize the spectral distortion of the *FWHM* of the output pulse, and maintain pulse fidelity.

5.4 Summary

In summary, it has been observed that the degree of birefringence, or beat length, is responsible for an observed Brillouin shift, $\Delta\upsilon_B$, in the output PW and SW spectra, which may be used to quantify the birefringence of the fiber. Polarization and elliptical birefringence has a prominent effect on the spectral shape of output light – in particular, non-ideal LP light causes spectral distortion, which appears in the shape of a 'blip' on top of the expected spectral shape, as well as spreading of the spectrum in the frequency domain. As such, a good measure for detecting non-ideally linearly polarized light has been established. Additionally, the spectral depletion of the non-ideally linearly polarized light has uncovered a regime which is preferable for measurement in sensing applications. Elliptical polarization, for moderate input powers of the PW and SW, also causes the spectrum to spread out in the frequency domain. For high input powers, a spectral spreading effect is observed for certain elliptical polarizations. Other elliptical polarizations provide means for maintaining the *FWHM* and pulse fidelity of the Brillouin spectral shape – even for powers beyond the Brillouin threshold.

Chapter 6

Polarization Effects in combined Brillouin gain and loss

6.1 Introduction

In this chapter, a more accurate model of the polarization-dependent Brillouin gain and loss interaction, which includes the case of elliptical birefringence, is provided. The model presented in this manuscript describes the most comprehensive equations considering the birefringence effects in an optical fiber, being an extension of the work presented in Chapter 5. As in Chapter 5, the model includes the most general case of elliptical birefringence, the effects of polarization mode dispersion (PMD), polarization dependent loss (PDL), phonon resonance structures, pulse length, as well as the overall attenuation of the fiber.

For sensing applications involving optical differential parametric amplification in Brillouin optical time domain analysis (ODPA-BOTDA) systems [65, 89], which employ both Stokes wave (SW) and anti-Stokes wave (ASW) pulses, this investigation of the effects of birefringence on the combined Brillouin gain and loss is paramount. Additionally, since spectral distortion is detrimental in sensing applications, it is important to investigate a power regime in which birefringence effects are minimal.

6.2 Model

The process of Brillouin gain and loss has been studied in a birefringent optical fiber, with a core radius of 4.1μm. The configuration is comprised of a pump wave (PW) launched into one end, and a Stokes wave (SW) and an anti-Stokes wave (ASW) launched from the other end. The PW, SW and ASW have *x*- and *y*- eigen-polarization components. The schematic arrangement is shown in Figure 6.1 below.

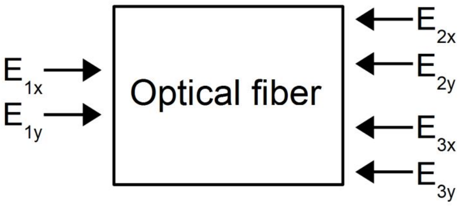

Figure 6.1 Schematic arrangement of SBS in an optical fiber of length *L*.
E_{1x} – Pump wave, E_{1y} – Pump wave, E_{2x} – Stokes wave, E_{2y} – Stokes wave, E_{3x} – anti-Stokes wave, E_{3y} – anti-Stokes wave

The extended system of equations (1.1)-(1.6) describes the interaction of the pump, SW and ASW, as shown in Figure 6.1, including the effects of PMD and PDL, similar to the system presented in section 5.2. Again, besides the usual slowly varying amplitude approximation, the only additional approximation employed was the assumption that the phonon fields are established almost simultaneously [1, 30].

$$\begin{aligned}
&\frac{\partial E_{1x}}{\partial z}+\frac{\bar{n}_1}{c}\frac{\partial E_{1x}}{\partial t}+\left(\bar{\alpha}_1+\frac{\Delta\bar{\alpha}_1}{2}+i\frac{\Delta\bar{n}_1\omega_1}{2c}\right)E_{1x}\\
&\qquad\left.\begin{aligned}
&=i\frac{\gamma_e^2\omega_1^2}{2\rho_0c^2v}\frac{1}{\left(\Omega_{Bxx}^{SW}-\Omega_1\right)-i\frac{\Gamma_B}{2}}E_{1x}E_{2x}^*E_{2x}\frac{1}{2}\left(1+\mathbf{S}_{x1}\cdot\mathbf{S}_{x2}\right)\\
&+i\frac{\gamma_e^2\omega_1^2}{2\rho_0c^2v}\frac{1}{\left(\Omega_{Bxy}^{SW}-\Omega_1\right)-i\frac{\Gamma_B}{2}}E_{1x}E_{2y}^*E_{2y}\frac{1}{2}\left(1+\mathbf{S}_{x1}\cdot\mathbf{S}_{y2}\right)
\end{aligned}\right\}Stokes\\
&\qquad\left.\begin{aligned}
&+i\frac{\gamma_e^2\omega_1^2}{2\rho_0c^2v}\frac{1}{\left(\Omega_{Bxx}^{ASW}-\Omega_2\right)-i\frac{\Gamma_B}{2}}E_{1x}E_{3x}^*E_{3x}\frac{1}{2}\left(1+\mathbf{S}_{x1}\cdot\mathbf{S}_{x3}\right)\\
&+i\frac{\gamma_e^2\omega_1^2}{2\rho_0c^2v}\frac{1}{\left(\Omega_{Bxy}^{ASW}-\Omega_2\right)-i\frac{\Gamma_B}{2}}E_{1x}E_{3y}^*E_{3y}\frac{1}{2}\left(1+\mathbf{S}_{x1}\cdot\mathbf{S}_{y3}\right)
\end{aligned}\right\}anti-Stokes
\end{aligned}\tag{6.1}$$

$$
\begin{aligned}
&\frac{\partial E_{1y}}{\partial z}+\frac{\overline{n}_1}{c}\frac{\partial E_{1y}}{\partial t}+\left(\overline{\alpha}_1-\frac{\Delta\overline{\alpha}_1}{2}-i\,\frac{\Delta\overline{n}_1\omega_1}{2c}\right)E_{1y}\\
&\qquad \left.\begin{aligned}
&=i\,\frac{\gamma_e^2\omega_1^2}{2\rho_0 c^2 v}\frac{1}{\left(\Omega_{Byy}^{SW}-\Omega_1\right)-i\,\frac{\Gamma_B}{2}}E_{1y}E_{2y}^{*}E_{2y}\,\frac{1}{2}\left(1+\mathbf{S}_{y1}\cdot\mathbf{S}_{y2}\right)\\
&+i\,\frac{\gamma_e^2\omega_1^2}{2\rho_0 c^2 v}\frac{1}{\left(\Omega_{Byx}^{SW}-\Omega_1\right)-i\,\frac{\Gamma_B}{2}}E_{1y}E_{2x}^{*}E_{2x}\,\frac{1}{2}\left(1+\mathbf{S}_{y1}\cdot\mathbf{S}_{x2}\right)
\end{aligned}\right\}\mathit{Stokes}\\
&\qquad \left.\begin{aligned}
&+i\,\frac{\gamma_e^2\omega_1^2}{2\rho_0 c^2 v}\frac{1}{\left(\Omega_{Byy}^{ASW}-\Omega_2\right)-i\,\frac{\Gamma_B}{2}}E_{1y}E_{3y}^{*}E_{3y}\,\frac{1}{2}\left(1+\mathbf{S}_{y1}\cdot\mathbf{S}_{y3}\right)\\
&+i\,\frac{\gamma_e^2\omega_1^2}{2\rho_0 c^2 v}\frac{1}{\left(\Omega_{Byx}^{ASW}-\Omega_2\right)-i\,\frac{\Gamma_B}{2}}E_{1y}E_{3x}^{*}E_{3x}\,\frac{1}{2}\left(1+\mathbf{S}_{y1}\cdot\mathbf{S}_{x3}\right)
\end{aligned}\right\}\mathit{anti-Stokes}
\end{aligned}
\tag{6.2}
$$

$$
\begin{aligned}
&-\frac{\partial E_{2x}}{\partial z}+\frac{\overline{n}_2}{c}\frac{\partial E_{2x}}{\partial t}+\left(\overline{\alpha}_2+\frac{\Delta\overline{\alpha}_2}{2}+i\,\frac{\Delta\overline{n}_2\omega_2}{2c}\right)E_{2x}\\
&\qquad =i\,\frac{\gamma_e^2\omega_2^2}{2\rho_0 c^2 v}\frac{1}{\left(\Omega_{Bxx}^{SW}-\Omega_1\right)-i\,\frac{\Gamma_B}{2}}E_{2x}E_{1x}^{*}E_{1x}\,\frac{1}{2}\left(1+\mathbf{S}_{x1}\cdot\mathbf{S}_{x2}\right)\\
&\qquad +i\,\frac{\gamma_e^2\omega_2^2}{2\rho_0 c^2 v}\frac{1}{\left(\Omega_{Byx}^{SW}-\Omega_1\right)-i\,\frac{\Gamma_B}{2}}E_{2x}E_{1y}^{*}E_{1y}\,\frac{1}{2}\left(1+\mathbf{S}_{y1}\cdot\mathbf{S}_{x2}\right)
\end{aligned}
\tag{6.3}
$$

$$
\begin{aligned}
&-\frac{\partial E_{2y}}{\partial z}+\frac{\overline{n}_2}{c}\frac{\partial E_{2y}}{\partial t}+\left(\overline{\alpha}_2-\frac{\Delta\overline{\alpha}_2}{2}-i\,\frac{\Delta\overline{n}_2\omega_2}{2c}\right)E_{2y}\\
&\qquad =i\,\frac{\gamma_e^2\omega_2^2}{2\rho_0 c^2 v}\frac{1}{\left(\Omega_{Byy}^{SW}-\Omega_1\right)-i\,\frac{\Gamma_B}{2}}E_{2y}E_{1y}^{*}E_{1y}\,\frac{1}{2}\left(1+\mathbf{S}_{y1}\cdot\mathbf{S}_{y2}\right)\\
&\qquad +i\,\frac{\gamma_e^2\omega_2^2}{2\rho_0 c^2 v}\frac{1}{\left(\Omega_{Bxy}^{SW}-\Omega_1\right)-i\,\frac{\Gamma_B}{2}}E_{2y}E_{1x}^{*}E_{1x}\,\frac{1}{2}\left(1+\mathbf{S}_{x1}\cdot\mathbf{S}_{y2}\right)
\end{aligned}
\tag{6.4}
$$

$$
\begin{aligned}
-\frac{\partial E_{3x}}{\partial z}+\frac{\overline{n}_3}{c}\frac{\partial E_{3x}}{\partial t}+\left(\overline{\alpha}_3+\frac{\Delta\overline{\alpha}_3}{2}+i\,\frac{\Delta\overline{n}_3\omega_3}{2c}\right)E_{3x}& \\
=i\,\frac{\gamma_e^2\omega_3^2}{2\rho_0c^2v}\frac{1}{\left(\Omega_{Bxx}^{ASW}-\Omega_2\right)-i\,\frac{\Gamma_B}{2}}E_{3x}E_{1x}^{*}E_{1x}\,\frac{1}{2}\left(1+\mathbf{S}_{x1}\cdot\mathbf{S}_{x3}\right)& \\
+i\,\frac{\gamma_e^2\omega_2^2}{2\rho_0c^2v}\frac{1}{\left(\Omega_{Byx}^{ASW}-\Omega_2\right)-i\,\frac{\Gamma_B}{2}}E_{3x}E_{1y}^{*}E_{1y}\,\frac{1}{2}\left(1+\mathbf{S}_{y1}\cdot\mathbf{S}_{x3}\right)&
\end{aligned}
\tag{6.5}
$$

$$
\begin{aligned}
-\frac{\partial E_{3y}}{\partial z}+\frac{\overline{n}_3}{c}\frac{\partial E_{3y}}{\partial t}+\left(\overline{\alpha}_3-\frac{\Delta\overline{\alpha}_3}{2}-i\,\frac{\Delta\overline{n}_3\omega_3}{2c}\right)E_{3y}& \\
=i\,\frac{\gamma_e^2\omega_3^2}{2\rho_0c^2v}\frac{1}{\left(\Omega_{Byy}^{ASW}-\Omega_2\right)-i\,\frac{\Gamma_B}{2}}E_{3y}E_{1y}^{*}E_{1y}\,\frac{1}{2}\left(1+\mathbf{S}_{y1}\cdot\mathbf{S}_{y3}\right)& \\
+i\,\frac{\gamma_e^2\omega_2^2}{2\rho_0c^2v}\frac{1}{\left(\Omega_{Bxy}^{ASW}-\Omega_2\right)-i\,\frac{\Gamma_B}{2}}E_{3y}E_{1x}^{*}E_{1x}\,\frac{1}{2}\left(1+\mathbf{S}_{x1}\cdot\mathbf{S}_{y3}\right)&
\end{aligned}
\tag{6.6}
$$

For the Stokes wave, we have $\Omega_{Bxx}^{SW}=\frac{v}{c}\left(n_{1x}\omega_1+n_{2x}\omega_2\right)$, $\Omega_{Byy}^{SW}=\frac{v}{c}\left(n_{1y}\omega_1+n_{2y}\omega_2\right)$, $\Omega_{Bxy}^{SW}=\frac{v}{c}\left(n_{1x}\omega_1+n_{2y}\omega_2\right)$, $\Omega_{Byx}^{SW}=\frac{v}{c}\left(n_{1y}\omega_1+n_{2x}\omega_2\right)$, and for the anti-Stokes wave we have $\Omega_{Bxx}^{ASW}=\frac{v}{c}\left(n_{1x}\omega_1+n_{3x}\omega_3\right)$, $\Omega_{Byy}^{ASW}=\frac{v}{c}\left(n_{1y}\omega_1+n_{3y}\omega_3\right)$, $\Omega_{Bxy}^{ASW}=\frac{v}{c}\left(n_{1x}\omega_1+n_{3y}\omega_3\right)$, $\Omega_{Byx}^{ASW}=\frac{v}{c}\left(n_{1y}\omega_1+n_{3x}\omega_3\right)$, which are the Brillouin frequencies associated with the principal axis beatings [4], where ω_1 is the angular frequency of the PW, and ω_2 and ω_3 are the angular frequencies of the SW and ASW respectively. n_{1x} and n_{1y}, n_{2x} and n_{2y}, and n_{3x} and n_{3y}, are the indices of refraction associated with the principal axes of the PW, SW and ASW respectively. $\Omega_1=\omega_1-\omega_2$ is the angular frequency of the AW$_1$ caused by the interaction of the PW and SW, and $\Omega_2=\omega_3-\omega_1$ is the angular frequency of the AW$_2$ caused by the interaction of the PW and ASW. E_{1x} and E_{1y}, E_{2x} and E_{2y}, and E_{3x} and E_{3y}, are the complex amplitudes of the PW, SW and the ASW, respectively. c is the speed of light, ρ_0 is the mean density of the fiber, γ_e is the electrostrictive constant, z is the coordinate along the fiber, v is the speed of sound in the fiber, Γ_B is the Brillouin linewidth, and finally, α_{1x}, α_{1y}, α_{2x}, α_{2y}, α_{3x}, and α_{3y} represent the fiber attenuations of the principal axes of polarization of the three interacting waves.

The $\boldsymbol{S}_{1x}$, $\boldsymbol{S}_{1y}$, $\boldsymbol{S}_{2x}$, $\boldsymbol{S}_{2y}$, $\boldsymbol{S}_{3x}$, and $\boldsymbol{S}_{3y}$ represent the Stokes vectors in the Poincaré sphere polarization representation [66, 67], and are used to define the polarization of the propagating lights [61, 66, 67]. As defined in section 5.2, relations of importance include: $\boldsymbol{S}_{x1} = -\boldsymbol{S}_{y1}$, $\boldsymbol{S}_{x2} = -\boldsymbol{S}_{y2}$ and $\boldsymbol{S}_{x3} = -\boldsymbol{S}_{y3}$. In the above system of equations (6.1)-(6.6), $\boldsymbol{S}_{x1}$ describes the principal state of polarization vector for the forward propagating light, and $\boldsymbol{S}_{x2}$ and $\boldsymbol{S}_{x3}$ describe the principal states of the polarization vector of the backward propagating lights. In this case, if $\boldsymbol{S}_{x1}$ is defined as $\boldsymbol{S}_{x1} = (a, b, c)$, then $\boldsymbol{S}_{y1} = (-a, -b, -c)$, $\boldsymbol{S}_{x2} = (a, b, -c)$, $\boldsymbol{S}_{y2} = (-a, -b, c)$, $\boldsymbol{S}_{x3} = (a, b, -c)$ and $\boldsymbol{S}_{y3} = (-a, -b, c)$, where a, b and c are the Stokes vector components normalized such that $a^2 + b^2 + c^2 = 1$. For fibers having elliptical birefringence ($0 < |c| < 1$), the most general beating situation will be excited.

Lastly, the remaining simplifications were introduced to the system of equations (6.1)-(6.6) to make the birefringence effect more explicit, $\overline{n}_i = \dfrac{n_{ix} + n_{iy}}{2}$, $\Delta\overline{n}_i = n_{ix} - n_{iy}$, $\overline{\alpha}_i = \dfrac{\alpha_{ix} + \alpha_{iy}}{2}$, $\Delta\overline{\alpha}_i = \alpha_{ix} - \alpha_{iy}$, $i=1,2,3$.

In the above arrangement, the PW input parameters are known only at the beginning of the fiber, i.e. at z=0. Correspondingly, the SW and ASW input parameters are known only at the end of the fiber, i.e. at $z=L$, where L is the length of the fiber. Therefore, the boundary conditions for the system of equations (1.1)-(1.6) are similar to previously-studied configurations with one pulse [4, 9] from section 5.2. The conditions for two pulses are as follows

$$|E_{1x}(0)|^2=E^2_{1x0};\ |E_{1y}(0)|^2=E^2_{1y0} \tag{6.7}$$

$$|E_{2x}(L)|^2=E^2_{2x0};\ |E_{2y}(L)|^2=E^2_{2y0} \tag{6.8}$$

$$|E_{3x}(L)|^2=E^2_{3x0};\ |E_{3y}(L)|^2=E^2_{3y0} \tag{6.9}$$

where E^2_{1x0} , E^2_{1y0} , E^2_{2x0} , E^2_{2Y0} , E^2_{3x0} , and E^2_{3y0} are the known squared absolute values of the complex fields E_{1x} , E_{1y} , E_{2x} , E_{2y} , E_{3x} , and E_{3y} respectively. The same method was used to simplify the system of equations (6.1)-(6.6) as in section 5.2, namely we have employed the dimensionless length variable $\ell = z/L$, and the dimensionless time variable $\tau = t/t_c$, where $t_c = \frac{L \cdot n_{avg}}{c}$ is the transit time, *n_{avg}* is the average index of refraction, and *r* is the radius of the fiber core. The dimensionless intensity variables are defined as the ratio of powers $Y_{ij}=P_{ij}/P_{ij0}$, *i=1,2,3, j=x,y*. Additionally, ε_{1x}, ε_{1y}, ε_{2x}, ε_{2y}, ε_{3x}, and ε_{3y} are the dimensionless loss terms, defined as $\varepsilon_{ij} = 2L\alpha_{ij}$, *i=1,2,3, j=x,y*. The form factor component of the β-coefficients is defined as $\xi_{ij}^{SW} = \frac{\Omega_{Bij} - \Omega_1}{\frac{\Gamma_B}{2}}$ or $\xi_{ij}^{ASW} = \frac{\Omega_{Bij} - \Omega_2}{\frac{\Gamma_B}{2}}$, where *i=x,y, j=x,y*. Similarly, the Method of Characteristics [61, 75, 76] was employed as in section 5.2, and the following change of variables was used $u = \frac{1}{\overline{n}}\tau + \ell$ and $v = \frac{1}{\overline{n}}\tau - \ell$, where the approximation $\overline{n}_1 \approx \overline{n}_2 = \overline{n}$ was employed. The resulting system of equations is as follows, with β-coefficients as defined in expressions (6.16)-(6.31).

$$\frac{dY_{1x}}{du} = -\underbrace{\left[\beta_{1a}Y_{2x} + \beta_{1b}Y_{2y}\right]Y_{1x}}_{Stokes} + \underbrace{\left[\beta_{2a}Y_{3x} + \beta_{2b}Y_{3y}\right]Y_{1x}}_{anti-Stokes} - \varepsilon_{1x}Y_{1x} \tag{6.10}$$

$$\frac{dY_{1y}}{du} = -\underbrace{\left[\beta_{1c}Y_{2y} + \beta_{1d}Y_{2x}\right]Y_{1y}}_{Stokes} + \underbrace{\left[\beta_{2c}Y_{3y} + \beta_{2d}Y_{3x}\right]Y_{1y}}_{anti-Stokes} - \varepsilon_{1y}Y_{1y} \tag{6.11}$$

$$\frac{dY_{2x}}{dv} = \left[\beta_{3a}Y_{1x} + \beta_{3b}Y_{1y}\right]Y_{2x} - \varepsilon_{2x}Y_{2x} \tag{6.12}$$

$$\frac{dY_{2y}}{dv} = \left[\beta_{3c}Y_{1y} + \beta_{3d}Y_{1x}\right]Y_{2y} - \varepsilon_{2y}Y_{2y} \tag{6.13}$$

$$\frac{dY_{3x}}{dv} = -\left[\beta_{4a}Y_{1x} + \beta_{4b}Y_{1y}\right]Y_{3x} - \varepsilon_{3x}Y_{3x} \tag{6.14}$$

$$\frac{dY_{3y}}{dv} = -\left[\beta_{4c}Y_{1y} + \beta_{4d}Y_{1x}\right]Y_{3y} - \varepsilon_{3y}Y_{3y} \tag{6.15}$$

$$\beta_{1a} = \frac{4\gamma_e^2 k^2 P_{2x0} L}{r^2 \overline{n}_2 \rho_0 c v \Gamma_B} \cdot \frac{1}{2} \frac{1 + \mathbf{S}_{x1} \cdot \mathbf{S}_{x2}}{1 + \left(\xi_{xx}^{SW}\right)^2} \tag{6.16}$$

$$\beta_{2a} = \frac{4\gamma_e^2 k^2 P_{3x0} L}{r^2 \overline{n}_3 \rho_0 c v \Gamma_B} \cdot \frac{1}{2} \frac{1 + \mathbf{S}_{x1} \cdot \mathbf{S}_{x3}}{1 + \left(\xi_{xx}^{ASW}\right)^2} \tag{6.20}$$

$$\beta_{1b} = \frac{4\gamma_e^2 k^2 P_{2y0} L}{r^2 \overline{n}_2 \rho_0 c v \Gamma_B} \cdot \frac{1}{2} \frac{1 + \mathbf{S}_{x1} \cdot \mathbf{S}_{y2}}{1 + \left(\xi_{xy}^{SW}\right)^2} \tag{6.17}$$

$$\beta_{1c} = \frac{4\gamma_e^2 k^2 P_{2y0} L}{r^2 \overline{n}_2 \rho_0 c v \Gamma_B} \cdot \frac{1}{2} \frac{1 + \mathbf{S}_{y1} \cdot \mathbf{S}_{y2}}{1 + \left(\xi_{yy}^{SW}\right)^2} \tag{6.18}$$

$$\beta_{1d} = \frac{4\gamma_e^2 k^2 P_{2x0} L}{r^2 \overline{n}_2 \rho_0 c v \Gamma_B} \cdot \frac{1}{2} \frac{1 + \mathbf{S}_{y1} \cdot \mathbf{S}_{x2}}{1 + \left(\xi_{yx}^{SW}\right)^2} \tag{6.19}$$

$$\beta_{3a} = \frac{4\gamma_e^2 k^2 P_{1x0} L}{r^2 \overline{n}_1 \rho_0 c v \Gamma_B} \left(\frac{\omega_2}{\omega_1}\right)^2 \cdot \frac{1}{2} \frac{1 + \mathbf{S}_{x1} \cdot \mathbf{S}_{x2}}{1 + \left(\xi_{xx}^{SW}\right)^2} \tag{6.24}$$

$$\beta_{3b} = \frac{4\gamma_e^2 k^2 P_{1y0} L}{r^2 \overline{n}_1 \rho_0 c v \Gamma_B} \left(\frac{\omega_2}{\omega_1}\right)^2 \cdot \frac{1}{2} \frac{1 + \mathbf{S}_{y1} \cdot \mathbf{S}_{x2}}{1 + \left(\xi_{yx}^{SW}\right)^2} \tag{6.25}$$

$$\beta_{3c} = \frac{4\gamma_e^2 k^2 P_{1y0} L}{r^2 \overline{n}_1 \rho_0 c v \Gamma_B} \left(\frac{\omega_2}{\omega_1}\right)^2 \cdot \frac{1}{2} \frac{1 + \mathbf{S}_{y1} \cdot \mathbf{S}_{y2}}{1 + \left(\xi_{yy}^{SW}\right)^2} \tag{6.26}$$

$$\beta_{3d} = \frac{4\gamma_e^2 k^2 P_{1x0} L}{r^2 \overline{n}_1 \rho_0 c v \Gamma_B} \left(\frac{\omega_2}{\omega_1}\right)^2 \cdot \frac{1}{2} \frac{1 + \mathbf{S}_{x1} \cdot \mathbf{S}_{y2}}{1 + \left(\xi_{xy}^{SW}\right)^2} \tag{6.27}$$

$$\beta_{2b} = \frac{4\gamma_e^2 k^2 P_{3y0} L}{r^2 \overline{n}_3 \rho_0 c v \Gamma_B} \cdot \frac{1}{2} \frac{1 + \mathbf{S}_{x1} \cdot \mathbf{S}_{y3}}{1 + \left(\xi_{xy}^{ASW}\right)^2} \tag{6.21}$$

$$\beta_{2c} = \frac{4\gamma_e^2 k^2 P_{3y0} L}{r^2 \overline{n}_3 \rho_0 c v \Gamma_B} \cdot \frac{1}{2} \frac{1 + \mathbf{S}_{y1} \cdot \mathbf{S}_{y3}}{1 + \left(\xi_{yy}^{ASW}\right)^2} \tag{6.22}$$

$$\beta_{2d} = \frac{4\gamma_e^2 k^2 P_{3x0} L}{r^2 \overline{n}_3 \rho_0 c v \Gamma_B} \cdot \frac{1}{2} \frac{1 + \mathbf{S}_{y1} \cdot \mathbf{S}_{x3}}{1 + \left(\xi_{yx}^{ASW}\right)^2} \tag{6.23}$$

$$\beta_{4a} = \frac{4\gamma_e^2 k^2 P_{1x0} L}{r^2 \overline{n}_1 \rho_0 c v \Gamma_B} \left(\frac{\omega_3}{\omega_1}\right)^2 \cdot \frac{1}{2} \frac{1 + \mathbf{S}_{x1} \cdot \mathbf{S}_{x3}}{1 + \left(\xi_{xx}^{ASW}\right)^2} \tag{6.28}$$

$$\beta_{4b} = \frac{4\gamma_e^2 k^2 P_{1y0} L}{r^2 \overline{n}_1 \rho_0 c v \Gamma_B} \left(\frac{\omega_3}{\omega_1}\right)^2 \cdot \frac{1}{2} \frac{1 + \mathbf{S}_{y1} \cdot \mathbf{S}_{x3}}{1 + \left(\xi_{yx}^{ASW}\right)^2} \tag{6.29}$$

$$\beta_{4c} = \frac{4\gamma_e^2 k^2 P_{1y0} L}{r^2 \overline{n}_1 \rho_0 c v \Gamma_B} \left(\frac{\omega_3}{\omega_1}\right)^2 \cdot \frac{1}{2} \frac{1 + \mathbf{S}_{y1} \cdot \mathbf{S}_{y3}}{1 + \left(\xi_{yy}^{ASW}\right)^2} \tag{6.30}$$

$$\beta_{4d} = \frac{4\gamma_e^2 k^2 P_{1x0} L}{r^2 \overline{n}_1 \rho_0 c v \Gamma_B} \left(\frac{\omega_3}{\omega_1}\right)^2 \cdot \frac{1}{2} \frac{1 + \mathbf{S}_{x1} \cdot \mathbf{S}_{y3}}{1 + \left(\xi_{xy}^{ASW}\right)^2} \tag{6.31}$$

Once again, the change of variables u and v transforms the system of equations (6.1)-(6.6) of counter-propagating waves into the system of equations (6.10)-(6.15) of co-propagating waves. Consequently, we are able to set the initial conditions as $Y_{ij0}(t,0) = [\tanh(a_1(t-b_1))] \cdot [\tanh(-a_2(t-b_2))] + 1$, each of which takes place at the same end of the new coordinate system, where $i=1,2,3$ and $j=x,y$. The parameters a_1 and a_2 determine the rise time of the PW, SW and ASW pulse profiles, while the parameters b_1 and b_2 define the center of the pulses via the expression $|b_2-b_1|/2$.

In this chapter, the sixth order Runge-Kutta method (RK6) was used to numerically solve the system of equations (5.1)-(5.6), and was chosen for its stability, increased accuracy and relatively large step size [90, 91].

6.3 Results and Discussion

Output spectra were calculated by detuning the Stokes and anti-Stokes frequencies, ω_2 and ω_3, synchronously, as done in the typical experimental setup [4, 28, 92]. Output powers were calculated as $P_{ij\text{-}out}=P_{ij0}\cdot Y_{ij\text{-}out}$, $i=1,2,3$ and $j=x,y$, and the total power of the pump, Stokes and anti-Stokes waves was calculated to be $P_i=P_{ix}+P_{iy}$, $i=1,2,3$. Also, the attenuation in the fiber has been approximated as $\alpha_{ij}=\alpha=0.2$ dB/km, $i=1,2,3$ and $j=x,y$, and the following parameters of the fiber were used: $n_{avg}=1.45$, $\gamma_e=0.902$, $\lambda=1550$nm, $\rho_0=2.21$g/cm^3, $v=5616$m/s, $\Gamma_B=0.1$GHz.

For sensing applications such as the ODPA-BOTDA systems [65, 89], the pump and pulse powers are chosen to be relatively low, with $P_{pump} > P_{pulse}$. In addition, the ODPA system functions ideally when the SW and ASW are balanced, causing the gain and loss to eliminate each other, creating a ‘similar’ effect to the substraction process in the differential pulse-width pair Brillouin optical time-domain analysis (DPP-BOTDA) in the electric domain. Consequently, for the simulations performed in this chapter, the pump wave was given a power of $P_{1x}=P_{1y}=1$mW, while the Stokes and anti-Stokes waves were given increasing powers from $P_{2x}=P_{2y}=P_{3x}=P_{3y}=0.1$mW to 0.9mW in nine different simulations. Elliptical birefringences of $\Delta n = 10^{-4}$, 10^{-5} and 10^{-6} were investigated, and compared to the case of negligible birefringence, $\Delta n = 10^{-10}$ with Stokes vector $\boldsymbol{S}=(0, 0, 0)$, which has been taken to be a first-order approximation to truly unpolarized light. A random elliptical polarization has been assigned to the pulses, having a Stokes vector $\boldsymbol{S}=(0.1, 0.9, 0.424)$, which corresponds to polarization *Random4* from Chapter 5. A pulse length of 7.5ns has been chosen for the SW and ASW, respectively.

6.3.1. Gain dominant regime

In this section, pulse powers have been chosen to be between 0.1 mW and 0.6mW. As can be seen from Figure 6.2 below, the output pump spectra look substantially Lorentzian, since the powers chosen allowed the combined Brillouin gain and loss to operate in the gain dominant regime. By increasing in pulse powers from 0.1mW to 0.6 mW, the Brillouin spectrum becomes increasingly distorted. This is caused by an imbalance between the gain and loss processes − since the regime is gain dominant, the loss experienced by the pump wave contributes in creating an asymmetry in the output pump spectra.

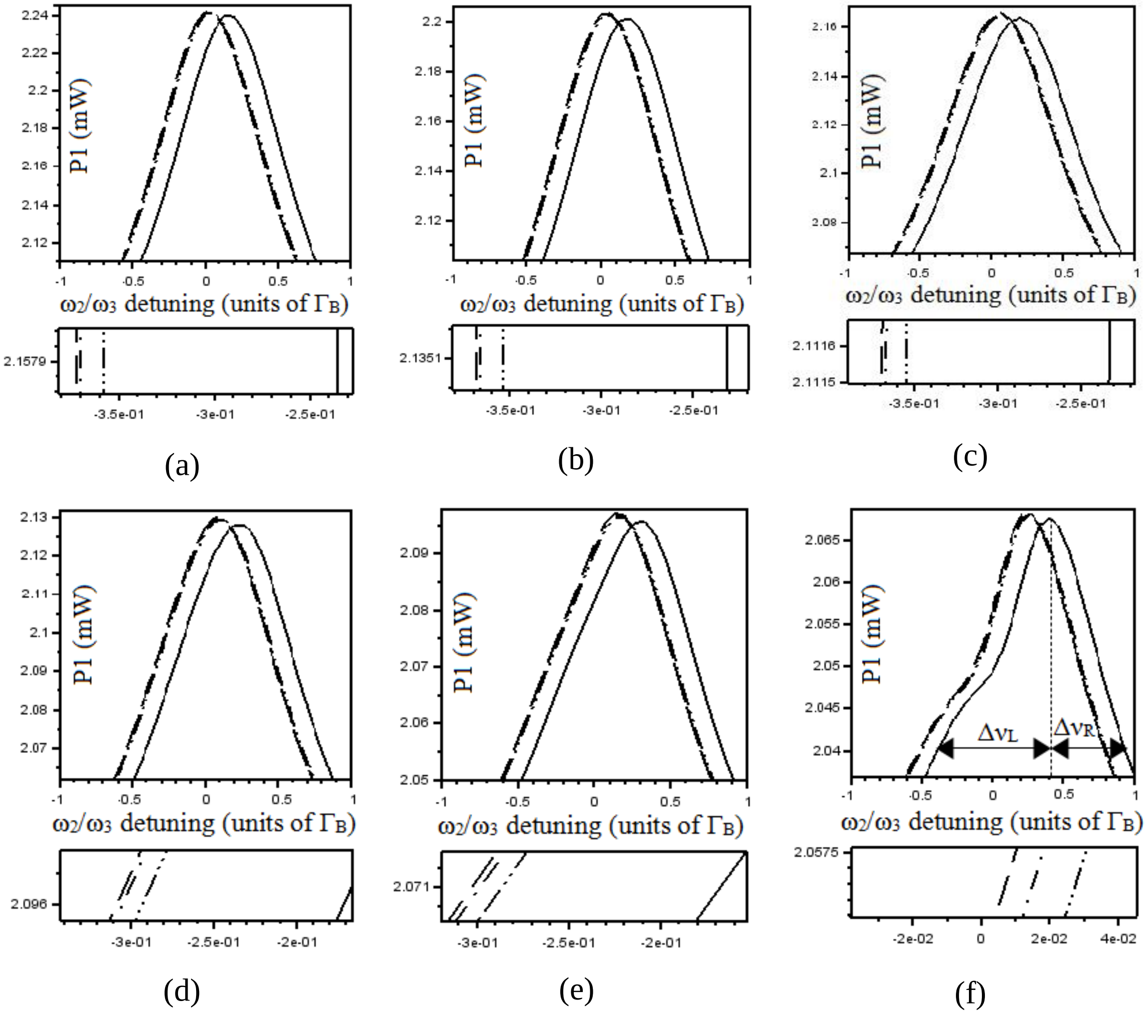

(a) (b) (c)

(d) (e) (f)

Figure 6.2 Output pump spectra. $\boldsymbol{S}$=(0.1, 0.9, 0.42). L=45m. $P_{1x}=P_{1y}$=1mW.
(a) $P_{2x}=P_{2y}=P_{3x}=P_{3y}$=0.1mW; (b) $P_{2x}=P_{2y}=P_{3x}=P_{3y}$=0.2mW; (c) $P_{2x}=P_{2y}=P_{3x}=P_{3y}$=0.3mW;
(d) $P_{2x}=P_{2y}=P_{3x}=P_{3y}$=0.4mW; (e) $P_{2x}=P_{2y}=P_{3x}=P_{3y}$=0.5mW; (f) $P_{2x}=P_{2y}=P_{3x}=P_{3y}$=0.6mW.
—— : $\Delta n = 10^{-4}$; —••—•• : $\Delta n = 10^{-5}$; —•—•— : $\Delta n = 10^{-6}$; — — — : $\Delta n = 10^{-10}$ $\boldsymbol{S}$=(0, 0, 0).

Similar physical principles govern the SBS interaction as described in section 5.3, namely that in addition to the contributing gain and loss processes, birefringence of the optical fiber causes the appearance of a fast and slow axis, which results in two optical modes in the fiber with different SBS frequency shifts. This causes a mismatch in the corresponding momentum vectors of the acoustic waves, thereby making it impossible for both principal axes to be resonant with the acoustic phonons. The mismatch in phonon resonance causes a Brillouin shift, $\Delta \upsilon_B$.

For each power distribution, the spectral shift was calculated for each degree of birefringence, shown in Figure 6.3(A) below.

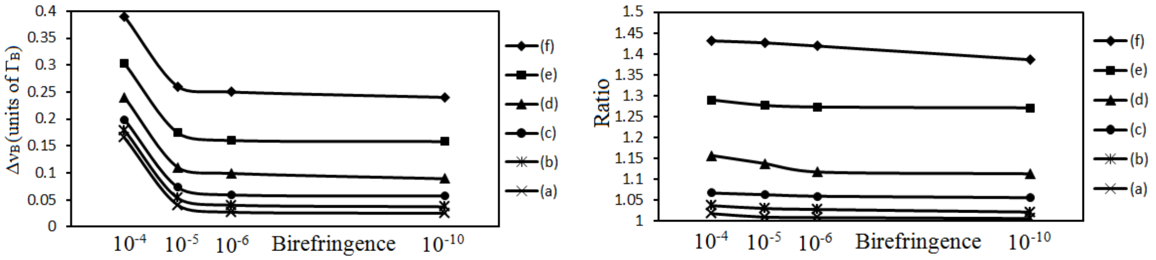

(A) (B)

Figure 6.3. (A) $\Delta \upsilon_B$ dependence on Δn; (B) *Ratio* dependence on Δn. L=45m, $\mathbf{S}$=(0.1, 0.9, 0.42). (a) $P_{2x}=P_{2y}=P_{3x}=P_{3y}$=0.1mW; (b) $P_{2x}=P_{2y}=P_{3x}=P_{3y}$=0.2mW; (c) $P_{2x}=P_{2y}=P_{3x}=P_{3y}$=0.3mW; (d) $P_{2x}=P_{2y}=P_{3x}=P_{3y}$=0.4mW; (e) $P_{2x}=P_{2y}=P_{3x}=P_{3y}$=0.5mW; (f) $P_{2x}=P_{2y}=P_{3x}=P_{3y}$=0.6mW.

It is apparent from Figure 6.3(A) that the degree of birefringence has a nonlinear effect on the Brillouin shift $\Delta \upsilon_B$, in particular, the larger the birefringence, the larger the shift, regardless of the power distribution. Not surprisingly, this nonlinear effect is similar to the case of the two-wave interaction of the PW and SW from Chapter 5. This spectral shift can in turn be used to quantify the birefringence of the optical fiber upon measurement of the output signal. Understandably, the largest shifts occur for the smallest power disparity between the pump and pulses, while the smallest shift occurs for the largest power disparity, since the case of smaller power disparity, shown in Figure 6.2(f), yields a greater spectral distortion due to a stronger competing gain and loss process, while the spectral distortion of Figure 6.2(a) is nearly noticeable.

To assess the effect of birefringence on the asymmetry of the output spectra, the spectral width at half maximum on the left, $\Delta \upsilon_L$, and the spectral width at half maximum on the right,

$\Delta\upsilon_R$, was measured, and their *Ratio*=$\Delta\upsilon_L/\Delta\upsilon_R$ was calculated. Exemplary $\Delta\upsilon_L$ and $\Delta\upsilon_R$ are shown in Figure 6.2(f) for clarity − a perfectly symmetric spectrum would have a *Ratio=1*. Figure 6.3(B) below shows the *Ratios* for the different power distributions, as well as for different Δn, from which it is confirmed that an increase in pulse power increases the spectral distortion (asymmetry) of the output plots. Although the general asymmetrical shape is a result of the competing gain and loss processes, an increase in birefringence contributes to the asymmetry, increasing the disparity between $\Delta\upsilon_L$ and $\Delta\upsilon_R$, as seen by the increase in the *Ratio*, as compared to the case of negligible birefringence.

In the most general case of elliptical birefringence used in both Chapter 5 and the current chapter, there are four running acoustic waves, each having their own resonance frequency. As a result, each of the fast and slow modes have their own resonant frequency at which energy transfer occurs. The result is an asymmetric spectral shape due to the uneven energy transfer along different resonant frequencies. The effects of polarization mode dispersion (PMD) contribute to the spectral distortion seen in Figure 6.3(B), since the existence of a fast and slow axis causes the two optical modes to travel at different speeds, and arrive at the end of the fiber at differing times. In Chapter 5, this has been shown to causes a spectral spreading, and in combination with the multiple resonance frequencies, could account for the increase in distortion.

6.3.2 Competing Gain and Loss regime

In the previous section, although the gain and loss processes were competing, due to the power distributions chosen, the regime was mainly gain dominant. For higher pulse powers, the loss process becomes stronger, making the effects of the gain and loss regime comparable. In this section, pulse powers were increased from 0.7mW to 0.9mW.

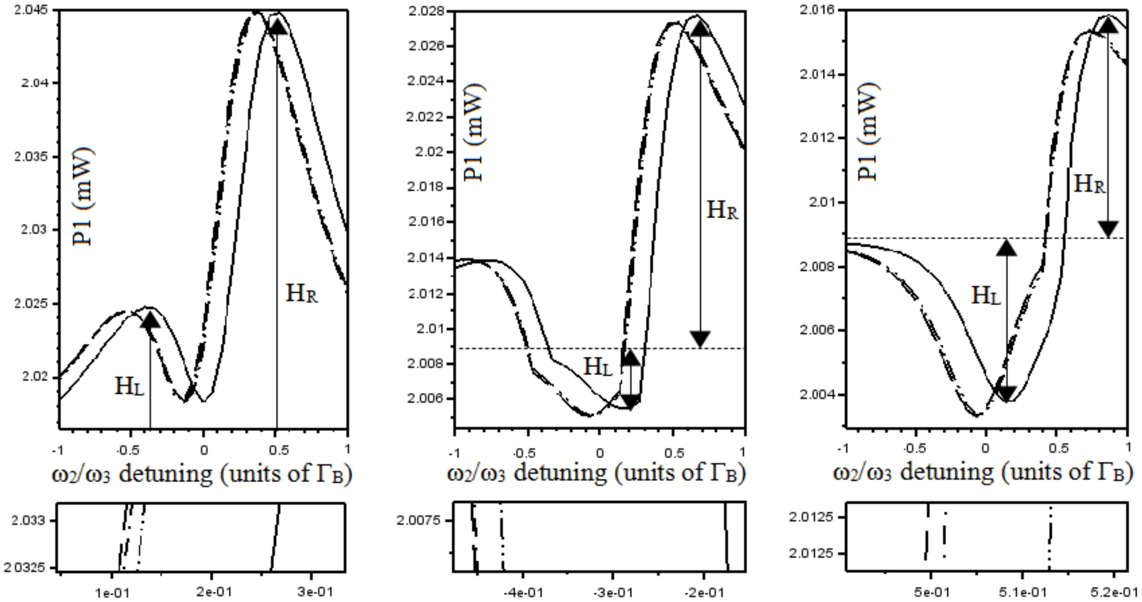

(a) (b) (c)

Figure 6.4 Output pump spectra. ***S***=(0.1, 0.9, 0.42). *L*=45m. $P_{1x}=P_{1y}$=1mW.
(a) $P_{2x}=P_{2y}=P_{3x}=P_{3y}$=0.7mW; (b) $P_{2x}=P_{2y}=P_{3x}=P_{3y}$=0.8mW; (c) $P_{2x}=P_{2y}=P_{3x}=P_{3y}$=0.9mW;
—— : Δn =10^{-4}; —••—•• : Δn =10^{-5}; —•—•— : Δn =10^{-6}; — — — : Δn =10^{-10} ***S***=(0, 0, 0).

As can be seen from Figure 6.4, the comparable gain and loss processes substantially alter the output pump spectrum from its previous Lorentzian shape [28, 30] − in Figure 6.4(a) the spectral deformity results in dual peaks, or a spectral spreading effect, while in Figures 6.4(b)-(c) there is a simultaneous gain and loss spectra. A spectral shift is still apparent − in Figure 6.4(a), the positions of the two peaks have been measured, while in Figures 6.4(b)-(c) the positions of the peaks and troughs have been measured. The results are shown in Figure 6.5(A) below, where the same general trend is observed as in Figure 6.3(A).

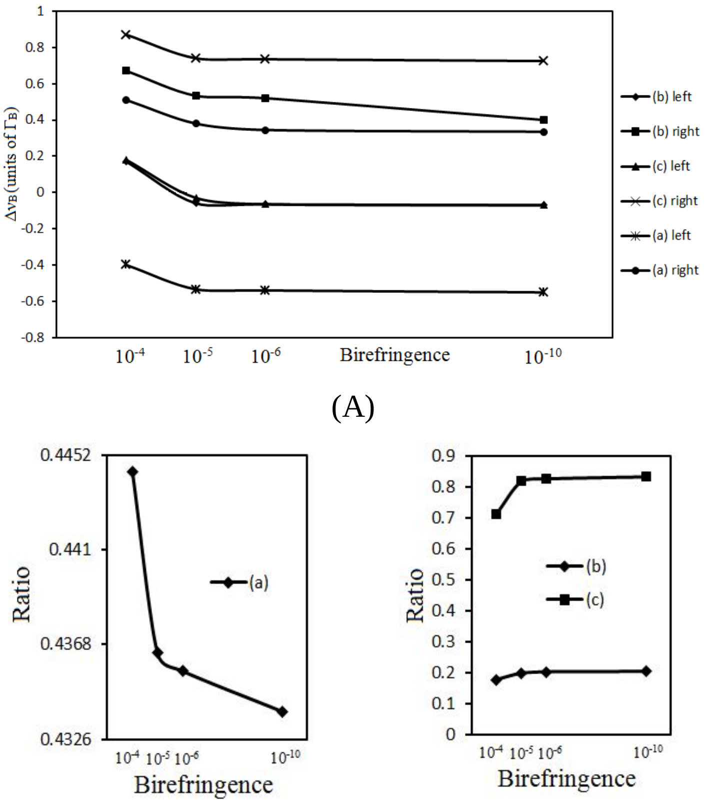

(A)

(B)

(C)

Figure 6.5 (A) $\Delta\upsilon_B$ dependence on Δn; (B)-(C) *Ratio* dependence on Δn. L=45m, **S**=(0.1, 0.9, 0.42). (a) $P_{2x}=P_{2y}=P_{3x}=P_{3y}$=0.7mW; (b) $P_{2x}=P_{2y}=P_{3x}=P_{3y}$=0.8mW; (c) $P_{2x}=P_{2y}=P_{3x}=P_{3y}$=0.9mW.

Similarly to section 6.3.1, to assess the effect of birefringence on the asymmetry of the output spectra, the disparity between peak heights for various degrees of birefringence was measured. Namely for Figure 6.4(a), the height of the peak on the left, H_L, the height of the peak on the right, H_R, was measured, and their $Ratio=H_L/H_R$ was calculated. For Figures 6.4(b)-(c), the dip of the peak on the left, H_L, the height of the peak on the right, H_R, was measured, and their $Ratio=H_L/H_R$ was calculated. The H_L and H_R for each case is shown on Figure 6.4. Figure 6.5(B) below shows the *Ratios* for the different Δn, for the case of spectral burning depicted in Figure 6.4(a), while Figure 6.5(C) shows the *Ratios* for the different power distributions and different Δn for the case of simultaneous gain and loss depicted in Figure 6.4(b)-(c). Similarly to section 6.3.1, a perfectly symmetric spectrum would have a *Ratio=1*.

The spectral spreading effect of Figure 6.4(a) can be explained as a result of a sufficiently strong loss process, which causes a portion of the pump spectra to become substantially depleted, but not sufficiently strong enough to create a lossy spectrum. From Figure 6.5(A), it can be seen that the disparity between the height of the peaks increases with increasing birefringence, represented by the decreasing *Ratio* −birefringence contributes once again to spectral asymmetry.

However, looking at Figure 6.5(C), it is apparent that with increasing birefringence, the disparity between the gain and loss peaks *decreases*, represented by the *Ratio* becoming closer to 1, hence the asymmetry decreases. This can be explained by the same multiple resonant frequency argument as in section 6.3.1. The same energy transfer that contributed to the increase in spectral asymmetry in section 6.3.1, now contributes to creating a more symmetrical simultaneous gain and loss spectrum in Figures 6.4(b)-(c).

As can be seen from Figures 6.2 and 6.4 above, the effects of PMD and PDL caused by birefringence result in a spectral distortion effect, similar to the one reported in [28] for BOTDA systems. Since elliptical polarizations of the interacting pulses include vertical, horizontal, and circular components in their Stokes vectors, it is therefore expected that the resulting gain would be different than in the case of parallel linear alignment, where both waves have the Stokes vector *(1, 0, 0)* and experience maximum gain along one resonant frequency [22, 24, 25]. In the case of elliptical polarization, where there exists an interaction along all components of the Poincaré sphere, an increase in distortion effects is expected, as compared to the case of perfectly parallel polarized light, often attributed to models of Brillouin gain and loss which do not account for polarization [4, 65, 89]. In the gain dominant regime, this distortion contributes to the asymmetry of the output pump spectrum, while conversely in the competing gain and loss regime, the distortion contributes to making the output spectra more symmetrical.

The spectral distortion effect is highly detrimental for the ODPA-BOTDA sensor system employing Lorentzian spectra [65, 89], where an inaccurate spectral reading could cause inaccuracies in the operation of the sensor. Based on the results of this chapter, it is therefore beneficial to choose powers in the gain dominant regime. Not only is the output pump spectrum substantially Lorentzian in this regime, but the higher the disparity in power between the pump and pulses, the more minimal the effect of birefringence is on the spectral distortion of the output pulse.

6.4 Summary

The most general model of elliptical birefringence in an optical fiber has been extended to describe a transient Brillouin interaction including both gain and loss. Spectral distortion effects related to birefringence have been investigated in the gain dominant and competing gain and loss regimes. It has been shown that the spectral distortion caused by birefringence can be minimized by choosing pump and pulse powers with a large disparity.

Chapter 7

Applications of SBS: Photonic Logic

7.1 Introduction

In this chapter, a novel fiber nonlinearity-based technique is proposed to realize all-optical NAND/NOT/AND/OR logic gates, based on the principles of a combined Brillouin gain and loss process in a polarization maintaining fiber (PMF). Combined Brillouin gain and loss is often advantageous over Brillouin gain in the construction of all-optical gates since it describes the energy transfer between three optical waves, as compared to only two optical waves. Additionally, the combination of simultaneous gain and loss acts to improve the signal-to-noise ratio (SNR) by approximately twofold [92] upon measurement of the Brillouin gain spectrum (BGS). This increases the clarity of the signal, as well as the switching contrast in the proposed logic gates. Furthermore, the combined gain and loss scheme is more compact than the traditional Brillouin optical correlation-domain analysis (BOCDA) system [93, 94], which employs successive utilization of the Brillouin gain and loss. The additional parameters in the three-wave interaction give combinations of input powers such that the output signals yield results which correspond to the truth tables of, for example, a NAND gate. The combined Brillouin gain and loss model was used to create several configurations of a functional NAND gate, and a NOT gate. With Brillouin gain one can construct a simplified NOT gate. The combination of the NAND and NOT gates has been used to further construct several configurations of AND and OR gates. Switching contrasts are simulated to be between 20-83% for various configurations.

7.2 Model

The process of combined Brillouin gain and loss has been studied in a single mode optical fiber, with core radius of 4.1μm and power penalty of 0.67 dB/km. The configuration is comprised of a pump wave, which has been taken to be a continuous wave (CW) launched into one end, and a Stokes wave (SW), and an anti-Stokes wave (ASW) launched into the other end. The schematic arrangement is shown on Figure 2.8 in Chapter 2. Since the pump wave is a continuous wave in this case, it will be referred to as 'CW.'

The system is deemed to operate in the steady-state regime with pulse lengths greater than the phonon relaxation time, in this case 10ns [1, 4]. In the slowly varying amplitude approximation, the steady state interaction between the CW, SW, ASW and two acoustic waves (AW_1 and AW_2) is described by the system of equations (2.33)-(2.37) from Chapter 2, shown again below [1, 9, 65].

$$-\frac{dA_1}{dz}=\frac{i\omega_1\gamma_e}{2nc\rho_0}\rho_1 A_2+\frac{i\omega_1\gamma_e}{2nc\rho_0}\rho_2^* A_3-\frac{1}{2}\alpha A_1 \tag{7.1}$$

$$\frac{dA_2}{dz}=\frac{i\omega_2\gamma_e}{2nc\rho_0}\rho_1^* A_1-\frac{1}{2}\alpha A_2 \tag{7.2}$$

$$\frac{dA_3}{dz}=\frac{i\omega_3\gamma_e}{2nc\rho_0}\rho_2 A_1-\frac{1}{2}\alpha A_3 \tag{7.3}$$

$$\left(\Omega_B^2-\Omega_1^2-i\Omega_1\Gamma_B\right)\rho_1=\frac{\gamma_e q_1^2}{4\pi}A_1A_2^* \tag{7.4}$$

$$\left(\Omega_B^2-\Omega_2^2-i\Omega_2\Gamma_B\right)\rho_2=\frac{\gamma_e q_2^2}{4\pi}A_3A_1^* \tag{7.5}$$

Where $\Omega_1=\omega_1-\omega_2$, $\Omega_2=\omega_3-\omega_1$, Ω_1 is the angular frequency of the AW_1 caused by the interaction of CW and SW, Ω_2 is the angular frequency of the AW_2 caused by interaction of CW and ASW, $\mathbf{q}_1$ and $\mathbf{q}_2$ are the acoustic wavevectors defined as $\mathbf{q}_1\approx 2\mathbf{k}_1$ and $\mathbf{q}_2\approx 2\mathbf{k}_1$, where $\mathbf{k}_1$ is the wavevector of the CW, defined as $|\mathbf{k}_1|=n\omega_1/c$. A_1 is the complex amplitude of the CW, A_2 is the complex amplitude of the SW, A_3 is the complex amplitude of the ASW, ρ_1 is the complex amplitude of the AW_1 caused by interaction of CW and SW, ρ_2 is the complex amplitude of the AW_2 caused by interaction of CW and ASW, c is the speed of light, ρ_0 is the density of the fiber, γ_e is the electrostrictive constant, z is the coordinate along the fiber, n is the index of refraction of the fiber, v is the speed of sound in the fiber, Γ_B is the Brillouin linewidth, Ω_B is the Brillouin frequency defined as $\Omega_B = 2nv\omega_1/c$, where ω_1 is the angular frequency of the CW, ω_2 is the angular frequency of the SW, and ω_3 is the angular frequency of the ASW.

For a two-wave configuration describing Brillouin gain, the ASW terms are simply set to ‘0’ in the following analysis. In the above arrangement, the SW and ASW input parameters are known only at the beginning of the fiber, i.e. at $z=0$. Correspondingly, the CW input parameters are known only at the end of the fiber, i.e. at $z=L$, where L is the length of the fiber. Therefore, the boundary conditions for the system of equations (7.1)-(7.5) are similar to previously-studied configurations with one pulse [4, 65]. The conditions for two pulses are as follows

$$|A_1(L)|^2 = A^2_{10}; \quad |A_2(0)|^2 = A^2_{20}; \quad |A_3(0)|^2 = A^2_{30} \tag{7.6}$$

where A^2_{10} , A^2_{20} and A^2_{30} are known squared absolute values of the complex amplitudes A_1 , A_2 , and A_3 respectively. In the dimensionless notation, the system of equations (7.1)-(7.5) becomes

$$\frac{dY_1}{dl} = \beta_1 Y_1 Y_2 - \beta_2 Y_1 Y_3 + \varepsilon Y_1 \tag{7.7}$$

$$\frac{dY_2}{dl} = \beta_3 Y_1 Y_2 - \varepsilon Y_2 \tag{7.8}$$

$$\frac{dY_3}{dl} = -\beta_4 Y_1 Y_3 - \varepsilon Y_3 \tag{7.9}$$

$$Y_4 = \beta_5 Y_1 Y_2 \tag{7.10}$$

$$Y_5 = \beta_6 Y_1 Y_3 \tag{7.11}$$

With corresponding boundary conditions: $Y_1(1)=1; \quad Y_2(0)=1; \quad Y_3(0)=1$ (7.12)

The dimensionless variables $l = z/L$, $Y_1=P_1/P_{10}$, $Y_2=P_2/P_{20}$, $Y_3=P_3/P_{30}$, $Y_4=|\rho_1/\rho_0|^2$, $Y_5=|\rho_2/\rho_0|^2$, $\varepsilon = \alpha L$ have been introduced to derive the system of equations (7.7)-(7.11), as well as the following β-coefficients.

$$\beta_1 = \frac{2\gamma_e^2 k^3 L P_{20}}{\pi r^2 n^3 c \rho_0 \Omega_1 \Gamma_B} \cdot \frac{1}{1+\xi_1^2} \tag{7.13}$$

$$\beta_2 = \frac{2\gamma_e^2 k^3 L P_{30}}{\pi r^2 n^3 c \rho_0 \Omega_2 \Gamma_B} \cdot \frac{1}{1+\xi_2^2} \tag{7.14}$$

$$\beta_3 = \frac{2\gamma_e^2 k^3 L P_{10}}{\pi r^2 n^3 c \rho_0 \Omega_1 \Gamma_B} \cdot \frac{1}{1+\xi_1^2} \tag{7.15}$$

$$\beta_4 = \frac{2\gamma_e^2 k^3 L P_{10}}{\pi r^2 n^3 c \rho_0 \Omega_2 \Gamma_B} \cdot \frac{1}{1+\xi_2^2} \tag{7.16}$$

$$\beta_5 = \left(\frac{2\gamma_e k^2}{\pi r^2 n c \rho_0 \Omega_1 \Gamma_B} \right)^2 \cdot \frac{1}{1+\xi_1^2} \cdot P_{10} P_{20} \tag{7.17}$$

$$\beta_6 = \left(\frac{2\gamma_e k^2}{\pi r^2 n c \rho_0 \Omega_2 \Gamma_B} \right)^2 \cdot \frac{1}{1+\xi_2^2} \cdot P_{10} P_{30} \tag{7.18}$$

$$\xi_1 = \frac{\Omega_B^2 - \Omega_1^2}{\Omega_1 \Gamma_B} \quad \mathit{and} \quad \xi_2 = \frac{\Omega_B^2 - \Omega_2^2}{\Omega_2 \Gamma_B} \tag{7.19}$$

L is the fiber length, P_1 is the CW power, P_{10} is the initial CW power, P_2 is the SW power, P_{20} is the initial SW power, P_3 is the ASW power, P_{30} is the initial ASW power, and r is the radius of fiber, and $\omega=\omega_1\approx\omega_2\approx\omega_3$ and $\mathbf{q}=\mathbf{q}_1\approx\mathbf{q}_2$.

The system of equations (7.7)-(7.11) was solved numerically, making use of boundary conditions (7.12), to feature the power distribution of the ASW inside the optical fiber, for given input CW and SW powers. A typical power distribution of the ASW is shown on Figure 7.1 for the case of (a) combined Brillouin gain and loss, for which all three initial powers are 10mW, and (b) Brillouin loss, where the Stokes input power has been set to '0'. The goal of studying these distributions is to show that the model described in the system of equations (7.7)-(7.11) does, indeed, describe the combined Brillouin gain and loss process, depicted by the solid line, which shows significant depletion reduction as compared with the Brillouin loss processes, depicted by the dashed line. The parameters used for the simulations in this paper are shown in Table 7.1 below.

Table 7.1 Simulation Parameters

Index of reflection n	1.48
Electrostrictive constant γ_e	0.902
Wavelength of pump laser λ	1550 nm
Density of fiber ρ_0	2.21 g/cm^3
Speed of sound v	5616 m/s
Brillouin Linewidth Γ_B	0.1 GHz
Fiber attenuation α	0.2 dB/km
Power penalty	0.67 dB/km

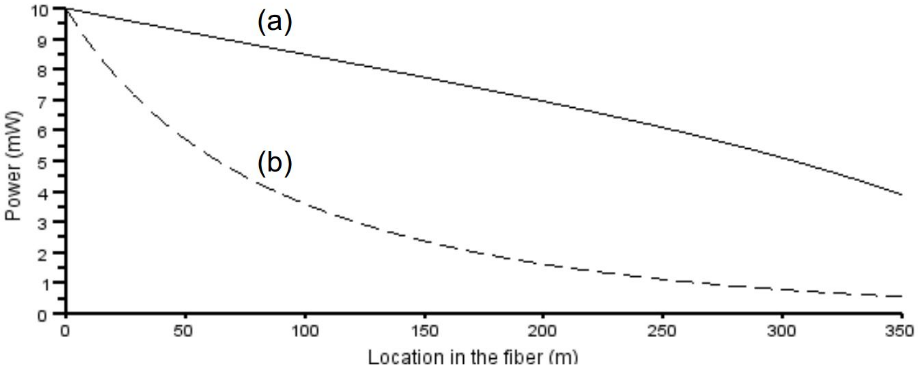

Figure 7.1 ASW power distribution inside the optical fiber.

(a) Gain *and* Loss regime: P_{20}=10mW; (b) Loss regime: P_{20}=0mW

n=1.48, γ_e=0.902, λ=1550nm, ρ_0=2.21 g/cm^3, v=5616 m/s, Γ_B=0.1 GHz, α=0.2 dB/km, L=350m, P_{10}=10mW, P_{30}=10mW.

7.3 Results and Discussion

It has been determined that obtaining a logical output of exactly 0.1mW or 10mW is not feasible. However, it is possible to obtain output signals within a given level of tolerance. In this manuscript, a threshold value of at least 20% is deemed acceptable. Switching contrast bar graphs are introduced in Figures 7.2, 7.5, 7.6 and 7.9, showing the output signals as percentages of the optimal signal power of 10mW. The tolerance between the low and high thresholds is the resultant switching contrast of the logic gate configuration. The higher the switching contrast, the more accurate the logical ‘0’ and ‘1’ representation is by the real circuit.

7.4 NAND gate

7.4.1 Configuration I

In Configuration I, a fiber length of L=2300m was used (shorter fiber length is possible with lower switching contrast), and the ASW reference signal was kept constant at P_{30}=40mW. The logical output ‘1’ corresponds to several different values of output power, namely

25.1mW, 25.0mW and 7.48mW for the logical inputs ‘0 0’, ‘0 1’ and ‘1 0’ respectively, while the logical output ‘0’ corresponds to an output ASW power of 5.47mW.

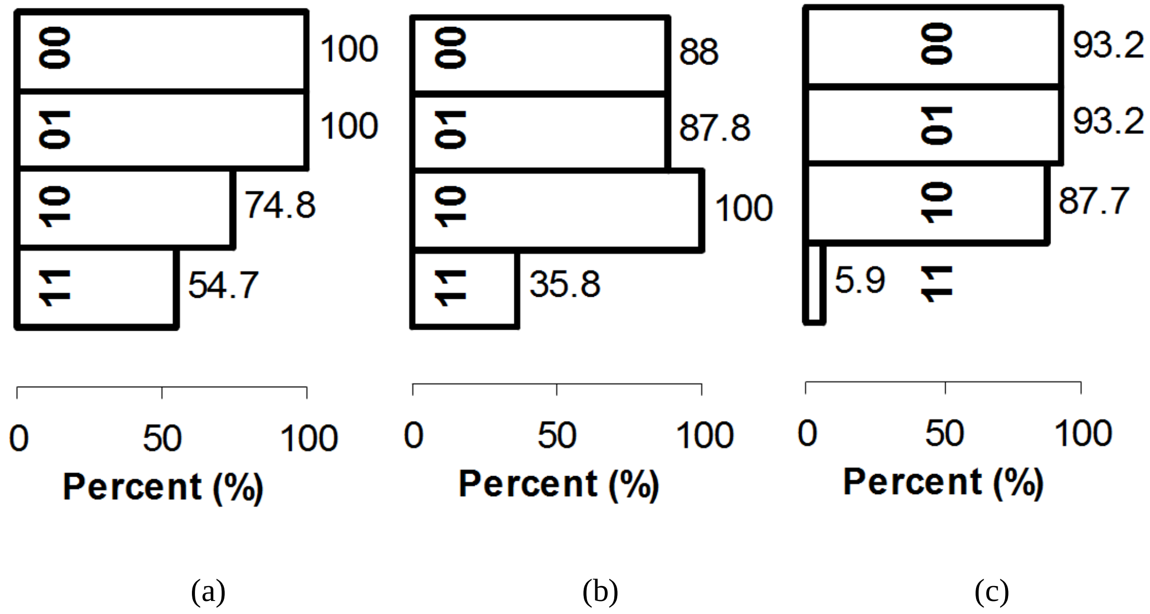

Figure 7.2 NAND gate switching contrast plots

(a) Configuration I: Low threshold: 54.7%, High threshold: 74.8%, Tolerance: 20.6%

(b) Configuration II: Low threshold: 35.8%, High threshold: 87.8%, Tolerance: 52.7%

(c) Configuration III: Low threshold: 5.9%, High threshold: 87.7%, Tolerance: 82.8%

As can be seen from Figure 7.2(a), Configuration I has a switching contrast of 20.6%, which could be acceptable. It is technologically the easiest to implement, since all signals are in resonance, and no frequency detuning is required.

If a higher switching contrast is desired, amplitude modulation of the P_{30} input ASW power is introduced, arriving to Configuration II.

7.4.2 Configuration II

Configuration II is characterized by a slightly shorter fiber length of L=500m, as well as an amplitude modulation of the input ASW power for various inputs. Namely, for the ‘0 0’, ‘0

1’ and ‘1 1’ inputs, P_{30}=10mW, while for the ‘1 0’ input, P_{30}=40mW. As a result, output powers of 8.80mW, 8.78mW, 10.9mW and 3.58mW were obtained for the logical inputs ‘0 0’, ‘0 1’, ‘1 0’ and ‘1 1’ respectively.

As can be seen from Figure 7.2(b), Configuration II has an increased switching contrast of 52.7%. The trade-off is the required change in ASW input power for the “1 0” logical input. As such, some additional calibrations would be needed to realize the function of this logic gate, since it would require amplitude switching of the reference ASW signal, making it more difficult to implement than Configuration I.

To further optimize the switching contrast, detuning of the SW or ASW signals has been introduced instead of amplitude modulation of the P_{30} signal in Configuration III.

7.4.3 Configuration III

Figure 7.3 below depicts the output ASW power spectra for typical NAND gate inputs. From Figure 7.3, it can be seen that it is possible to optimize the output signal via detuning of either the SW or ASW signals. For each input ‘0 0’, ‘0 1’, ‘1 0’ and ‘1 1’, a detuning greater than ±3Γ_B is sufficient to obtain a maximum switching contrast within 2-3%.

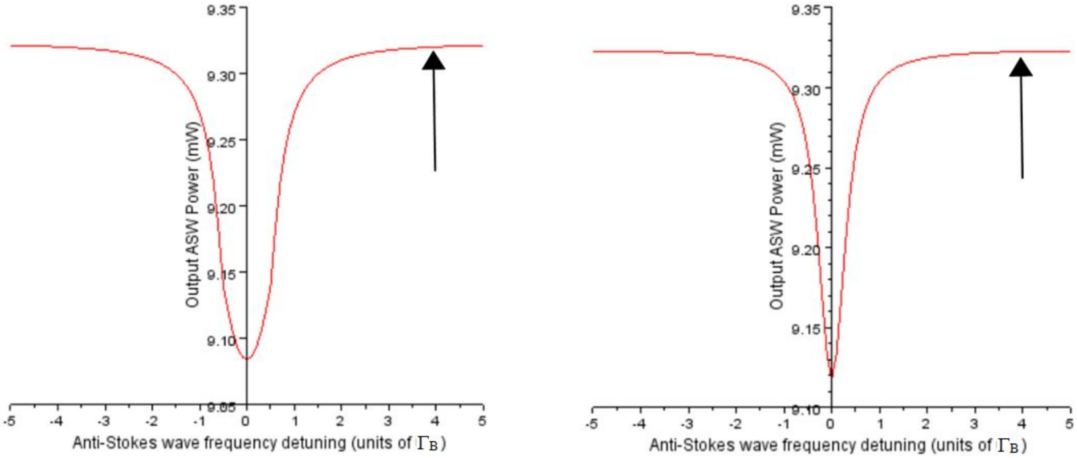

(a) (b)

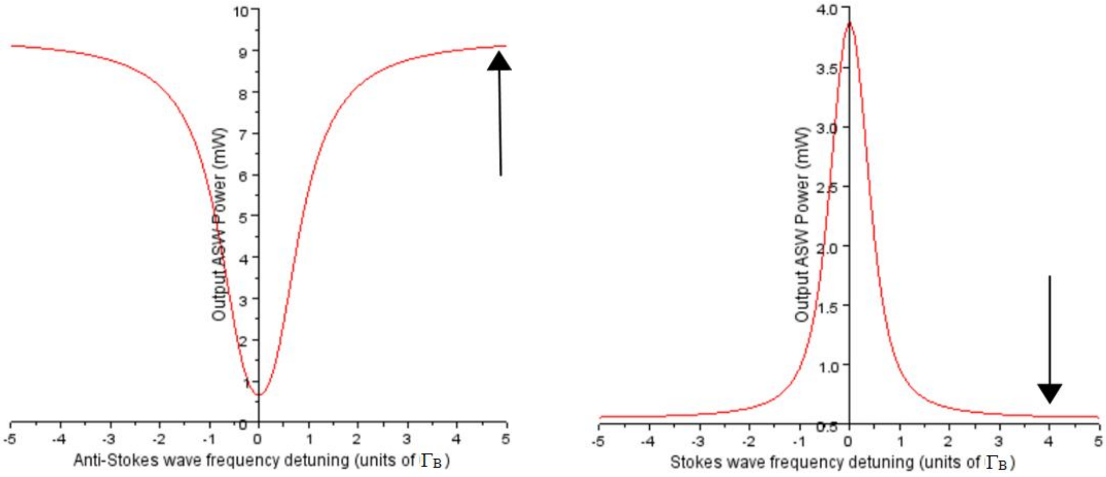

(c) (d)

Figure 7.3 Output ASW power spectra.

(a) ‘0 0’ input, (b) ‘0 1’ input, (c) ‘1 0’ input, (d) ‘1 1’ input.

Configuration II utilizes a fiber length of L=350m, as well as detuning of the SW and ASW to achieve a maximum switching contrast. Namely, for the ‘0 0’, ‘0 1’ and ‘1 0’ inputs, the ASW is detuned by $\pm 3\Gamma_B$, while for the ‘1 1’ input, the SW is detuned by $\pm 3\Gamma_B$. As a result, output powers of 9.32mW, 9.32mW, 8.77mW, and 0.59mW were obtained for the logical inputs ‘0 0’, ‘0 1’, ‘1 0’ and ‘1 1’ respectively. In this configuration, the reference ASW signal was held constant at P_{30}=10mW.

Configuration III requires a tunable laser source, capable of detuning the SW and ASW separately. Although technologically this is more complicated to realize, the tunable frequency range is very large and, in this case, any detuning outside $\pm 3\Gamma_B$ (about ±0.3 GHz) will provide the maximum switching contrast of 82.8%, within 2-3%. As such, this configuration also benefits from a shorter fiber length of 350m, which acts to compactify the setup.

7.5 NOT gate

7.5.1 Configuration IV

Although, according to DeMorgan’s Theorem [95], any logic gate may be constructed from several NAND gates, practical considerations may require a simplified design of certain simple gates, such as the NOT, AND, etc. In view of this, the design for an all-optical NOT gate was considered, using a similar approach as for the NAND gate described in previous sections. The combination of the NAND and NOT gates may be used to create a simplified AND gate, which would require minimal calibration and yield a high switching contrast.

In Configuration IV, the initial CW power, P_{10} , was chosen to be the input signal, and the output ASW power, $P_{3\text{-}out}$, was taken to be the output signal of the optical gate. In this case, the input SW is a reference signal, and was held constant at P_{20}=10mW. As before, a power of 0.1mW was assigned a logical value of ‘0’, while a power of 10mW was assigned a logical value of ‘1’. Output powers of 9.11mW and 3.89mW were obtained for the logical inputs ‘0’ and ‘1’ respectively. In this configuration, a fiber length of L=350m was used.

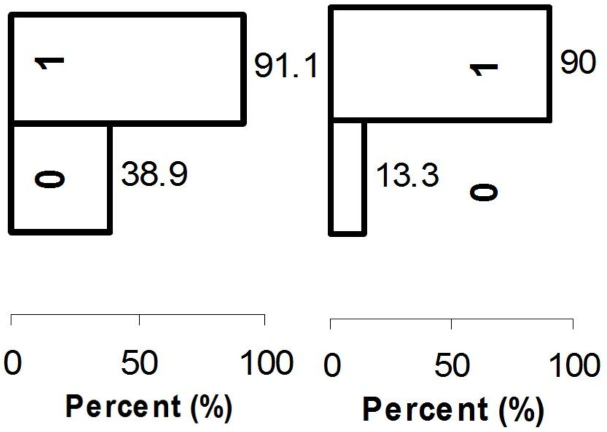

(a) (b)

Figure 7.4 NOT gate switching contrast plots

(a)Configuration IV: Low threshold: 38.9%, High threshold: 91.1%, Tolerance: 52.9%

(b)Configuration V: Low threshold: 13.3%, High threshold: 90.0%, Tolerance: 77.6%

The proposed configuration of the NOT gate has all the technological benefits of the NAND gate in Configuration I, as well as a switching contrast of 52.9%, as can be seen from Figure 7.4(a).

7.5.2 Configuration V

Another possible realization of the NOT gate utilizes the two-wave configuration of Brillouin gain. In this case, the initial SW power, P_{20}, was chosen to be the input signal, and the output CW power, $P_{1\text{-}out}$, was taken to be the output signal of the optical gate. The input CW was taken to be the reference signal, and was held constant at P_{10}=10mW. A power of 0.1mW was assigned a logical value of ‘0’, while a power of 10mW was assigned a logical value of ‘1’. Output powers of 9.0mW and 1.33mW were obtained for the logical inputs ‘0’ and ‘1’ respectively. In this configuration, a fiber length of L=350m was used.

As seen in Figure 7.4(b), the proposed configuration of the NOT gate has a higher switching contrast of 77.6%, as compared to Configuration IV. Additionally, the current NOT gate, based on the two-wave SBS interaction is substantially simpler in design, requiring the use of only two optical waves, as compared to three optical waves.

7.6 AND gate

7.6.1 Configuration VI

In the current configuration, an AND gate is constructed by connecting the NAND gate of Configuration III with the NOT gate of Configuration IV, shown schematically in Figure 7.5 below.

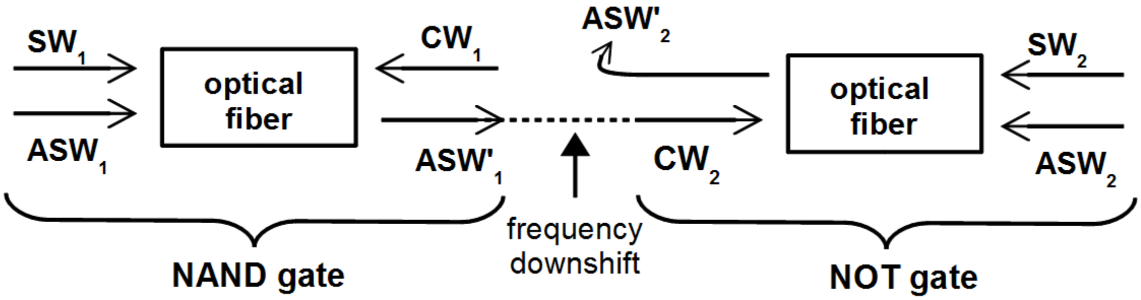

Figure 7.5 Schematic of Configuration VI: AND gate.

P_{10} and P_{20}, represented by CW₁ and SW₁ in Figure 7.5 above, are the input signals of the AND gate, while the initial power of the reference signal ASW₁ is held constant at P_{30}=10mW. The output ASW'₁ signal from the NAND gate, $P_{3\text{-}out}$, is frequency downshifted from ω_3 to ω_1, turning it into an effective CW₂ wave, which is the input signal for the NOT gate. SW₂ and ASW₂ are the reference signals of the NOT gate, and are kept constant at 10mW. The output signal of the AND gate is the ASW'₂ signal. As before, a power of 0.1mW was assigned a logical value of '0', while a power of 10mW was assigned a logical value of '1'. Output powers of 4.02mW, 4.02mW, 4.14mW and 8.31mW were obtained for the logical inputs '0 0', '0 1', '1 0' and '1 1' respectively. In this configuration, a fiber length of L=350m was used for both the NAND gate and NOT gate.

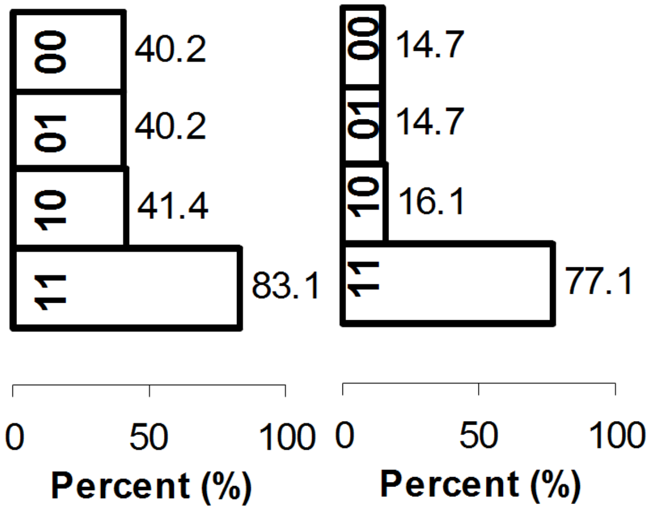

(a) (b)

Figure 7.6 AND gate switching contrast plots.

(a) Configuration VI: Low threshold: 40.2%, High threshold: 83.1%, Tolerance: 42.3%

(b) Configuration VII: Low threshold: 16.1%, High threshold: 77.1%, Tolerance: 61.8%

The same detuning must be applied to optical signals entering the NAND gate as stated in the description of Configuration III. For the subsequent NOT gate, input signals should be kept at resonance.

As can be seen from Figure 7.6(a), Configuration VI of the AND gate yields a switching contrast of 42.3%.

7.6.2 Configuration VII

In the current configuration, an AND gate is constructed by connecting the NAND gate of Configuration III with the NOT gate of Configuration V, shown schematically in Figure 7.7 below.

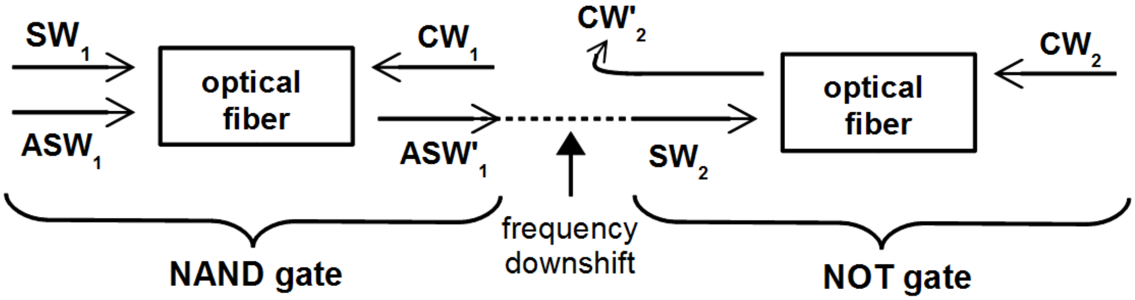

Figure 7.7 Schematic of Configuration VII: AND gate.

Similar to Configuration VI, P_{10} and P_{20}, represented by CW_1 and SW_1 in Figure 7.7 above, are the input signals of the AND gate, while the initial power of the reference signal ASW_1 is held constant at P_{30}=10mW. The output ASW'_1 signal from the NAND gate, $P_{3\text{-}out}$, is frequency downshifted from ω_3 to ω_2, turning it into an effective SW_2 wave, which is the input signal for the NOT gate. The reference signal CW_2 is kept constant at 10mW. The output signal of the AND gate is the CW'_2 signal. As usual, a power of 0.1mW was assigned a logical value of '0', while a power of 10mW was assigned a logical value of '1'. Output powers of 1.47mW, 1.47mW, 1.61mW and 7.71mW were obtained for the logical inputs '0

0’, ‘0 1’, ‘1 0’ and ‘1 1’ respectively. Once again, a fiber length of *L*=350m was used for both the NAND gate and NOT gate.

The same detuning must be applied to optical signals entering the NAND gate as stated in the description of Configuration III. For the subsequent NOT gate, input signals should be kept at resonance.

As can be seen from Figure 7.6(b), Configuration VI of the AND gate yields a switching contrast of 61.8%. This is higher than the switching contrast on Configuration VI; additionally, the setup is substantially simpler since the NOT gate from Configuration V requires a two-wave SBS interaction.

7.6.3 Configuration VIII

In another possible configuration, loops mirrors [96] and High-Order Mode Fibers (HOM) [97, 98], are utilized to re-use the fiber under test. Loops mirrors redirect output light back into a different mode of the HOM, thereby compactifying the setup. In this configuration only one fiber, which must be an HOM fiber, is required. Since HOM fibers do not maintain the polarization of propagating light, this configuration is more prone to polarization instabilities and PMD. Another possibility is to use a PMF, whereby loop mirrors redirect output light back into a perpendicularly polarized state in the same fiber, similar to the implemented schemes in [99, 100]. This would also act to compactify the setup, while helping to eliminate the influence of polarization instability and PMD.

7.7 OR gate

7.7.1 Configuration IX

To create a functional OR gate, three NAND gates from Configuration III must be connected, shown schematically in Figure 7.8 below.

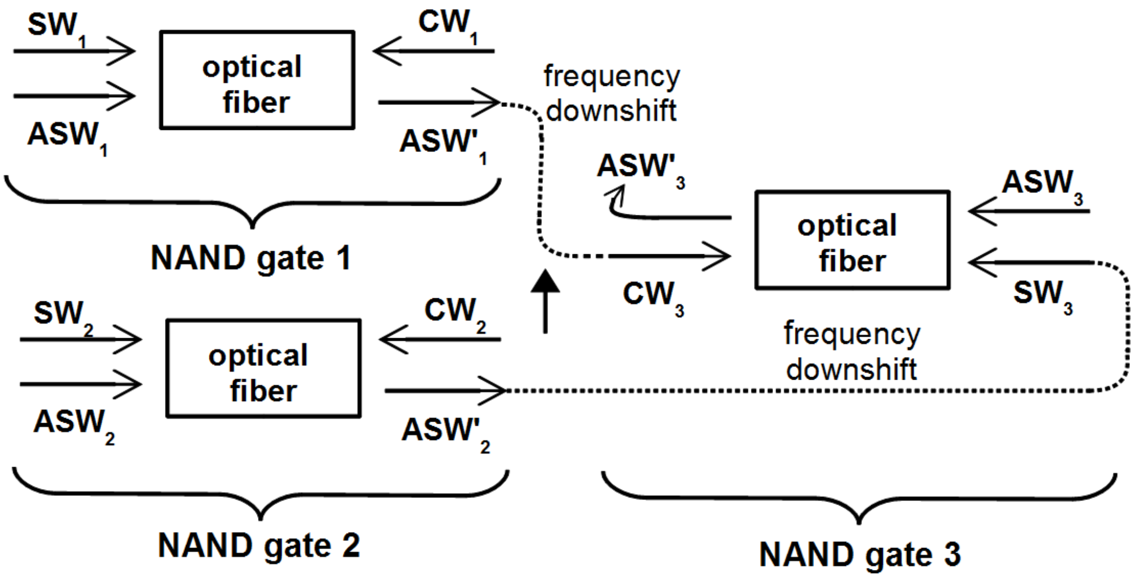

Figure 7.8 Schematic of Configuration IX: OR gate.

CW_1 and SW_1, as well as CW_2 and SW_2 in Figure 7.8 above, are the input signals of the OR gate. CW_1 and SW_1, and CW_2 and SW_2, must always have identical power. The initial power of the reference signals ASW_1 and ASW_2 is held constant at 10mW. The output ASW'_1 signal from NAND gate 1 is frequency downshifted from ω_3 to ω_1, turning it into an effective CW_3 wave, which is an input signal for the NAND gate 3. The output ASW'_2 signal from NAND gate 2 is frequency downshifted from ω_3 to ω_2, turning it into an effective SW_3 wave, which is another input signal for the NAND gate 3. The reference signal of NAND gate 3, ASW_3, is held constant at 10mW. The output signal of the OR gate is the ASW'_3 signal. A power of 0.1mW was assigned a logical value of '0', while a power of 10mW was assigned a logical value of '1'. Output powers of 0.68mW, 8.89mW, 9.31mW and 9.29mW were obtained for the logical inputs ‘0 0’, ‘0 1’, ‘1 0’, and ‘1 1’ respectively. A fiber length of L=350m was used for all three NAND gates.

The same detuning must be applied to optical signals entering all three NAND gates as stated in the description of Configuration III.

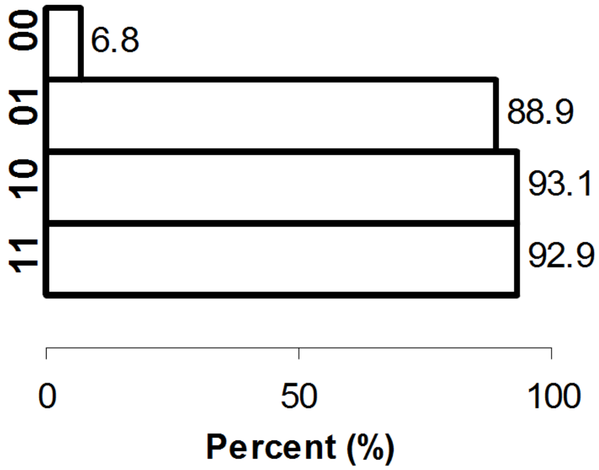

Figure 7.9 OR gate switching contrast plot.
Low threshold: 6.8%, High threshold: 88.9%, Tolerance: 83.0%.

As can be seen from Figure 7.9, Configuration IX of the OR gate yields a switching contrast of 83.0%. Though the current configuration is more complicated than the previous ones, it also yields an extremely high switching contrast.

7.7.2 Configuration X

In the current configuration, an OR gate is constructed by connecting a NAND gate with two *3-wave* NOT gates, shown schematically in Figure 7.10 below.

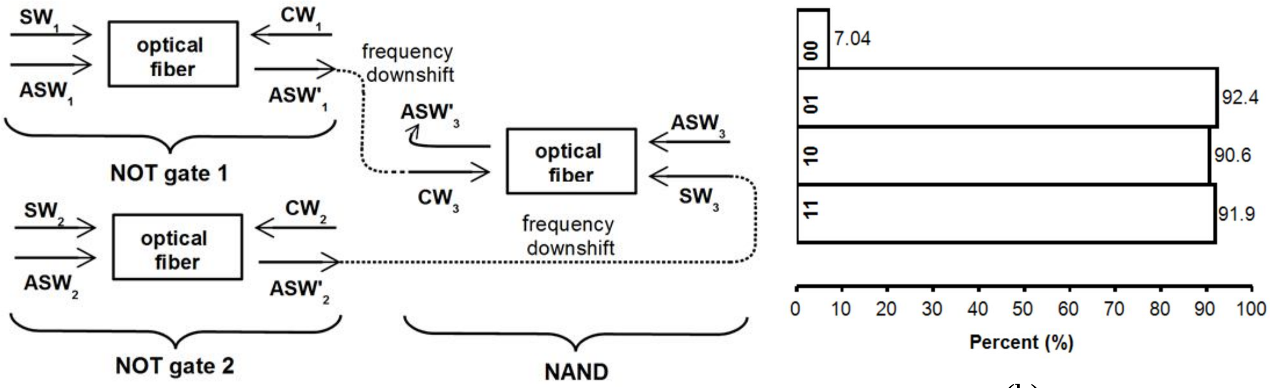

(b)

(a)

Figure 7.10 (a) Schematic of Configuration X: OR gate, (b) OR gate switching contrast plot, Low threshold: 7.04%, High threshold: 90.6%, Tolerance: 83.6%.

CW_1, as well as CW_2, in Figure 7.10(a) above, are the input signals of NOT gate 1 and NOT gate 2, respectively, as well as the two input signals of the OR gate. Similarly, SW_1 and ASW_1, as well as SW_2 and ASW_2, are the reference signals of each NOT gate, which are held constant at 10mW. The output ASW'_1 signal from NOT gate 1 is frequency downshifted from ω_3 to ω_1, turning it into an effective CW_3 wave, which is an input signal for the NAND gate. The output ASW'_2 signal from NOT gate 2 is frequency downshifted, from ω_3 to ω_2, turning it into an effective SW_3 wave, which is another input signal for the NAND gate. The reference signal of the NAND gate, ASW_3, is held constant at 10mW. The output signal of the OR gate is the ASW'_3 signal. Output powers of 0.704mW, 9.24mW, 9.06mW, and 9.19mW were obtained for the logical inputs ‘0 0’, ‘0 1’, ‘1 0’, and ‘1 1’, respectively. A fiber length of L=350m was used for all three gates.

As can be seen from Figure 7.10(b), Configuration X of the OR gate yields a high switching contrast of 83.6%. This is comparable to the OR gate proposed in Configuration IX, which has a switching contrast of 83.0%. Additionally, NOT gate 1 and NOT gate 2 have only one input each, namely CW_1 and CW_2 respectively. The SW_1 and ASW_1, and SW_2 and ASW_2, respectively, are kept as reference signals. In the OR gate of Configuration IX, a NAND gate 1 and a NAND gate 2 are employed – each having two input signals, CW_1 and SW_1, and CW_2 and SW_2, respectively, which must be carefully calibrated to match each other for each logical input. Such calibration is time-consuming, and often difficult to achieve.

Configuration X eliminates this difficulty by employing NOT gate 1 and NOT gate 2, which by virtue of the operation of a NOT gate, have only one input signal each, and do not require any such calibration. As a result, Configuration X of the all-optical OR gate has the benefit of being simpler to operate and more compact as compared to the existing variant of Configuration IX.

7.7.3 Configuration XI

In the current configuration, an OR gate is constructed by connecting a NAND gate with two *2-wave* NOT gates, shown schematically in Figure 7.11 below.

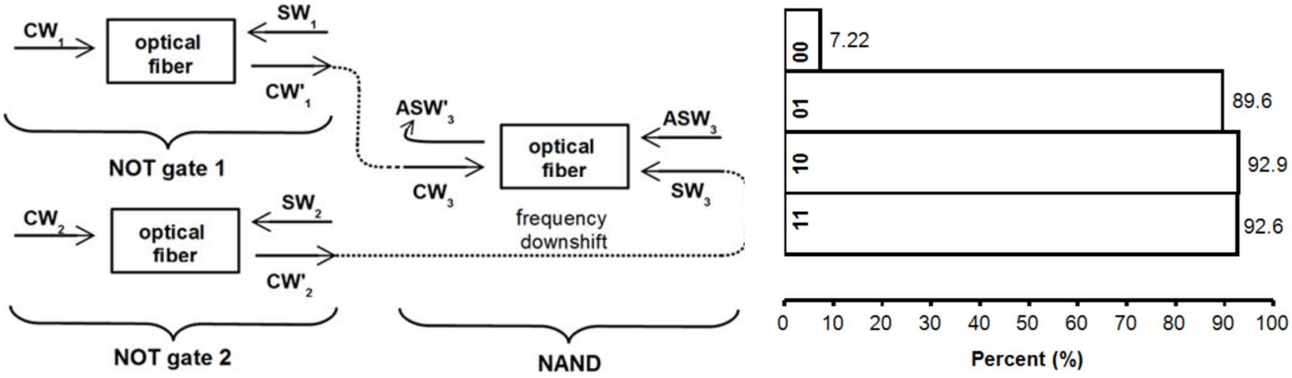

(a) (b)

Figure 7.11 (a) Schematic of Configuration XI: OR gate, (b) OR gate switching contrast plot, Low threshold: 7.22%, High threshold: 89.6%, Tolerance: 82.4%.

SW$_1$, as well as SW$_2$, in Figure 7.11(a) above, are the input signals of NOT gate 1 and NOT gate 2, respectively, as well as the two input signals of the OR gate. Similarly, CW$_1$ and CW$_2$ are the reference signals of NOT gate 1 and NOT gate 2, respectively, which are held constant at 10mW. The output CW’$_1$ signal from NOT gate 1 is redirected towards the NAND gate into an effective CW$_3$ wave, which is an input signal for the NAND gate. The output CW’$_2$ signal from NOT gate 2 is frequency downshifted from ω_1 to ω_2, turning it into an effective SW$_3$ wave, which is another input signal for the NAND gate. The reference signal of the NAND gate, ASW$_3$, is held constant at 10mW. The output signal of the OR gate is the ASW’$_3$ signal. Output powers of 0.722mW, 8.96mW, 9.29mW, and 9.26mW were obtained for the logical inputs ‘0 0’, ‘0 1’, ‘1 0’, and ‘1 1’, respectively. A fiber length of *L*=350m was used for all three gates.

As can be seen from Figure 7.11(b), Configuration XI of the OR gate yields a high switching contrast of 82.4%. In addition to the existing benefits of using two NOT gates in place of two NAND gates, as discussed in section 7.7.2, another benefit of Configuration XI is that only one frequency downshift is required, from CW'$_2$ to SW$_3$, which greatly increases accuracy and ease of operation, while decreasing the bulk. In summary, the setup of Configuration XI is even simpler to operate and more compact than that of Configuration X, without any significant compromise on switching contrast.

7.8 General method of logic gate construction

In the previous sections 7.4-7.7, configurations to realize NAND/NOT/AND/OR gates are proposed. In these sections, specific parameters of the fiber are defined for ideal operation of the proposed gates. In the current section, we will outline a method by which it is possible to find other parameters of the fiber, to realize functional optical gate configurations.

7.8.1 Configuration V: NOT gate

The NOT gate of Configuration V is the simplest, so we will start with this one. Figure 7.12 depicts a flow chart describing the steps of an algorithm needed to find the correct parameters to realize a NOT gate of Configuration V.

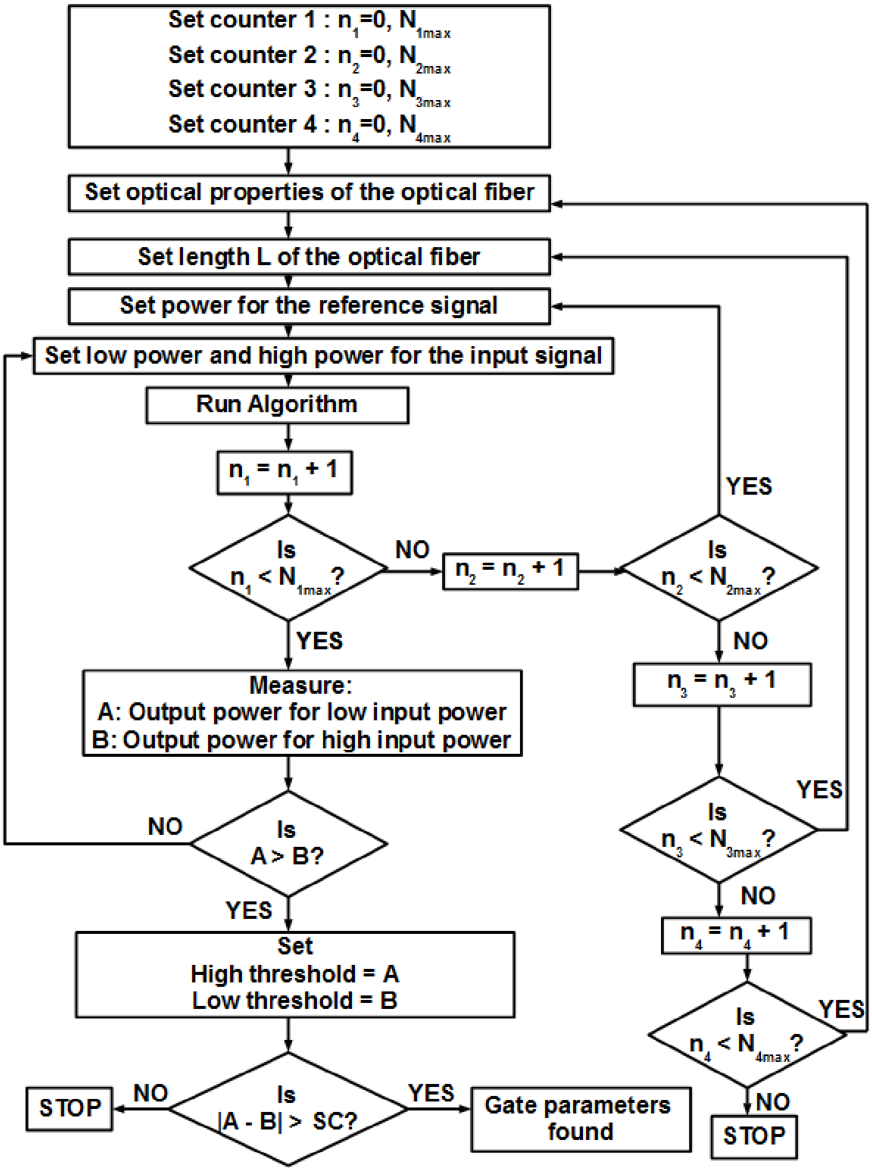

Figure 7.12 Flow chart for NOT gate of Configuration V.

Four counters are set, n_1, n_2, n_3, and n_4, with maximum values N_{1max}, N_{2max}, N_{3max}, N_{4max}, to ‘sift’ through: i) the parameters of the optical fiber, ii) the length L of the fiber, iii) the power of the reference signal, and iv) the low and high powers of the input signal. With this arbitrary choice of initial parameters, length and powers, the differential equations (7.7)-(7.11) are solved, denoted by ‘Run Algorithm’, after which each counter is increased. If the high threshold, denoted as ‘A,’ is higher than the low threshold, denoted as ‘B,’ by a value greater than the switching contrast, denoted as ‘SC,’ then the gate parameters are found.

If not, the algorithm is repeated with a different combination of fiber parameters, length and powers until the correct gate parameters are found.

7.8.2 Configuration IV: NOT gate

For the slightly more complex setup of the NOT gate of Configuration IV, we have the flow chart of Figure 7.13.

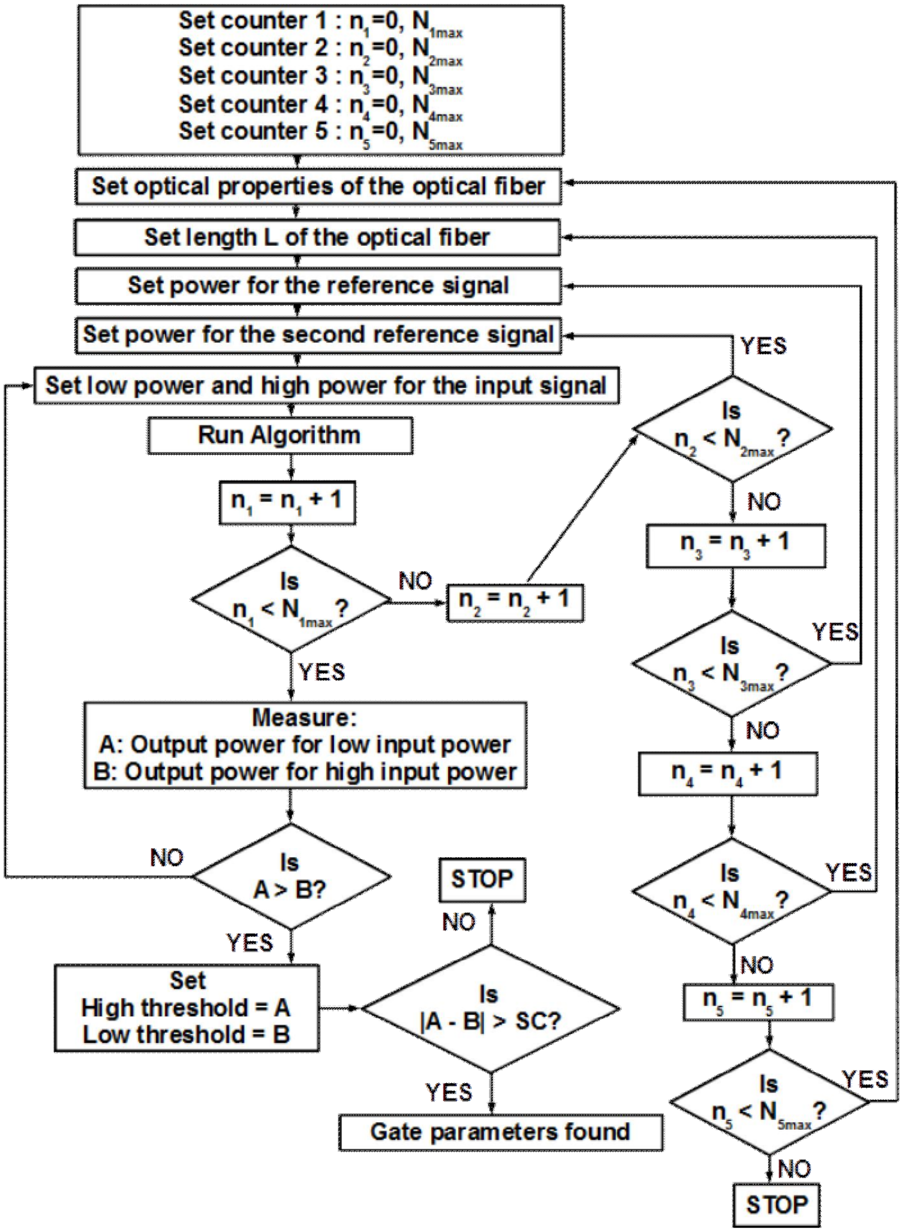

Figure 7.13 Flow chart for NOT gate of Configuration IV.

For the algorithm of the NOT gate of Configuration IV, an additional counter is added, n_5, with maximum N_{5max}, to take into account the power of the second reference signal. The rest of the algorithm remains unchanged.

7.8.3 Configurations I and II: NAND gates

For the NAND gates of Configurations I and II, which do not have frequency detuning, we have the following flow chart, shown in Figure 7.14 below.

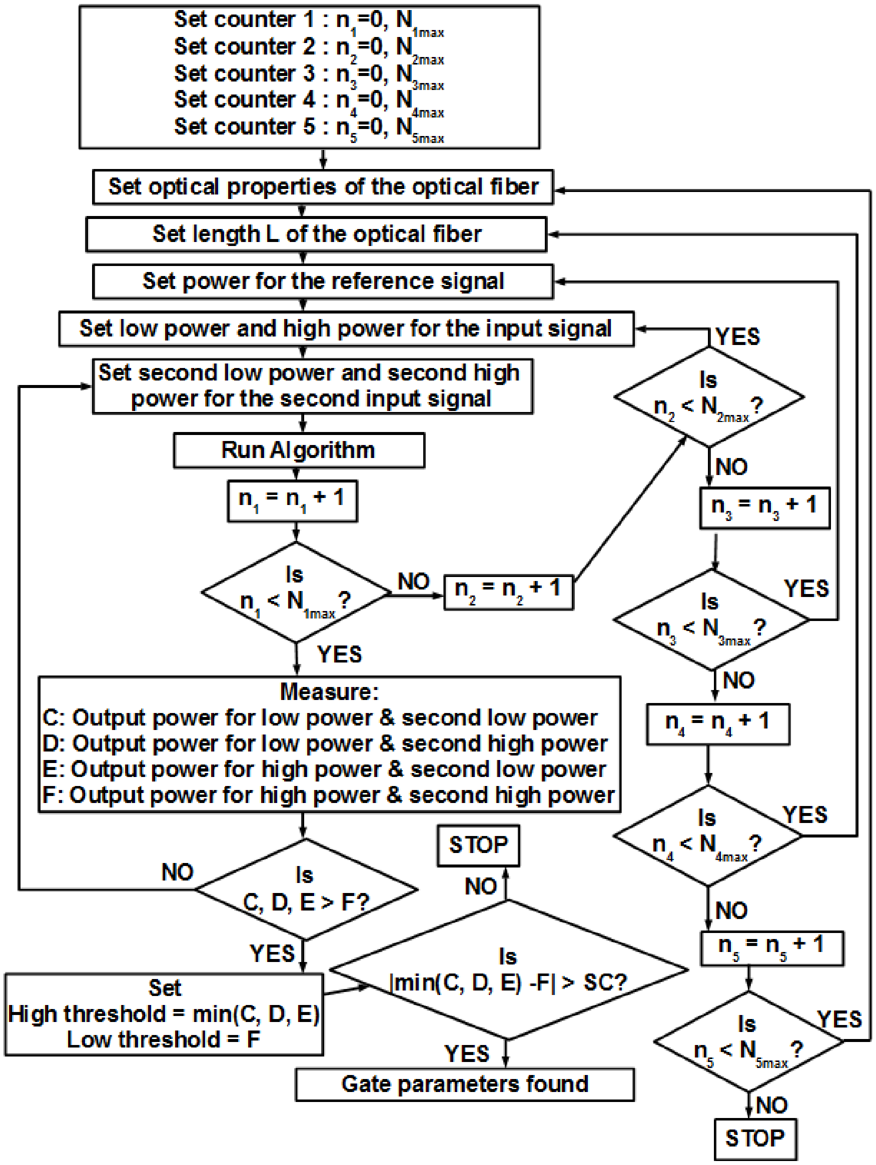

Figure 7.14. Flow chart for NAND gate of Configurations I and II.

For the algorithm of the NAND gates of Configurations I-II, the additional counter added, n_5, is used to take into account the second low power and second high power of the second input signal. ‘C,’ ‘D,’ ‘E,’ and ‘F’ are denoted as the output powers for the effective input combinations of ‘0 0,’ ‘0 1,’ ‘1 0,’ and ‘1 1’, which are simulated by the combination of low power and second low power, low power and second high power, high power and second low power, and high power and second high power. For the NAND gate, for which the corresponding outputs should be ‘1,’ ‘1,’ ‘1,’ and ‘0’ respectively, C, D, E are evaluated in comparison to F. If C, D, E > F by a value greater than the switching contrast, ‘SC,’ then the smallest of C, D, E are set as the high threshold, and F is set as the low threshold. Otherwise, the counters are increased and the algorithm continues to ‘sift’ through other parameters of the fiber.

7.8.4 Configuration III: NAND gate

For the NAND gate of Configuration III, which has frequency detuning, we have the following flow chart, shown in Figure 7.15 below.

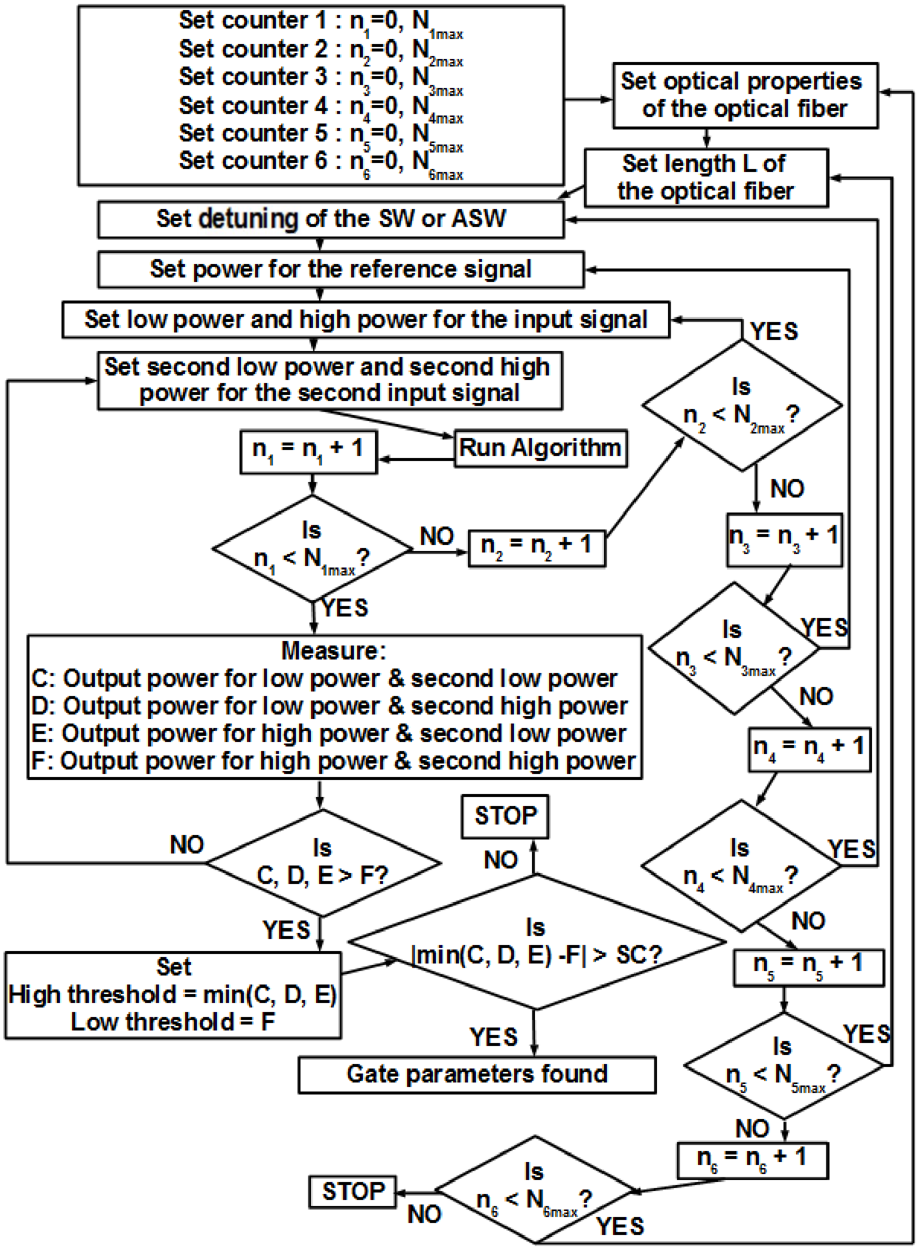

Figure 7.15 Flow chart for NAND gate of Configuration III.

In the algorithm of the NAND gate of Configuration III, an additional counter is added, n_6, with maximum N_{6max}, to take into account the detuning of the Stokes or anti-Stokes waves. The rest of the algorithm remains unchanged as compared to the NAND gates of Configurations I-II.

7.8.5 *3D parametric model* applications in photonic logic

An additional important application of the *3D parametric model* of Chapter 3 is in photonic logic. In section 7.5.2, the construction of an optical NOT gate of Configuration V, utilizing the mechanisms of SBS, has been described. To obtain a high switching contrast of 77.6%, such as the one obtained in section 7.5.2, it is important to find the correct combination of fiber parameters. The initial Stokes power, P_{SW}, was chosen to be the input signal, and an output CW power, $P_{pump\text{-}out}$,was taken to be the output signal of the optical gate. The input CW power was taken to be the reference signal, and was held constant at P_{pump}=10mW. An input power of 0.1mW was assigned a logical value of "0," while an input power of 10mW was assigned a logical value of "1." Output powers of 9.0mW and 1.33mW were obtained for the logical inputs "0" and "1," respectively, yielding the switching contrast of 77.6%. In the configuration described in Section 7.5.2, a SNF-28 fiber was used, of length 350m, and a 1550nm laser.

The Brillouin surface can be used to reconstruct this optical gate for any combination of parameters, not only for the ones used in Section 7.5.2. For example, it is possible to reproduce the optical logic gate of Section 7.5.2 for the SMF-28e fiber, 1310nm laser, and 1000m fiber, used in Chapter 3, by referring to the Brillouin surface in Figure 3.3. From Figure 3.3, it is seen that a reference input CW beam of 10mW corresponds to β_3=6.4, hence all combinations of parameters must be on the parametric curve corresponding to β_3=6.4. Furthermore, the output CW power of $P_{pump\text{-}out}$=1.33mW, corresponding to the "0" output, in turn corresponds to β_1=0.88. For the parameters taken in this manuscript, this yields an input Stokes power of P_{SW}=1.4mW. Likewise, the output CW power of $P_{1\text{-}out}$=9.0mW, corresponding to the "1" output, in turn corresponds to β_1=0.002. Again, for the parameters taken in this manuscript, this yields an input Stokes power of P_{SW}=0.003mW. Hence, just by looking at the Brillouin surface in Figure 3.3, it is possible to find the combination of parameters of the fiber, to re-create the optical logic gate described in section 7.5.2. Of course, the *3D parametric model* may also be used to construct an optical gate with a higher switching contrast than the one disclosed in section 7.5.2, or for different, more practical, input powers.

7.9 Proposed Experimental Configurations

7.9.1 Configurations I-V

A proposed experimental setup to test the functionality of the NAND/NOT gates proposed in sections 7.4-7.5 is shown in Figure 7.16(a) below. Similar to the ODPA-BOTDA sensor described in [65], the current experimental setup has a DFB laser with a wavelength at 1550nm and an output power which may be varied from 10-40mW. The output light from DFB laser is split into two parts by a fiber coupler CC1. One part works as a CW and is sent to the fiber directly. An EDFA1 is used to vary the power of this CW light wave. The other part is modulated by an EOM1 to generate two side bands with optical carrier suppressed. A circulator C1 and an FBG1 is applied to separate the upper side band and lower side band. Two optical pulse widths are generated by two EOMs (EOM2 and EOM3) after the FBG1, EDFA2 and EDFA3 are used to control the power of each wave individually. After the generation of the SW and ASW pulses, fiber coupler CC2 is used to combine the two pulses together, after which the combined SW and ASW were sent to the testing fiber. After passing through the fiber, a circulator C2 relays the combined SW and ASW to another FBG2, which filters out the desired ASW signal, after which an AC coupled photo detector is used to detect the ASW signal.

In the case of a NAND gate of Configurations I-III, the input signals are controlled by EDFA1 and EDFA3, which regulate the initial CW and SW powers respectively, while EDFA2 is used to keep the power of the initial ASW constant (10mW). In the case of the NOT gate of Configuration IV, the input signal is controlled by EDFA1, while EDFA2 and EDFA3 are used to keep the powers of the initial SW and ASW constant (10mw) respectively. For both gates, the output ASW signal is measured at the photo detector.

For the case of the NOT gate of Configuration V, which requires only a CW and SW, the proposed experimental setup is shown in Figure 7.16(b). EOM1 acts to create only one sideband with optical carrier suppressed, and the EDFA2 acts to control the power of the resulting SW. In this case, circulator C2 is moved to the opposite end of the optical fiber, and the output CW wave is measured by the photo detector.

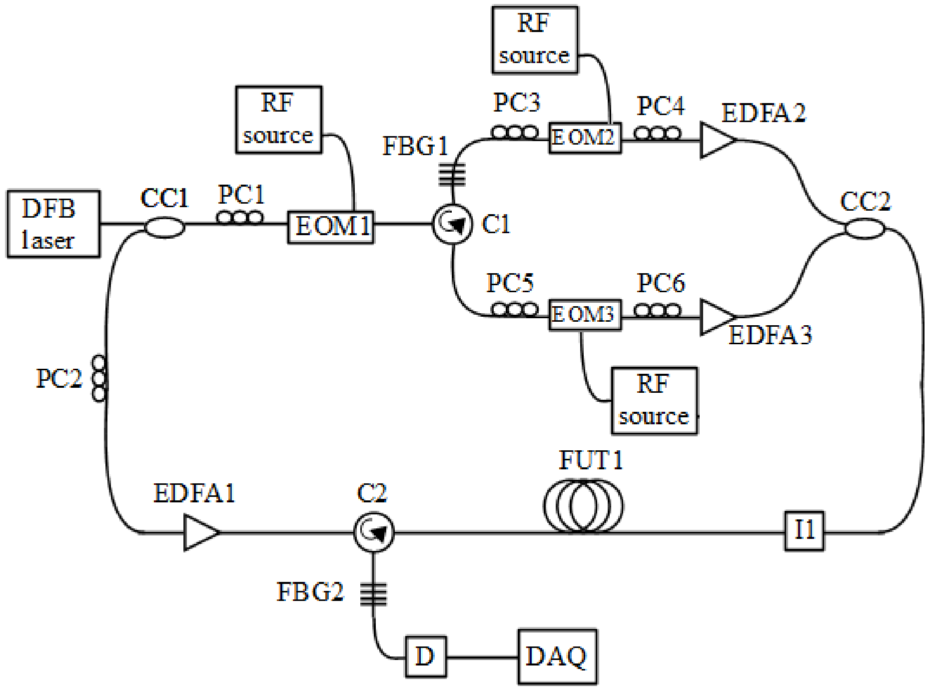

(a)

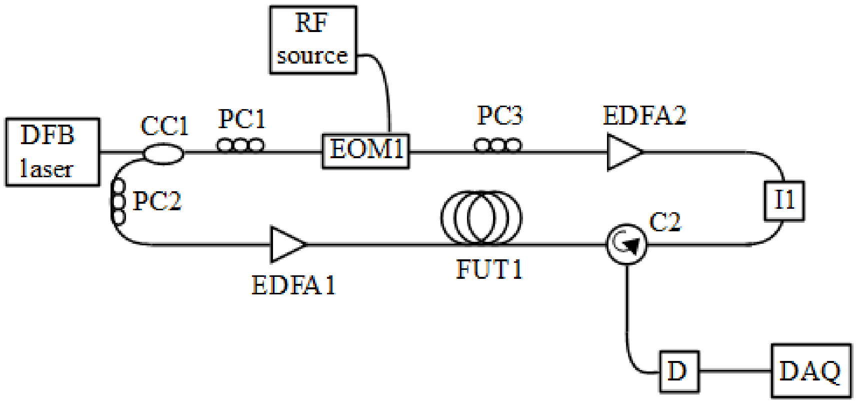

(b)

Figure 7.16 NOT experimental setup for test of NAND/NOT gates.

(a) Configurations I-IV, (b) Configuration V.

DFB: Distributed Feedback, RF: radio frequency, C: circulator, CC: fiber coupler,

FUT: fiber under test, I: isolator, EOM: Electro-Optic Modulator, FBG: Fiber Bragg Grating,

PC: polarization controller, EDFA: Erbium-doped fiber amplifier, DAQ: Data Acquisition.

7.9.2 Configurations VI

In the current configuration, an AND gate is constructed by connecting the NAND gate of Configuration III with the NOT gate of Configuration IV, shown in Figure 7.17 below.
Similar to Figure 7.16, the signal from the DFB laser is split by circulator C1 into a SW and ASW via FBG1, while EOM2 and EOM3 detune the SW and ASW signals individually. In this case, before the two waves are recombined, couplers CC4 and CC5 redirect the SW and ASW, to later act as reference signals for the NOT gate. EDFA5 and EDFA4 are used to control the power of the redirected SW and ASW waves respectively, keeping them constant (10mW). The NAND gate is represented by the first fiber under test (FUT1). The output ASW from FUT1, $P_{3\text{-}out}$, after being separated from its output SW counterpart by FBG3, is passed through a ring resonator RR1 which is utilized to downshift the frequency of the ASW from ω_3 to ω_1, which is the frequency of the CW. The resulting converted CW wave acts as an input signal for the NOT gate, represented by FUT2. Reference signals ASW and SW are recombined by coupler CC6 and injected into FUT2 from the opposite end, and as previously, the output ASW is filtered by FBG4 before being measured by the photo detector.

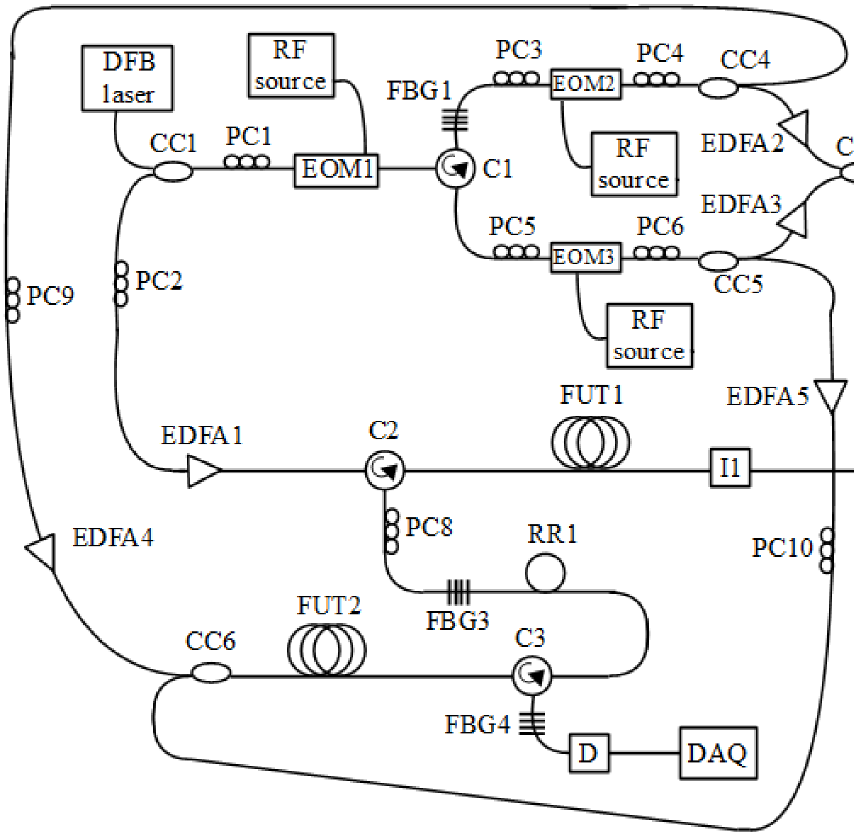

Figure 7.17 Configuration VI: AND gate.
DFB: Distributed Feedback, RF: radio frequency, C: circulator, CC: fiber coupler,
RR: ring resonator, FUT: fiber under test, I: isolator, EOM: Electro-Optic Modulator,
FBG: Fiber Bragg Grating, PC: polarization controller, EDFA: Erbium-doped fiber amplifier,
DAQ: Data Acquisition.

Similar to Figure 7.16(a), EDFA1 and EDFA3 control the input signals of the AND gate, P_{10} and P_{20}, while EDFA2 is used to keep the power of the initial ASW constant (10mW). The output ASW from FUT2 is measured by the photo detector.

7.9.3 Configurations VII

In the current configuration, an AND gate is constructed by connecting the NAND gate of Configuration III with the NOT gate of Configuration V, shown in Figure 7.18 below. The dotted lines represent extension to the experimental setup of Figure 7.16(a).

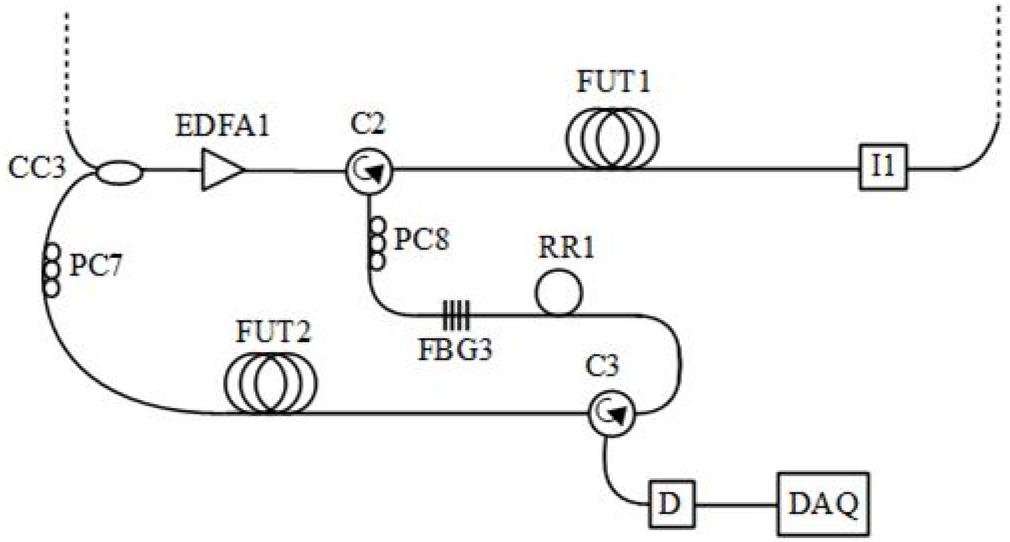

Figure 7.18 Configuration VII: AND gate.
DFB: Distributed Feedback, RF: radio frequency, C: circulator, CC: fiber coupler,
RR: ring resonator, FUT: fiber under test, I: isolator, EOM: Electro-Optic Modulator,
FBG: Fiber Bragg Grating, PC: polarization controller, EDFA: Erbium-doped fiber amplifier,
DAQ: Data Acquisition.

In this configuration, the output ASW, $P_{3\text{-}out}$, after being filtered by FBG3, is passed through a ring resonator RR1, which downshifts the frequency of the optical signal from ω_3 to ω_2, which is the frequency of the SW. The resulting converted SW wave acts as an input signal for the NOT gate, represented by FUT2. A CW reference signal is injected into FUT2 from the opposite end. The output CW signal from FUT2 is measured by the photo detector.

In this case, EDFA1 and EDFA3 (Figure 7.16(a)) are used to regulate the input signals of the AND gate, P_{10} and P_{20}, while the output CW from FUT2 is measured by the photodetector.

7.9.4 Configurations IX

To create a functional OR gate of Configuration IX, three NAND gates from Configuration III must be connected, shown in Figure 7.19 below. In this case, FUT1, FUT2 and FUT3 represent the three NAND gates, NAND1, NAND2 and NAND3 respectively. In this case, both inputs to NAND1 and NAND2 are identical. For this reason, the power of the CW and SW signals, which is controlled by attenuators EDFA1 and EDFA3, for NAND1, and EDFA7 and EDFA8, for NAND2, must be made identical. Similar to Figure 7.17, before the generated SW and ASW are recombined by a coupler CC2, another coupler CC4 is used redirect the ASW, to later act as reference signals for the NAND3. The output ASW from NAND1 is passed through ring resonator RR1, which downshifts its frequency from ω_3 to ω_1, which is the frequency of the CW. The resulting converted CW wave acts as an input signal for NAND3. The output ASW from NAND2 is passed through ring resonator RR2, which downshifts its frequency from ω_3 to ω_2, which is the frequency of the SW. The resulting converted SW wave acts as the second input signal for NAND3, and is injected into FUT3 at the opposite end, after being recombined with the redirected ASW by coupler CC7. The output ASW signal from FUT3 from is then filtered by FBG4 and measured by the photo detector.

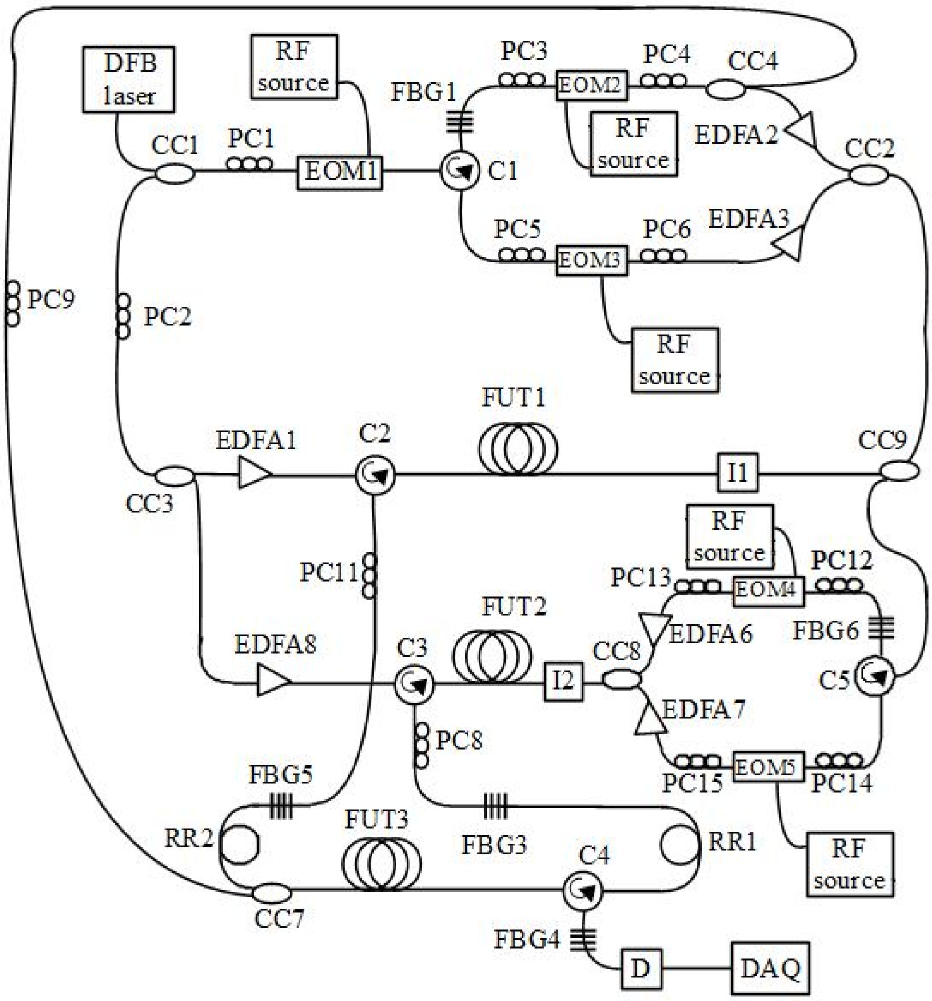

Figure 7.19 Configuration IX: OR gate.
DFB: Distributed Feedback, RF: radio frequency, C: circulator, CC: fiber coupler,
RR: ring resonator, FUT: fiber under test, I: isolator, EOM: Electro-Optic Modulator,
FBG: Fiber Bragg Grating, PC: polarization controller, EDFA: Erbium-doped fiber amplifier,
DAQ: Data Acquisition.

In this case, EDFA1 and EDFA3, and EDFA7 and EDFA8, are used to regulate the input signals of the AND gate, while the output ASW from FUT3 is measured by the photo detector.

The same detuning must be applied to optical signals entering FUT1 (NAND gate 1), FUT2 (NAND gate 2) and FUT3 (NAND gate 3), as described in Table 3 of Configuration III. To accomplish this, combined SW and ASW signals by coupler CC2 are split by coupler CC9 into two paths, one path is injected into FUT1, while the SW and ASW signals on the second path are split by circulator C5 and separated by FBG6. In this way, it is possible to detune the SW and ASW separately by EOM4 and EOM5, such that the resulting recombined signals by coupler CC8 are detuned accordingly, before being injected into FUT2.

7.9.5 Configurations X

The setup to create a functional OR gate of Configuration X is very similar to that of Configuration IX depicted in Figure 7.19. The difference is that two NOT gates of Configuration IV and one NAND gate from Configuration III must be connected. Keeping this difference in mind, it follows that FUT1 and FUT2 represent the two NOT gates, NOT1 and NOT2 respectively, and FUT3 represents the NAND gate, NAND3 respectively. In this case, only one input to NOT1 and NOT2 exist, which are the CW signals controlled by attenuators EDFA1 for NOT1 and EDFA8 for NOT2. The ASW and SW reference signals, which are controlled respectively by attenuators EDFA2 and EDFA3 for NOT1, and EDFA6 and EDFA7 for NOT2, are kept constant at 10mW. Similar to Figure 7.17, before the generated SW and ASW are recombined by a coupler CC2, another coupler CC4 is used redirect the ASW, to later act as reference signals for the NAND3. The output ASW from NOT1 is passed through ring resonator RR1, which downshifts its frequency from ω_3 to ω_1, which is the frequency of the CW. The resulting converted CW wave acts as an input signal for NAND3. The output ASW from NOT2 is passed through ring resonator RR2, which downshifts its frequency from ω_3 to ω_2, which is the frequency of the SW. The resulting converted SW wave acts as the second input signal for NAND3, and is injected into FUT3 at the opposite end, after being recombined with the redirected ASW by coupler CC7. The output ASW signal from FUT3 from is then filtered by FBG4 and measured by the photo detector.

7.9.6 Configurations XI

The setup to create a functional OR gate of Configuration XI is comprised of two NOT gates of Configuration V and one NAND gate from Configuration III. To realize this setup, the experimental setups from Figure 7.16(b) must be combined with the experimental setup of 7.16(a), shown below in Figure 7.20. In this case, FUT1 and FUT2 represent the two NOT gates, NOT1 and NOT2 respectively, and FUT3 represents the NAND gate, NAND3 respectively. In this case, only one input to NOT1 and NOT2 exist, which are the SW signals controlled by attenuators EDFA3 for NOT1 and EDFA7 for NOT2. The CW reference signals, which are controlled respectively by attenuators EDFA1 for NOT1, and EDFA8 NOT2, are kept constant at 10mW. Since the NOT gates in this setup are *2-wave* NOT gates, the SW and ASW waves are no longer recombined by a coupler CC2, the ASW is simply redirected to later act as a reference signal for the NAND3. The output CW from NOT1 is passed directly to the FUT3, the redirected CW wave acts as an input signal for NAND3. The output CW from NOT2 is passed through ring resonator RR1, which downshifts its frequency from ω_1 to ω_2, which is the frequency of the SW. The resulting converted SW wave acts as the second input signal for NAND3, and is injected into FUT3 at the opposite end, after being recombined with the redirected ASW by coupler CC7. The output ASW signal from FUT3 from is then filtered by FBG4 and measured by the photo detector.

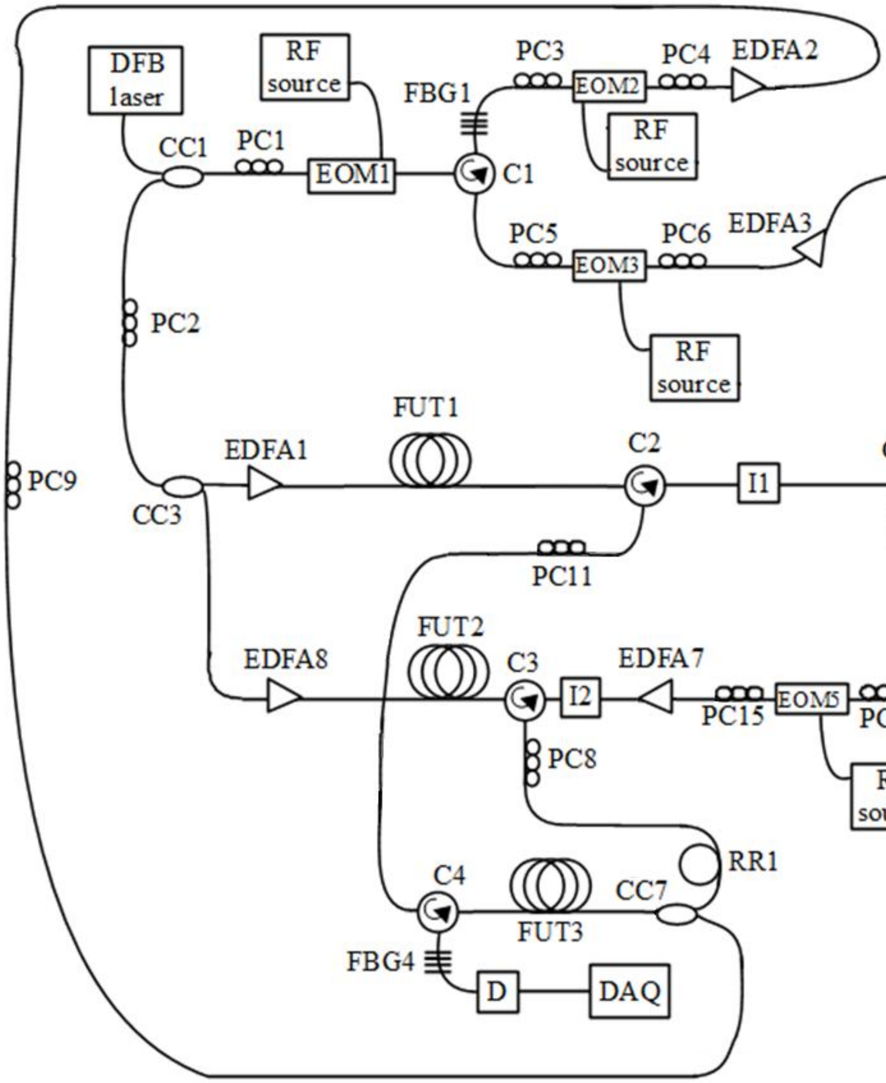

Figure 7.20 Configuration XI: OR gate.
DFB: Distributed Feedback, RF: radio frequency, C: circulator, CC: fiber coupler,
RR: ring resonator, FUT: fiber under test, I: isolator, EOM: Electro-Optic Modulator,
FBG: Fiber Bragg Grating, PC: polarization controller, EDFA: Erbium-doped fiber amplifier,
DAQ: Data Acquisition.

In this case, EDFA3 and EDFA7, are used to regulate the input signals of the AND gate, while the output ASW from FUT3 is measured by the photo detector.

7.10 Bit rate

Because optical gates based on the process of SBS, or combined Brillouin gain and loss, are limited by a phonon relaxation time of about 10ns, and because of the narrowband characteristic of Brillouin amplification, the bit rate of the Brillouin signal is limited to tens of megabits per second [101, 102]. However, there are a number of techniques aimed at increasing the Brillouin gain bandwidth, thereby supporting a higher bit rate. These include a simple pump-spectral broadening technique [103, 104] via direct- modulation of the pump laser using a pseudorandom binary sequence (PRBS) data, a Gaussian noise source. Alternatively, the pump wave can be broadened by using an external phase modulator (PM), which has been demonstrated to yield bit rates between 1-2.5 Gb/s [101, 105]. Comparatively, bit rates between 10 Gb/s to 100 Gb/s have been claimed by other technologies to construct optical logic units [37, 43, 49, 51, 106, 107]. Though these alternative constructions have higher bit rates, they also include numerous drawbacks, including configurations which are both bulky and require extensive calibration, and fall victim to spontaneous emission noise, time dependent modulation due to time jitter, and birefringence induced signal distortion. The technique based on combined Brillouin gain and loss, disclosed in this chapter, is free of polarization-induced signal fluctuations which cause spectral distortion, thereby making the lower bit rate a worthy trade-off.

7.11 Summary

A novel fiber nonlinearity-based technique has been proposed to realize all-optical NAND/NOT/AND/OR logic gates, based on the principles of combined Brillouin gain and loss in a PMF. Switching contrasts are simulated to be between 20-83%, for various configurations. In addition, the technique is not limited by polarization instabilities or PMD. Additionally, a general method for constructing optical gates has been proposed in the form of an algorithm.

Finally, experimental configurations have been proposed to realize the optical logic gates of Configurations I-XI.

Chapter 8

Conclusion

8.1 Thesis Outcomes

The main focus of the research presented in this thesis was on the theoretical investigation of stimulated Brillouin scattering (SBS), as well as combined Brillouin gain and loss, in optical fibers and their application to current technologies in fiber sensing, photonic logic, and telecommunications.

Experimentally verified fully analytic expressions have been obtained for the Brillouin amplification process without any underlying assumptions about the behaviour of the pump or pulse waves. Additionally, for the first time, analytic solutions for the output pump and Stokes spectra have been obtained to good accuracy, as well as an expression for the *FWHM*, which have been confirmed experimentally. In sensing applications, the *3D parametric model* may be used to avoid parameter combinations which yield the unwanted spectral distortion effect, such as in distributed sensing where pump depletion is substantial. The *3D parametric model* can also be used to classify the similarity between various Brillouin amplification processes, making it possible to obtain the same pump or Stokes output intensity with a different collection of parameters of the fiber. This, in particular, has useful applications in the construction of all-optical logic gates.

Regarding applications in telecommunications, the SBS process has been used to develop an improved method of phase-modulation, and applied in the conceptualization of an optical phase-modulator based on the principles of SBS, as well as an optical phase network employing the same.

Polarization and birefringence effects on SBS, and combined Brillouin gain and loss, in an optical fiber have been investigated. The most general model of elliptical birefringence in an optical fiber has been developed and extended to describe a transient Brillouin interaction including gain, loss, and combined gain and loss. The subsequent investigation of SBS spectral distortion effects, caused by the birefringence and polarization of the optical fiber, showed that these effects can be used for measuring the degree of non-ideally linearly polarized light, finding regimes which are preferable for measurement in fiber sensing, and for preserving the full width at half maximum (*FWHM*) and pulse fidelity of the Brillouin spectral shape, which has applications in telecommunications and data transmission. In the combined Brillouin gain and loss regime, it has been shown that the spectral distortion caused by birefringence can be minimized by choosing pump and pulse powers with a large disparity, thereby increasing the ease of operation of the optical differential parametric amplification in optical differential parametric amplification (ODPA-BOTDA) systems.

Finally, the theory of combined Brillouin gain and loss has been employed to propose a novel fiber nonlinearity-based technique to realize all-optical NAND/NOT/AND/OR logic gates in polarization-maintaining fibers (PMF). Switching contrasts are simulated to be between 20-83% for various configurations. In addition, the technique is not limited by polarization instabilities or PMD. Finally, experimental configurations have been proposed to realize the optical logic gates.

8.2 Future Work

Future research directions could include the experimental verification of the theoretical works presented in this thesis. Namely, experimental confirmation of the optical phase-modulator of Chapter 4, as well as the optical network employing the optical phase-modulator, would be a logical next step in the development of this technology.

For the all-optical logic gates proposed in Chapter 7, an interesting avenue for research could include the use of chalcogenide fibers in place of silica fibers to realize the all-optical gates. Chalcogenide fibers are characterized by pronounced optical nonlinearities. Compared to silica, for example, the nonlinear refractive index of As_2S_3 glass is about 1000 larger [61, 108, 109, 110, 111, 112], and the Brillouin gain coefficient was reported to be between 100-600 times larger than in fused silica [108, 111]. As a result, a comparable gain may be accomplished in chalcogenide fibers of a few meters as compared to silica fibers of hundreds of meters, which would greatly compactify the setups described in Chapter 7. Additionally, the *3D parametric model* may be used to characterize this new chalcogenide optical gate, as described in section 7.8.5. Furthermore, realization of the experimental configurations proposed in section 7.9, as well as performing multiple-gate connections, would be an important next step in the development of the photonic logic technology.

Regarding the theoretical investigation of polarization and birefringence effects, additional studies could be performed to investigate the effects of a non-uniform fiber on spatial resolution, by simulating different sound velocities for different segments of the optical fiber. Additionally, it would also be interesting to see the spectral evolution as a function of coordinate inside the optical fiber, z. It has been shown experimentally [113] that a spectral "oscillation" occurs inside the fiber; future work could include modeling this behaviour theoretically and seeing how the spatial period of these oscillations is related to the PMD and beat length of the fiber. Additionally, experimental verification of the current theory could be performed by inducing elliptical birefringence in a PMF fiber by twisting it in a controlled way and performing measurements on the twisted fiber.

Bibliography

[1] R. Boyd, *Nonlinear Optics*, second ed., Academic Press, New York, 1992.

[2] P. Bayvel, P.M. Radmore, "Solutions of the SBS equations in single mode optical fibers and implications for fibre transmission systems," Electronics Letters **26**, 434-436 (1990).

[3] E. Geinitz, S. Jetschke, U. Röpke, S. Schröter, R. Willsch and H. Bartelt, "The influence of pulse amplification on distributed fibre-optic Brillouin sensing and a method to compensate for systematic errors," Measurement Science and Technology **10**, 112-116 (1999).

[4] X. Bao, L. Chen, "Recent Progress in Distributed Fiber Optic Sensors," Sensors **12**, 8601-8639 (2012).

[5] S. L. Zhang, J. J. O'Reilly, "Effect of Stimulated Brillouin Scattering on Distributed Erbium-Doped Fiber Amplifier," IEEE Photonics Techonology Letters **5**, 537-539 (1993).

[6] B. Foley, M. L. Dakss, R. W. Davies, P. Melman, "Gain Saturation in Fiber Raman Amplifiers Due to Stimulated Brillouin Scattering," J. of Lightwave Technology **7**, 2024-2032 (1989)

[7] F. S. Gokhan, "Moderate-gain Brillouin amplification: An analytical solution below pump threshold," Optics Communications **284**, 4869-4873 (2011).

[8] C. L. Tang, "Saturation and Spectral Characteristics of the Stokes Emission in the Stimulated Brillouin Process," J. of Applied Physics **37**, 2945-2955 (1966).

[9] L. Chen, X. Bao, "Analytical and Numerical Solutions for Steady State Stimulated Brillouin Scattering in a Single-mode Fiber," Optics Communications **152**, 65-70 1998).

[10] A. Kobyakov, S. Darmanyan, M. Sauer, D. Chowdhury, "High-gain Brillouin amplification: an analytical approach," Optics Letters 31, 1960-1962 (2006).

[11] A. Chen, E. Murphy, *Broadband Optical Modulators: Science, Technology, and Applications*, first ed., CRC Press, Boca Raton, 2012.

[12] R. Hui, M. O'Sullivan, *Fiber Optic Measurement Techniques*, first ed., Elsevier Academic Press, Burlington, 2009.

[13] M. M. Rao, *Optical Communication*, first ed., Universal Press, Hyderguda, 2000.

[14] J. N. Downing, *Fiber-optic Communications*, first ed., Thomson Delmar Learning, Clifton Park, 2005.

[15] C. DeCusatis, I. P. Kaminow, *The Optical Communications Reference*, first ed.,

Academic Press, Oxford, 2010.

[16] P. E. Powers, *Fundamentals of Nonlinear Optics*, first ed., CRC Press, Boca Raton, 2011.

[17] Y. S. Kuz'minov, *Lithium Niobate Crystals*, first ed., Cambridge International Science Publishing, Cambridge, 1999.

[18] R. Hui, Q. Jiang, M. Kavehrad, T. Makino, “All-optical phase modulation in a traveling wave semiconductor laser amplifier”, IEEE Photonics Technology Letters **6**, 808-810 (1994).

[19] D. R. Walker, M. Bashkanski, A. Gulian, F. K. Fatemi, M. Steiner, "Stabilizing slow light delay in stimulated Brillouin scattering using a Faraday rotator mirror," JOSA B **25**, C61-C64 (2008).

[20] L. Thevenaz, "Slow and Fast Light in Optical fibers,"Nature Photonics **2**, 474-481 (2008).

[21] G. M. Gehring, R. W. Boyd, A. L. Gaeta, D. J. Gauthier, A. E. Willner, "Fiber-based Slow-Light Technologies," J. of Lightwave Technology **26**, 3752-3762 (2008).

[22] R. H. Stolen, "Polarization Effects in Fiber Raman and Brillouin Lasers," J. of Quantum Electronics **QE-15**, 1157-1160 (1979).

[23] O. Shlomovits, M. Tur, "Vector analysis of depleted stimulated Brillouin scattering amplification in standard single-mode fibers with non-zero birefringence," Optics Letters **38**, 836-838 (2013).

[24] L. Ursini, M. Santagiustina, L. Palmieri, "Polarization-Dependent Brillouin Gain in Randomly Birefringence Fibers," IEEE Photonics Technology Letters **22**, 712-714 (2010).

[25] M. Oskar van Deventer, A. J. Boot, "Polarization Properties of Stimulated Brillouin Scattering in Single-Mode Fibers," J. of Lightwave Technology **12**, 585-590 (1994).

[26] W. Zou, Z. He, K. Hotate, "Complete discrimination of strain and temperature using Brillouin frequency shift and birefringence in a polarization-maintaining fiber," Optics Express **17**, 1248-1255 (2009).

[27] A. Zadok, A. Eyal, M. Tur, "Polarization attributes of stimulated Brillouin scattering slow light in fiber," Proc. of SPIE **7949**, 79490A (2011).

[28] S. Xie, M. Pang, X. Bao, L. Chen, “Polarization dependence of Brillouin linewidth and peak frequency due to fiber inhomogeneity in single mode fiber and its impact on distributed fiber Brillouin sensing,” Opt Express **20**, 6385-6399 (2012) .

[29] L. Thevenaz, M. Facchini, A. Fellay, M. Nikles, P. Robert, "Evaluation of local

birefringence along fibres using Brillouin analysis," Optical Fibre Measurement Conference OFMC'97,82-85 (1997).

[30] A. Zadok, S. Chin, L. Thevenaz, E. Zilka, A. Eyal, M. Tur, "Polarization-induced distortion in stimulated Brillouin scattering slow-light systems," Optics Letters **34**, 2530-2532 (2009).

[31] T. Chattopadhyay, “Optical programmable Boolean logic unit,” Applied Optics **52**, 6049-6056 (2011).

[32] T. Chattopadhyay, “Optical reversible programmable Boolean logic unit,” Applied Optics **51**, 5266-5271 (2012).

[33] M. R. Fetterman, "Design for high-speed optoelectronic Boolean logic," IEEE Photonics Technology Letters **21**, 1740-1742 (2009).

[34] J. Yang, X. Li, J. Yang, J. Liu, X. Su, "Polarization-independent bidirectional 4 x 4 optical switch in free-space," Optical Laser Technology **43**, 927-933 (2010).

[35] Y. Wu, T. Shih, M. Chen, “New all-optical logic gates based on the local nonlinear Mach-Zehnder interferometer,” Optics Express **16**, 248-257 (2008).

[36] M. Nazari, M. Haghparast, “Novel design of all-optical reversible logic gate using Mach-Zehnder interferometer in the field of nanotechnology,” Australian J. of Basic and Applied Science **5**, 923-929 (2011).

[37] T. Chattopadhyay, “All-optical modified Fredkin gate,” IEEE J. of Selected Topics in Quantum Electronics **18**, 585-592 (2012).

[38] Z. Li, G. Li, “Ultrahigh speed reconfigurable logic gates based on four-wave mixing in a semiconductor optical amplifier,” Photonics Technology Letters **18**, 1341-1343 (2006).

[39] S. H. Kim, J. H. Kim, B. G. Yu, Y. T. Byun, Y. M. Jeon, S. Lee, D. H. Woo, S. H. Kim, “All-optical NAND gate using cross-gain modulation in semiconductor optical amplifiers,” Electronics Letters **41**, 1027-1028 (2005).

[40] D. Nesset, T. Kelly, D. Marcenac, "All-optical wavelength conversion using SOA nonlinearities," IEEE Communications Magazine **36**, 56-61 (1998).

[41] C. Schubert, R. Ludwig, H-G. Weber, “High-speed optical signal processing using semiconductor optical amplifiers," J. of Optical and Fiber Communication Research Reports **2**, 171-208 (2004).

[42] X. Ye, P. Ye, M. Zhang, “All-optical NAND gate using integrated SOA-based Mach-Zehnder interferometer,” Optical Fiber Technology **12**, 312-316 (2006).

[43] T. Chattopadhyay, “All-optical programmable Boolean logic unit using SOA-MZI switch,” IET Optoelectronics **5**, 270-280 (2011).

[44] K. I. Kang, T.G. Chang, I. Glesk, P. R. Prucnal, "Comparison of Sagnac and Mach-Zehnder ultrafast all-optical interferometric switches based on semiconductor resonant optical nonlinearity," Applied Optics **35**, 417-426 (1996).

[45] J. Y. Kim, J. M. Kang, T. Y. Kim, S. K. Han, "All-optical multiple logic gates with XOR, NOR, OR and NAND functions using parallel SOA-MZI structures: theory and experiment," J. of Lightwave Technology **24**, 3392-3399 (2006).

[46] J. Wang, J. Sun, Q. Sun, “Experimental observation of a 1.5μm band wavelength conversion and logic NOT gate at 40 Gbit/s based on sum-frequency generation,” Optics Letters **31**, 1711-1713 (2006).

[47] J. Wang, J. Sun, Q. Sun, “Proposal for all-optical switchable OR/XOR logic gates using sum-frequency generation,” IEEE Photonics Technology Letters **19**, 541-543 (2007).

[48] Z. Y. Shen, L. L.Wu, “Reconfigurable optical logic unit with terahertz optical asymmetric demultiplexer and electro optic switches,” Applied Optics **47**, 3737-3742 (2008).

[49] T. Chattopadhyay, “Eliminating the additional input beam in all-optical XOR gate using Terahertz Optical Asymmetric Demultiplexer (TOAD) based interferometer: A theoretical analysis,” Optik International J. for Light and Electron Optics **122**, 1486–1491 (2011).

[50] T. Chattopadhyay, “All-optical terahertz optical asymmetric demultiplexer (TOAD) based binary comparator: a proposal,” J. of Nonlinear Optical Physics & Materials **18**, 471-480 (2009).

[51] T. Chattopadhyay, “All-optical cross-bar network architecture using TOAD based interferometric switch and using it to design reconfigurable logic unit,” Optical Fiber Technology **17**, 558-567 (2011).

[52] A. W. Lohmann, “Polarization and optical logic,” Applied Optics **25**, 1594-1597 (1986).

[53] M. A. Karim, A. A. S. Awwal, A. K. Cherri, “Polarization-Encoded Optical Shadow-Casting Logic Units: Design,” Applied Optics **26**, 2720-2725 (1987).

[54] T. Chattopadhyay, T. Sarkar, “All-optical by Kerr nonlinear prism and its application to of binary-to-gray-to-binary code conversion,” Optics & Laser Technology **44**, 1722-1728 (2012).

[55] C. Yu, L. Christen, T. Luo, Y. Wang, Z. Pan, L. Yan, A. E. Willner, “All-optical XOR gate using polarization rotation in single highly nonlinear fiber,” Photonics Technology Letters **17**, 1232-1234 (2005).

[56] C. Yu, L. Christen, T. Luo, Y. Wang, Z. Pan, L. Yan, A. E. Willner, “All-optical XOR gate based on Kerr effect in single highly-nonlinear fiber,” Proc. of Conf. Lasers and Electro-Optics (CLEO), 3-5 (2004).

[57] K. Suzuki, H. Kubota, S. Kawanishi, M. Tanaka, M. Fujita, “Optical properties of low-loss polarization-maintaining photonic crystal fiber,” Optics Express **9**, 676-680 (2001).

[58] T. Hosaka, K. Okamoto, T. Miya, Y. Sasaki, T. Edahiro, “Low-loss single polarization fibers with asymmetrical strain birefringence,” Electronics Letters **17**, 530-531 (1981).

[59] R. D. Birch, D. N. Payne, M. P. Varnham, “Fabrication of polarization-maintaining fibers using gas-phase etching,” Electronics Letters **18**, 1036-1038 (1982).

[60] J. D. Jackson, *Classical Electrodynamics*, first ed., John Wiley & Sons, Inc., New York, 1962.

[61] G. P. Agrawal, *Nonlinear Fiber Optics*, third ed., Academic Press, San Diego, 2001.

[62] A. B. Ruffin, "Stimulated Brillouin Scattering: An overview of measurements, system impairments, and applications," NIST Symposium on Optical Fiber Measurements **2**, 23-28 (2004).

[63] A. Kobyakov, M. Sauer, D. Chowdhury, “Stimulated Brillouin scattering in optical fibers,” Advances in Optics and Photonics **2**, 1-59 (2010).

[64] I. L. Fabelinskii, *Molecular Scattering of Light*, first ed., Plenum Press, Moscow, 1968.

[65] Y. Li, X. Bao, Y. Dong, L. Chen, "A novel distributed Brillouin sensor based on optical differential parametric amplification," J. Lightwave Technology **28**, 2621–2626 (2010).

[66] E. Collette, *Field Guide to Polarization*, first ed., SPIE Press, Washington, 2005.

[67] A. Kumar, A. Ghatak, *Polarization of Light with Applications in Optical Fibers*, first ed., SPIE press, Washington, 2011.

[68] E. Collette, *Polarized Light in Fiber Optics*, first ed., The PolaWave Group, Lincroft, 2003.

[69] A. Rogers, *Polarization in Optical Fibers*, first ed., Artech House Inc., Norwood, 2008.

[70] F. Ravet, *Performance of the Distributed Brillouin Sensor: Benefits and Penalties Due to Pump Depletion*, first ed., University of Ottawa Press, Ottawa, 2007.

[71] T. Horiguchi, K. Shimizu, T. Kurashima, M. Tateda, Y. Koyamada, "Development of a distributed sensing technique using Brillouin scattering," J. of Lightwave Technology **13**, 1296-1302 (1995).

[72] L. Thévenaz, S. F. Mafang, "Depletion in a distributed Brillouin fiber sensor: practical limitation and strategy to avoid it," J. Lin. Proc. of SPIE **7753A5** 1-4 (2011).

[73] A. Minardo, R. Bernini, L. Zeni, L. Thevenaz, F. Briffod, "A reconstruction technique for long-range stimulated Brillouin scattering distributed fibre-optic sensors: experimental results," Measurement Science and Technology **16**, 900-908 (2005).

[74] T. H. Russell, W. B. Roh, "Threshold of second-order stimulated Brillouin scattering in optical fiber," JOSA B **19**, 2341-2345 (2002).

[75] J. W. D. Chi, L. Chao, M. K. Rao, "Time-domain large-signal investigation on nonlinear interactions between an optical pulse and semiconductor waveguides," J. of Quantum Electronics **37**, 1329-1336 (2001).

[76] R. Chu, M. Kanefsky, J. Falk, "Numerical study of transient stimulated Brilllouin scattering," J. of Applied Physics **71**, 4653 - 4658 (1992).

[77] M. Razaghi, V. Ahmadi, M. J. Connelly, "Comprehensive Finite-Difference Time-Dependent Beam Propagation Model of Counterpropagating Picosecond Pulses in a Semiconductor Optical Amplifier," J. of Lightwave Technology **27**, 3162-3174 (2009).

[78] F. S. Gokhan, G. W. Griffiths, W. E. Schiesser, "Method of lines solution to the transient SBS equations for nanosecond Stokes pulses," J. of the European Optical Society **8**, 13049 (2013).

[79] Z. Zhu, D. J. Gauthier, Y. Okawachi, J. E. Sharping, A. L. Gaeta, R. W. Boyd, A. E. Willner, "Numerical study of all-optical slow-light delays via stimulated Brillouin scattering in an optical fiber," JOSA B **22**, 2378-2384 (2005).

[80] C. Zeringue, I. Dajani, S. Naderi, G. T. Moore, C. Robin, "A theoretical study of transient stimulated Brillouin scattering in optical fibers seeded with phase-modulated light," Optics Express **20**, 21196-21213 (2012).

[81] D. Cotter, "Transient Stimulated Brillouin Scattering in long single-mode fibres," Electronics Letters **18**, 504-506 (1982).

[82] V. P. Kalosha, L. Chen, X. Bao, "Slow and fast light via SBS in optical fibers for

short pulses and broadband pump," Optics Express **14**, 12693-12703 (2006).

[83] V. P. Kalosha, E. A. Ponomarev, L. Chen, X. Bao, "How to obtain high spectral resolution of SBS-based distributed sensing by using nanosecond pulses," Optics Express **14**, 2071-2077 (2006).

[84] S. V. Afshar, G. A. Ferrier, X. Bao, L. Chen, "Effect of the finite extinction ratio of an electro-optic modulator on the performance of distributed probe-pump Brillouin sensor systems," Optics Letters **28**, 1418-1420 (2003).

[85] R. Bernini, A. Minardo, L. Zeni, "Dynamic strain measurement in optical fibers by stimulated Brillouin scattering,: Optics Letters **34**, 2613-2615 (2009).

[86] X. Bao, C. Zhang, W. Li, M. Eisa, S. El-Gamal, B. Benmokrane, "Monitoring the distributed impact wave on a concrete slab due to the traffic based on polarization dependence on stimulated Brillouin scattering," Smart Materials and Structures **17**, 1-5 (2008).

[87] V. I. Kovalev, R. G. Harrison, "Observation of Inhomogeneous Spectral Broadening of Stimulated Brillouin Scattering in an Optical Fiber," Physical Review Letters **85**, 1879-1882 (2000).

[88] L. Stepien, S. Randoux, J. Zemmouri, "Origin of spectral hole burning in Brillouin fiber amplifiers and generators," Physical Review A **65**, 053812 (2002).

[89] X. Bao, L. Chen, “Recent Progress in Optical Fiber Sensors based on Brillouin scattering at University of Ottawa,” Photonic Sensors **1**, 102-117 (2011).

[90] H. A. Luther, "An Explicit Sixth-Order Runge-Kutta Formula," Mathematics of Computation **22**, 424-436 (1968).

[91] J. C. Butcher, "On Fifth and Sixth Order Explicit Runge-Kutta Methods: Order Conditions and Order Barriers," Canadian Applied Mathematics Quarterly **17**, 433-445 (2009).

[92] W. Zou, C. Jin, J. Chen, “Distributed Strain Sensing Based on Combination of Brillouin Gain and Loss Effects in Brillouin Optical Correlation Domain Analysis,” Applied Physics Express **5**, 082503 (2012).

[93] K. Y. Song, Z. He, K. Hotate, "Distributed strain measurement with millimeter-order spatial resolution based on Brillouin optical correlation domain analysis," Optics Letters **31**, 2526-2528 (2006).

[94] W. Zou, Z. He, M. Kishi, K. Hotate, "Stimulated Brillouin scattering and its dependences on strain and temperature in a high-delta optical fiber with F-doped depressed inner cladding," Optics Letters **32**, 600-602 (2007).

[95] A. Kumar, *Switching Theory and Logic Design*, first ed., PHI Learning Private

Limited, New Delhi, 2008.

[96] N. J. Doran, D. Wood, “Nonlinear-optical loop mirror,” Optics Letters **13**, 56-58 (1988).

[97] S. H. Larsen, M. E. V. Pedersen, L. Gruner-Nielsen, M. F. Yan, E. M. Monberg, P. W. Wisk, K. Rottwitt, “Polarization Maintaining Higher Order Mode Fiber Module with Anomalous Dispersion at 1μm,” Optics Letters **37**, 4170-4172 (2012).

[98] M. Tur, E. Herman, A. Kozhekin, Y. Danziger, “Stimulated Brillouin Scattering in High-Order Mode fibers employed in dispersion management modules,” IEEE Photon. Technology Letters **14**, 1282-1284 (2002).

[99] A. Bogoni, L. Poti, R. Proietti, G. Meloni, F. Ponzini, P. Ghelfi, “Regenerative and reconfigurable all-optical logic gates for ultra-fast applications,” Electronics Letters **41**, 435-436 (2005).

[100] Y. Miyoshi, R. Ikeda, H. Tobioka, T. Inoue, S. Namiki, K. Kitayama, “Ultrafast all-optical logic gate using a nonlinear optical loop mirror based multi-periodic transfer function,” Optics Express **16**, 2570-2577 (2008).

[101] L. Yi, L. Zhan, W. Hu, Y. Xia, "Delay of Broadband Signals Using Slow Light in Stimulated Brillouin Scattering With Phase-Modulated Pump," IEEE Photonics Technology Letters **19**, 619-621 (2007).

[102] M. Lee, R. Pant, M. A. Neifeld, "Improved slow-light delay performance of a broadband stimulated Brillouin scattering system using fiber Bragg gratings," Applied Optics **47**, 6404-6415 (2008).

[103] M. G. Herraez, K. Y. Song, L. Thevenaz, “Arbitrary-bandwidth Brillouin slow light in optical fibers,” Optics Express **14**, 395–1400 (2006).

[104] Z. Zhu, A. M. C. Dawes, D. J. Gauthier, L. Zhang, A. E. Willner, "12-GHz-bandwidth SBS slow light in optical fibers,” Proc. OFC **PDP1,** 1-3 **(**2006).

[105] L. Yi, L. Zhan, Y. Su, W. Hu, L. Leng, Y. Song, H. Shen, Y. Xia, “Delay of RZ PRBS data based on wideband SBS by phase-modulating the Brillouin pump,” Proc. ECOC **We3.P.30**, 1-2 (2006).

[106] L. Yi, W. Hu, H. He, Y. Dong, Y. Jin, W. Sun, "All-Optical reconfigurable multi-logic gates based on nonlinear polarization rotation effect in a single SOA," Chinese Optics Letters **9**, 030603-1 - 030603-4. (2011).

[107] J. Yang, L. Han, H. Zhang, Y. Guo, " Function-lock strategy in OR/NOR optical logic gates based on cross-polarization modulation effect in semiconductor optical amplifier," Chinese Optics Letters **5**, 566-568 (2007).

[108] S. Levy, V. Lyubin, M. Klebanov, J. Scheuer, A. Zadok, "Stimulated Brillouin scattering amplification in centimeter-long directly written chalcogenide waveguides," Optics Letters **37**, 5112-5114 (2012).

[109] J. L. Adam, X. Zhang, *Chalcogenide Glasses: Preparation, Properties and Applications,* first ed., Woodhead Publishing, New Delhi, India, 2014.

[110] J. S. Sanghera, L. B. Shaw, C. M. Florea, P. Pureza, V. Q. Nguyen, F. Kung, D. Gibson, I. D. Aggarwal, "Nonlinear Properties of Chalcogenide glass fibers," J. of Optoelectronics and Advanced Materials **8**, 2148-2155 (2006).

[111] R. Cherif, A. Salem, M. Zghal, "Full modal analysis of the stimulated Brillouin scattering in As_2S_3 chalcogenide photonic crystal fiber," Proc. Of SPIE **8073**, (2011).

[112] J. S. Sanghera, L. B. Shaw, I. D. Aggarwal, "Applications of Chalcogenide glass optical fibers," Comptes Rendus Chimie **5**, 873-883 (2002).

[113] Y. Li, *Development of the Distributed Brillouin Sensor with High Spatial and Frequency Resolution,* first ed., University of Ottawa Press, Ottawa, 2010.

Appendix

A. Derivation of the system of equations (5.1)-(5.4)

Let us consider the simple case of two propagation constants in the fiber, $\hat{x}$ and $\hat{y}$. If a light with an angular frequency ω was injected into the fiber, the electric fields could be written in the following form, in terms of their principal axis of polarization

$$\left|E_1(z,t)\right\rangle = E_x \exp\{i[k_x z - \omega t]\}\left|\hat{x}\right\rangle + E_y \exp\{i[k_y z - \omega t]\}\left|\hat{y}\right\rangle \qquad \text{(A.1)}$$

Where $\langle\hat{x}|\hat{x}\rangle = 1 = \langle\hat{y}|\hat{y}\rangle$ and $\langle\hat{x}|\hat{y}\rangle = 0$. Considering two counter-propagating beams in the fiber, we can individually write them for the +z-propagating light,

$$\left|E_1(z,t)\right\rangle = E_{1x} \exp\{i[k_{1x} z - \omega_1 t]\}\left|\hat{x}_1\right\rangle + E_{1y} \exp\{i[k_{1y} z - \omega_1 t]\}\left|\hat{y}_1\right\rangle \qquad \text{(A.2)}$$

And the $-z$-propagating light,

$$\left|E_2(z,t)\right\rangle = E_{2x} \exp\{i[-k_{2x} z - \omega_2 t]\}\left|\hat{x}_2\right\rangle + E_{2y} \exp\{i[-k_{2y} z - \omega_2 t]\}\left|\hat{y}_2\right\rangle \qquad \text{(A.3)}$$

The beating via electrostriction in the fiber due to the two light waves can be written explicitly

$$\begin{aligned}\left\langle E_2(z,t)\middle|E_1(z,t)\right\rangle = {} & E_{1x}E_{2x}^{*} \exp\{i[(k_{1x}+k_{2x})z-(\omega_1-\omega_2)t]\}\langle\hat{x}_2|\hat{x}_1\rangle \\ & + E_{1y}E_{2y}^{*} \exp\{i[(k_{1y}+k_{2y})z-(\omega_1-\omega_2)t]\}\langle\hat{y}_2|\hat{y}_1\rangle \\ & + E_{1x}E_{2y}^{*} \exp\{i[(k_{1x}+k_{2y})z-(\omega_1-\omega_2)t]\}\langle\hat{y}_2|\hat{x}_1\rangle \\ & + E_{1y}E_{2x}^{*} \exp\{i[(k_{1y}+k_{2x})z-(\omega_1-\omega_2)t]\}\langle\hat{x}_2|\hat{y}_1\rangle\end{aligned} \qquad \text{(A.4)}$$

In the most general case of elliptical birefringence, we will have $\langle\hat{x}_2|\hat{x}_1\rangle \neq 1 \neq \langle\hat{y}_2|\hat{y}_1\rangle$ and furthermore $\langle \hat{y}_2 | \hat{x}_1 \rangle \neq 0 \neq \langle \hat{x}_2 | \hat{y}_1 \rangle$. The direct physical consequence of this is that there are now four acoustic running waves.

Taking the steady state approximation, we have the complex acoustic field amplitude for the simplest case of zero birefringence, where $\boldsymbol{q}=\boldsymbol{q}_1\approx 2\boldsymbol{k}_1$ as defined in Chapter 2:

$$\Delta\rho = \frac{\gamma_e q^2}{\Omega_B^2 - \Omega_1^2 - i\Gamma_B\Omega_1} \langle E_2(z,t) | E_1(z,t) \rangle \tag{A.5}$$

To generalize the result to the case of elliptical birefringence, where it is expected to have the corresponding resonance frequency associated with the principal birefringence axes, we make Ω_B to be functions of the polarization principal axis beatings [30], with Ω_{Bxx}, Ω_{Byy}, Ω_{Bxy} and Ω_{Byx} as defined in Chapter 5. Furthermore, the following approximation is used

$$\begin{aligned} \frac{\gamma_e q^2}{\Omega_B^2 - \Omega_1^2 - i\Gamma_B\Omega_1} &= \frac{\gamma_e q^2 / \Omega_1}{\frac{(\Omega_B + \Omega_1)(\Omega_B - \Omega_1)}{\Omega_1} - i\Gamma_B} \approx \frac{\gamma_e q}{2v} \frac{1}{(\Omega_B - \Omega_1) - i\frac{\Gamma_B}{2}} \\ &\cong \frac{\gamma_e \overline{n}\,\overline{\omega}}{cv} \frac{1}{(\Omega_B - \Omega_1) - i\frac{\Gamma_B}{2}} \end{aligned} \tag{A.6}$$

as well as the approximation $q = k_1 + k_2 = \frac{1}{c}(n_1\omega_1 + n_2\omega_2) \cong 2\frac{\overline{n}\,\overline{\omega}}{c}$, where $\overline{n}$ and $\overline{\omega}$ are taken to be the averages of n_1 and n_2, and ω_1 and ω_2 respectively. It is then possible to have the following approximate complex acoustic field amplitudes,

$$
\begin{aligned}
\Delta\rho = {} & \frac{\gamma_e \overline{n}\,\overline{\omega}}{cv} \frac{1}{\left(\Omega_{Bxx} - \Omega_1\right) - i\frac{\Gamma_B}{2}} E_{1x}E_{2x}^{*} \exp\left\{i\left[\left(k_{1x} + k_{2x}\right)z - \left(\omega_1 - \omega_2\right)t\right]\right\} \left\langle \hat{x}_2 \,|\, \hat{x}_1 \right\rangle \\
& + \frac{\gamma_e \overline{n}\,\overline{\omega}}{cv} \frac{1}{\left(\Omega_{Byy} - \Omega_1\right) - i\frac{\Gamma_B}{2}} E_{1y}E_{2y}^{*} \exp\left\{i\left[\left(k_{1y} + k_{2y}\right)z - \left(\omega_1 - \omega_2\right)t\right]\right\} \left\langle \hat{y}_2 \,|\, \hat{y}_1 \right\rangle \\
& + \frac{\gamma_e \overline{n}\,\overline{\omega}}{cv} \frac{1}{\left(\Omega_{Bxy} - \Omega_1\right) - i\frac{\Gamma_B}{2}} E_{1x}E_{2y}^{*} \exp\left\{i\left[\left(k_{1x} + k_{2y}\right)z - \left(\omega_1 - \omega_2\right)t\right]\right\} \left\langle \hat{y}_2 \,|\, \hat{x}_1 \right\rangle \\
& + \frac{\gamma_e \overline{n}\,\overline{\omega}}{cv} \frac{1}{\left(\Omega_{Byx} - \Omega_1\right) - i\frac{\Gamma_B}{2}} E_{1y}E_{2x}^{*} \exp\left\{i\left[\left(k_{1y} + k_{2x}\right)z - \left(\omega_1 - \omega_2\right)t\right]\right\} \left\langle \hat{x}_2 \,|\, \hat{y}_1 \right\rangle
\end{aligned}
\tag{A.7}
$$

Paying attention to the original case without birefringence in equation (A.5), it is possible to generalize our result. Recall that non-birefringent lights were assumed to undergo ideal power transfer between the pump wave and the Stokes wave, as would be the case when both these waves are parallel-polarized (under the slowly varying amplitudes, A_1 and A_2, approximation),

$$
\frac{\partial A_1}{\partial z} + \frac{n}{c}\frac{\partial A_1}{\partial t} + \alpha A_1 = i\frac{\gamma_e \omega_1}{2\rho_0 nc}\Delta\rho A_2
\tag{A.8}
$$

$$
-\frac{\partial A_2}{\partial z} + \frac{n}{c}\frac{\partial A_2}{\partial t} + \alpha A_2 = i\frac{\gamma_e \omega_2}{2\rho_0 nc}\Delta\rho^{*} A_1
\tag{A.9}
$$

In equations (A.8) and (A.9), ρ_0 is the mean density of the fiber. Generalizing the above system of equations (A.8) and (A.9) to the case of birefringence we take the following,

$$
\begin{aligned}
& \frac{\partial E_{1x}}{\partial z} + \frac{n_{1x}}{c}\frac{\partial E_{1x}}{\partial t} + \alpha_{1x}E_{1x} \\
& = i\frac{\gamma_e \omega_1}{2\rho_0 n_{1x} c}\frac{\gamma_e \overline{n}\,\overline{\omega}}{cv} \frac{1}{\left(\Omega_{Bxx} - \Omega_1\right) - i\frac{\Gamma_B}{2}} E_{1x}E_{2x}^{*}E_{2x} \left\langle \hat{x}_2 \,|\, \hat{x}_1 \right\rangle \left\langle \hat{x}_1 \,|\, \hat{x}_2 \right\rangle \\
& + i\frac{\gamma_e \omega_1}{2\rho_0 n_{1x} c}\frac{\gamma_e \overline{n}\,\overline{\omega}}{cv} \frac{1}{\left(\Omega_{Bxy} - \Omega_1\right) - i\frac{\Gamma_B}{2}} E_{1x}E_{2y}^{*}E_{2y} \left\langle \hat{y}_2 \,|\, \hat{x}_1 \right\rangle \left\langle \hat{x}_1 \,|\, \hat{y}_2 \right\rangle
\end{aligned}
\tag{A.10}
$$

$$\begin{aligned}
&\frac{\partial E_{1y}}{\partial z}+\frac{n_{1y}}{c}\frac{\partial E_{1y}}{\partial t}+\alpha_{1y}E_{1y} \\
&= i\,\frac{\gamma_e\omega_1}{2\rho_0 n_{1y}c}\frac{\gamma_e\overline{n}\,\overline{\varpi}}{cv}\frac{1}{\left(\Omega_{Byy}-\Omega_1\right)-i\,\frac{\Gamma_B}{2}}E_{1y}E_{2y}^{*}E_{2y}\langle\hat{y}_2|\hat{y}_1\rangle\langle\hat{y}_1|\hat{y}_2\rangle \\
&+ i\,\frac{\gamma_e\omega_1}{2\rho_0 n_{1y}c}\frac{\gamma_e\overline{n}\,\overline{\varpi}}{cv}\frac{1}{\left(\Omega_{Byx}-\Omega_1\right)-i\,\frac{\Gamma_B}{2}}E_{1y}E_{2x}^{*}E_{2x}\langle\hat{x}_2|\hat{y}_1\rangle\langle\hat{y}_1|\hat{x}_2\rangle
\end{aligned}\tag{A.11}$$

$$\begin{aligned}
&-\frac{\partial E_{2x}}{\partial z}+\frac{n_{2x}}{c}\frac{\partial E_{2x}}{\partial t}+\alpha_{2x}E_{2x} \\
&= i\,\frac{\gamma_e\omega_2}{2\rho_0 n_{2x}c}\frac{\gamma_e\overline{n}\,\overline{\varpi}}{cv}\frac{1}{\left(\Omega_{Bxx}-\Omega_1\right)-i\,\frac{\Gamma_B}{2}}E_{2x}E_{1x}^{*}E_{1x}\langle\hat{x}_1|\hat{x}_2\rangle\langle\hat{x}_2|\hat{x}_1\rangle \\
&+ i\,\frac{\gamma_e\omega_2}{2\rho_0 n_{2x}c}\frac{\gamma_e\overline{n}\,\overline{\varpi}}{cv}\frac{1}{\left(\Omega_{Byx}-\Omega_1\right)-i\,\frac{\Gamma_B}{2}}E_{2x}E_{1y}^{*}E_{1y}\langle\hat{y}_1|\hat{x}_2\rangle\langle\hat{x}_2|\hat{y}_1\rangle
\end{aligned}\tag{A.12}$$

$$\begin{aligned}
&-\frac{\partial E_{2y}}{\partial z}+\frac{n_{2y}}{c}\frac{\partial E_{2y}}{\partial t}+\alpha_{2y}E_{2y} \\
&= i\,\frac{\gamma_e\omega_2}{2\rho_0 n_{2y}c}\frac{\gamma_e\overline{n}\,\overline{\varpi}}{cv}\frac{1}{\left(\Omega_{Byy}-\Omega_1\right)-i\,\frac{\Gamma_B}{2}}E_{2y}E_{1y}^{*}E_{1y}\langle\hat{y}_1|\hat{y}_2\rangle\langle\hat{y}_2|\hat{y}_1\rangle \\
&+ i\,\frac{\gamma_e\omega_2}{2\rho_0 n_{2y}c}\frac{\gamma_e\overline{n}\,\overline{\varpi}}{cv}\frac{1}{\left(\Omega_{Bxy}-\Omega_1\right)-i\,\frac{\Gamma_B}{2}}E_{2y}E_{1x}^{*}E_{1x}\langle\hat{y}_2|\hat{x}_1\rangle\langle\hat{x}_1|\hat{y}_2\rangle
\end{aligned}\tag{A.13}$$

The attenuations α_{1x}, α_{1y}, α_{2x}, and α_{2y} represent the fiber attenuations of the principal axes of polarizations $|\hat{x}_1\rangle$, $|\hat{y}_1\rangle$, $|\hat{x}_2\rangle$ and $|\hat{y}_2\rangle$, respectively. Finally, using the identity $|\hat{x}\rangle\langle\hat{x}|=\frac{1}{2}\left(1+\mathbf{S}_x\cdot\boldsymbol{\sigma}\right)$ which links the Jones matrix unit vector to its Stokes vector $\boldsymbol{S}_x$ on the Poincaré sphere via the Pauli matrix $\boldsymbol{\sigma}$, as well as the simplifications for $\overline{n}_1$, $\Delta\overline{n}_1$, $\overline{n}_2$, $\Delta\overline{n}_2$, $\overline{\alpha}_1$, $\Delta\overline{\alpha}_1$, $\overline{\alpha}_2$, and $\Delta\overline{\alpha}_2$, we arrive at the system of equations (5.1)-(5.4).

B. Fourth Order Runge-Kutta Method of Solution

Using the Fourth Order Runge-Kutta (RK4) numerical method, the solution to the system of equations (5.20)-(5.23) is summarized in equations (B.1)-(B.4), where *n* is the temporal step, and *j* is the spatial step.

$$Y_{1x}(n+1, j+1) = Y_{1x}(n, j) + \frac{K_1 + 2K_2 + 2K_3 + K_4}{6} \tag{B.1}$$

$$Y_{1y}(n+1, j+1) = Y_{1y}(n, j) + \frac{L_1 + 2L_2 + 2L_3 + L_4}{6} \tag{B.2}$$

$$Y_{2x}(n+1, j+1) = Y_{2x}(n, j) + \frac{Q_1 + 2Q_2 + 2Q_3 + Q_4}{6} \tag{B.3}$$

$$Y_{2y}(n+1, j+1) = Y_{2y}(n, j) + \frac{R_1 + 2R_2 + 2R_3 + R_4}{6} \tag{B.4}$$

The coefficients *K_i*, *L_i*, *Q_i*, *R_i*, where *i=1,2,3,4* are defined as:

$$K_1 = -\left\lfloor \beta_{1a} Y_{2x}(n, j) + \beta_{1b} Y_{2y}(n, j) + \varepsilon_{1x} \right\rfloor \cdot Y_{1x}(n, j) \cdot \Delta u \tag{B.5}$$

$$L_1 = -\left\lfloor \beta_{1c} Y_{2y}(n, j) + \beta_{1d} Y_{2x}(n, j) + \varepsilon_{1y} \right\rfloor \cdot Y_{1y}(n, j) \cdot \Delta u \tag{B.6}$$

$$Q_1 = \left\lfloor \beta_{3a} Y_{1x}(n, j) + \beta_{3b} Y_{1y}(n, j) + \varepsilon_{2x} \right\rfloor \cdot Y_{2x}(n, j) \cdot \Delta v \tag{B.7}$$

$$R_1 = \left\lfloor \beta_{3c} Y_{1y}(n, j) + \beta_{3d} Y_{1x}(n, j) + \varepsilon_{2y} \right\rfloor \cdot Y_{2y}(n, j) \cdot \Delta v \tag{B.8}$$

$$K_2 = -\left[\beta_{1a}\left[Y_{2x}(n, j) + \frac{Q_1}{2} \right] + \beta_{1b}\left[Y_{2y}(n, j) + \frac{R_1}{2} \right] + \varepsilon_{1x} \right] \cdot \left[Y_{1x}(n, j) + \frac{K_1}{2} \right] \cdot \Delta u \tag{B.9}$$

$$L_2 = -\left[\beta_{1c}\left[Y_{2y}(n, j) + \frac{R_1}{2} \right] + \beta_{1d}\left[Y_{2x}(n, j) + \frac{Q_1}{2} \right] + \varepsilon_{1y} \right] \cdot \left[Y_{1y}(n, j) + \frac{L_1}{2} \right] \cdot \Delta u \tag{B.10}$$

$$Q_2 = \left[\beta_{3a}\left[Y_{1x}(n, j) + \frac{K_1}{2} \right] + \beta_{3b}\left[Y_{1y}(n, j) + \frac{L_1}{2} \right] + \varepsilon_{2x} \right] \cdot \left[Y_{2x}(n, j) + \frac{Q_1}{2} \right] \cdot \Delta v \tag{B.11}$$

$$R_2 = \left[\beta_{3c}\left[Y_{1y}(n, j) + \frac{L_1}{2} \right] + \beta_{3d}\left[Y_{1x}(n, j) + \frac{K_1}{2} \right] + \varepsilon_{2y} \right] \cdot \left[Y_{2y}(n, j) + \frac{R_1}{2} \right] \cdot \Delta v \tag{B.12}$$

$$K_3 = -\left[\beta_{1a}\left[Y_{2x}(n,j)+\frac{Q_2}{2}\right]+\beta_{1b}\left[Y_{2y}(n,j)+\frac{R_2}{2}\right]+\varepsilon_{1x}\right]\cdot\left[Y_{1x}(n,j)+\frac{K_2}{2}\right]\cdot\Delta u \qquad \text{(B.13)}$$

$$L_3 = -\left[\beta_{1c}\left[Y_{2y}(n,j)+\frac{R_2}{2}\right]+\beta_{1d}\left[Y_{2x}(n,j)+\frac{Q_2}{2}\right]+\varepsilon_{1y}\right]\cdot\left[Y_{1y}(n,j)+\frac{L_2}{2}\right]\cdot\Delta u \qquad \text{(B.14)}$$

$$Q_3 = \left[\beta_{3a}\left[Y_{1x}(n,j)+\frac{K_2}{2}\right]+\beta_{3b}\left[Y_{1y}(n,j)+\frac{L_2}{2}\right]+\varepsilon_{2x}\right]\cdot\left[Y_{2x}(n,j)+\frac{Q_2}{2}\right]\cdot\Delta v \qquad \text{(B.15)}$$

$$R_3 = \left[\beta_{3c}\left[Y_{1y}(n,j)+\frac{L_2}{2}\right]+\beta_{3d}\left[Y_{1x}(n,j)+\frac{K_2}{2}\right]+\varepsilon_{2y}\right]\cdot\left[Y_{2y}(n,j)+\frac{R_2}{2}\right]\cdot\Delta v \qquad \text{(B.16)}$$

$$K_4 = -\lfloor\beta_{1a}[Y_{2x}(n,j)+Q_3]+\beta_{1b}\lfloor Y_{2y}(n,j)+R_3\rfloor+\varepsilon_{1x}\rfloor\cdot[Y_{1x}(n,j)+K_3]\cdot\Delta u \qquad \text{(B.17)}$$

$$L_4 = -\lfloor\beta_{1c}\lfloor Y_{2y}(n,j)+R_3\rfloor+\beta_{1d}[Y_{2x}(n,j)+Q_3]+\varepsilon_{1y}\rfloor\cdot\lfloor Y_{1y}(n,j)+L_3\rfloor\cdot\Delta u \qquad \text{(B.18)}$$

$$Q_4 = \lfloor\beta_{3a}[Y_{1x}(n,j)+K_3]+\beta_{3b}\lfloor Y_{1y}(n,j)+L_3\rfloor+\varepsilon_{2x}\rfloor\cdot[Y_{2x}(n,j)+Q_3]\cdot\Delta v \qquad \text{(B.19)}$$

$$R_4 = \lfloor\beta_{3c}\lfloor Y_{1y}(n,j)+L_3\rfloor+\beta_{3d}[Y_{1x}(n,j)+K_3]+\varepsilon_{2y}\rfloor\cdot\lfloor Y_{2y}(n,j)+R_3\rfloor\cdot\Delta v \qquad \text{(B.20)}$$

Curriculum Vitae

DAISY WILLIAMS

EDUCATION

2010-2014	**Ph.D. in Physics (Photonics)** Thesis defense on September 3, 2014. University of Ottawa (Dean’s List) Recipient of CREATE Grant Recipient of Admission Scholarship at the University of Ottawa
2006-2010	**B.Sc. Honours Physics-Mathematics** University of Ottawa (Dean's List) Recipient of Prestige Scholarship at the University of Ottawa, for academic achievement and excellence in sports.

LIST OF PUBLICATIONS

Journal Papers

1. Journal publication in *Applied Optics Journal*

D. Williams, X. Bao, L. Chen, "All-optical NAND/NOT/AND/OR logic gates based on combined Brillouin gain and loss in an optical fiber," Applied Optics **52**, 3404-3411 (2013).

2. Journal publications in *Photonics Research Journal*

D. Williams, X. Bao, L. Chen, "Characterization of high nonlinearity in Brillouin amplification in optical fibers with applications in fiber sensing and photonic logic," Photonics Research **2**, 1-9 (2014).

3. Journal publication in *Chinese Optics Letters*

D. Williams, X. Bao, L. Chen, "Improved all-optical OR logic gate based on combined

Brillouin gain and loss in an optical fiber," Chinese Optics Letters **12**, 1-4 (2014).

4. Journal publication in *Photonics Research Journal*

D. Williams, X. Bao, L. Chen, "Effects of Polarization on stimulated Brillouin Scattering in a birefringent optical fiber," Photonics Research **2**, 126-137 (2014).

5. Journal accepted for publication in *Chinese Optics Letters*

D. Williams, X. Bao, L. Chen, "Investigation of combined Brillouin gain and loss in a birefringent fiber with applications in sensing," Chinese Optics Letters **12**, (2014).

Patents

1. Regular Patent Application filed in the USPTO

D. Williams, X. Bao, L. Chen, "All-optical NAND/NOT/AND/OR logic gates based on the combined Brillouin gain and loss in an optical fiber" US 14/048,004, Filed: Oct. 7, 2013, Published: Apr. 10, 2014.

2. Regular Patent Application filed in the CIPO

D. Williams, X. Bao, L. Chen, "All-optical NAND/NOT/AND/OR logic gates based on the combined Brillouin gain and loss in an optical fiber," CA 2829175, Filed: Oct. 7, 2013, Published: Apr. 5, 2014.

3. Regular Patent Application filed in the USPTO

Daisy Williams, Xiaoyi Bao, Liang Chen, "Method for Optical Phase Modulation, Optical Phase Modulator and optical network employing the same," US 13/633,749, Filed: Oct 2, 2012, Published: Apr. 4, 2013.